Tarduno, J.A., Duncan, R.A., Scholl, D.W., et al., 2002
Proceedings of the Ocean Drilling Program, Initial Reports Volume 197

5. Site 1205[1]

Shipboard Scientific Party[2]

BACKGROUND AND SCIENTIFIC OBJECTIVES

Nintoku Seamount occupies a central position in the Emperor Seamount chain of volcanoes and an important point in the paleolatitude history of the Hawaiian hotspot (see the **"Leg 197 Summary"** chapter). The structure of the seamount is that of an elongate volcanic edifice, aligned north-northwest along the Emperor trend, with two prominent ridges trending southwest and south-southwest as far as 100 km from the main center (Fig. **F1**). Undoubtedly, Nintoku Seamount is a plexus of coalesced volcanoes (Greene et al., 1980), much like many of the larger seamounts in this chain, whose positions are controlled to some degree by the fabric of the underlying ocean lithosphere. The Nintoku system is, however, clearly isolated from Yomei Seamount, ~100 km to the north, and Jingu Seamount, ~200 km to south, by abyssal depths.

In seismic reflection profile, the main edifice of Nintoku Seamount rises steeply from >5000 m as predominantly unsedimented volcanic slopes to a thinly sedimented (10–200 m thick), gently domed summit region between ~1400 and 1200 m that covers ~3400 km² (Greene et al., 1980). From analysis of seismic reflection survey data (Dalrymple et al., 1980a) and core material recovered by drilling at Site 432 (Jackson, Koizumi, et al., 1980), the shipboard party of Deep Sea Drilling Project (DSDP) Leg 55 proposed that Nintoku Seamount was in an intermediate atoll stage (no lagoon but fringing reefs and banks and extensive carbonate bank interiors) before subsidence removed the island below the wave base. It is further speculated that a few small remnant volcanic peaks pierce the shallow-water bank interior deposits.

Nintoku Seamount apparently remained at or above sea level long enough to be almost completely flattened by subaerial erosion and wave action. Reefs were not identified in seismic profiles, but fragmental material of the bryozoan-algal facies was recovered, documenting shallow-water sedimentary conditions (McKenzie et al., 1980). Impor-

F1. Nintoku Seamount region bathymetry, p. 33.

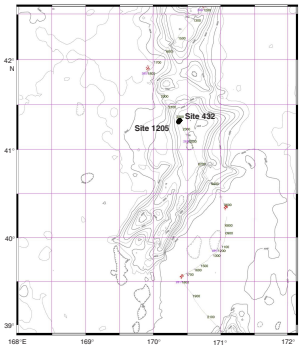

[1] Examples of how to reference the whole or part of this volume.
[2] Shipboard Scientific Party addresses.

Ms 197IR-105

tantly, the sedimentary record suggests deposition in waters cooler than the present tropical reef belt (±20° latitude). Shallow-water carbonate sedimentation ceased in Paleogene time (Jackson, Koizumi, et al., 1980).

Site 432 was located on the northwestern edge of the summit region of Nintoku Seamount in a gently sloping area mapped as terrace deposits. Although the sediment thickness was predicted to be 80 m from the site surveys, drilling intersected basement at only 42 meters below seafloor (mbsf). Poorly recovered sedimentary deposits are shallow-water biogenic carbonate beds typical of proximal depositional terraces flanking reefs and banks and fossiliferous volcanic sand (Jackson, Koizumi, et al., 1980). Drilling at Site 432 penetrated 32 m of volcanic basement (74 mbsf total) before terminating because of hole caving and damage to the bottom-hole assembly (BHA).

Site 1205 (41°20.00′N, 170°22.70′E) was located 100 m southwest of DSDP Site 432, in 1310 m water depth, where previous drilling had reached basement beneath Paleocene lagoonal deposits. We elected to return to Site 432 for a number of reasons. First, previous drilling at Site 432 had intersected reasonably unaltered basalt with good remanent magnetic properties (Kono, 1980), but insufficient lava flows were sampled to adequately determine paleolatitude. Hence, deeper drilling promised to achieve this goal, potentially providing a time-averaged paleolatitude for the Leg 197 hotspot motion test. Second, a short presite survey around Site 432 (see **"Underway Geophysics,"** p. 28) revealed a simple basement structure suitable for deeper drilling; nearby sites were found to have thinner apparent sediment cover. Third, the composition of previously recovered lava flows (alkali basalt to hawaiite) is most consistent with eruption during a postshield phase of volcano construction. Our petrochemical objectives are best met by recovery of tholeiitic lavas, which we hoped lay beneath the known section.

Another aspect of Nintoku Seamount's character deserves attention: the age of the sampled volcanic rocks in the overall age progression along the Emperor Seamounts volcanic lineament. With reference to Figure **F1,** p. 26, in the "Leg 197 Summary" chapter, it is apparent that the reported radiometric age for alkali basalt flows from Site 432 (55–56 Ma) (Dalrymple et al., 1980b) is younger than expected if the Emperor Seamounts form a linear age progression (Clague and Dalrymple, 1989). This is consistent with the postshield classification of Nintoku Seamount capping lavas. Deeper drilling, we predicted, would penetrate erosional surfaces and sample the older, main sequence of shield-building lava flows.

OPERATIONS

Transit to Proposed Site HE-4A (DSDP Site 432) and Underway Survey over Nintoku Seamount

The position of Site 1205, at the northwestern corner of the summit platform of Nintoku Seamount, was located nearly 600 nmi south-southeast of Site 1204. The area of Site 1205 was last visited during DSDP Leg 55 (Site 432) in early August 1977. Nintoku Seamount, one of the nine seamounts of the Emperor chain named by Robert Dietz in 1954, was named for the 16th emperor of Japan.

The 596-nmi transit to the first survey waypoint was accomplished at an average speed of 11.6 kt. During the 52-hr voyage, the skies were overcast, with occasional showers and fog hampering visibility. The sea and swell did not exceed 7 ft. The air temperature increased from 10° to 17°C as the vessel entered the Kuroshiro Current during the early evening of 7 August 2001.

Prior to spudding Hole 1205A, a geophysical survey was conducted to acoustically image the stratigraphic and structural setting of the site. Crossing high-resolution seismic reflection profiles were obtained using a single 80-in^3 water gun firing every 6 s. At 0030 hr on 4 August the vessel slowed to 6 kt to deploy the seismic equipment, and by 0600 hr the survey was completed. The 29.5-nmi survey was conducted at an average speed of 5.6 kt. To provide adequate sediment thickness to ensure lateral stability of the BHA while spudding, Site 1205 was positioned where the sedimentary blanket was estimated to be at least 60 m thick.

The thrusters were lowered as the vessel established location using the Global Positioning System (GPS) coordinates selected from the site survey, ~100 m southwest of proposed Site HE-4A (DSDP Site 432) in the Leg 197 Scientific Prospectus. After the vessel was on station at 0632 hr, the hydrophones were lowered, concurrent with the making up of a new BHA. A beacon was deployed at 0735 hr.

Hole 1205A

The corrected precision depth recorder (PDR) depth referenced to the dual elevator stool was obtained and indicated 1319.4 m. The BHA was made up of a 9.875-in rotary core barrel (RCB) hard formation C-7 bit, a mechanical bit release, a modified head sub, an outer core barrel, a modified top sub, a modified head sub, seven 8.25-in drill collars, a tapered drill collar, six 5.5-in drill pipe sections, and one crossover sub.

Hole 1205A was spudded with the RCB at 1230 hr on 4 August and tagged the depth of the seafloor at 1321.0 m. Coring advanced slowly through 42.7 m of sandstone and breccia rich in basalt fragments at an average rate of penetration (ROP) of 12.5 m/hr (recovery = 9.1%). Basement coring began with Core 197-1205A-6R (42.7–52.2 mbsf) and proceeded to a depth of 132.9 mbsf, when operations were suspended to change the bit, which had accumulated 52.1 hr of rotation.

Progress in the mostly fresh, fine-crystalline basaltic basement was the slowest thus far in the leg and was only uncommonly interrupted by sudden spurts of rapid penetration through thin soil horizons between lava flows. Until a depth of 59 mbsf was attained, slow penetration rate in basement was also attributed to the BHA not being sufficiently buried to allow the driller to apply more than 15,000 lb of weight on bit.

A total of 90.2 m of basaltic basement was cored (average recovery = 61.3%). The cored sedimentary section was 42.7 m (recovery = 9.1%). The ROP in basement varied from 4.8 m/hr (Core 197-1205A-6R [42.7–52.2 mbsf]) to 0.5 m/hr (56.9–58.9 mbsf). The average ROP in basement was 1.9 m/hr. The average total recovery for the 132.9 m of cored sedimentary and basement sequences was 49.0%.

Reentry

The bit cleared the free-fall funnel (FFF) at 1330 hr on 7 August and was captured by the vibration-isolated subsea television camera. The bit

cleared the rotary table at 1630 hr and was quickly removed and replaced with another new C-7 hard formation rotary bit. The used bit was inspected and found to be in excellent condition with only 0.0625 in loss of outside gage. The cones were intact with no chipped or missing teeth. All nozzles were clear. Because of the excessive hours of rotation, most of which were accumulated in basement, the bit was retired from service in spite of the outward excellent appearance.

The used mechanical bit release was also replaced with a fresh unit. After spacing out the new assembly, the drill string was deployed and positioned over the FFF by 2115 hr. As the driller was making a near-perfect reentry, the bit lightly tapped the throat of the cone, which immediately toppled over on its side, rendering it useless for reentry purposes. Apparently, the sandy surface formation was too firm to allow the 2.5-m length of 13.375-in casing to sufficiently penetrate the hard seafloor during deployment. The FFF was perched on, rather than nestled in, the hard sandy bottom of the summit platform of the Nintoku Guyot. The bit tapping the FFF was enough to upset the unstable installation.

Considerable bottom mud was stirred up as a result of the FFF tipping over, which obscured the now-unadorned Hole 1205A. However, the driller and dynamic positioning personnel persevered, and the reentry of the open hole was achieved by 2209 hr.

Coring resumed in Hole 1205A and advanced to 215.8 mbsf, when flow-back at the drill floor connection indicated that the float valve was jammed open. It required seven runs with the depluggers and core barrel to clear the obstruction. This effort consumed 5 hr and involved two runs with the long deplugger, two runs with fresh core barrels, another run with the long deplugger, and two runs with the chisel deplugger.

Basement coring again resumed and penetrated to 274.6 mbsf, when once again flow-back at the rig floor required one run with the deplugger and one run with a fresh core barrel to clear the obstruction from the float valve. Time-scheduled coring in Hole 1205A was terminated at a final depth of 326.0 mbsf. The cored interval was 326.0 m with a recovery of 165.6 m of sediment and basalt (recovery = 50.8%) (Table T1). The total basement penetration was 283.3 m with 161.8 m recovered (recovery = 57.1%). The coring effort required two bits with a total rotating time of 110.8 hr. The average ROP in basement was 2.6 m/hr. The cored sediment was 42.7 m with 3.87 m recovered (recovery = 9.1%). At this juncture during Leg 197, 935.2 m of basement had been cored with 487.9 m recovered (recovery = 52.2%).

T1. Coring summary, Site 1205, p. 92.

Logging Attempt

Following the retrieval of the last core, the hole was conditioned with a wiper trip up to 69 mbsf and down to 279 mbsf. The hole was washed and reamed from 279 to 326 mbsf with no apparent fill detected at the bottom. Following the displacement of the hole with 100 bbl of sepiolite mud, the bit was placed at the logging depth of 90 mbsf. The first planned logging run was with the triple combination tool string. Unfortunately, it was not possible for the loggers to deploy the tool deeper than 136 mbsf because the hole was blocked by a bridge and swelling formation. The logging effort was aborted, and the drilling equipment was retrieved.

The drilling equipment was secured, and the BHA was dismantled in preparation for the 400-nmi journey to proposed Site HE-6A, Koko Seamount. The beacon was recovered, and the thrusters and hydrophones

were retracted. The moonpool was secured for the transit, as the vessel got under way at 0600 hr on 12 August to the last site of Leg 197.

LITHOSTRATIGRAPHY

At Site 1205 one hole was RCB drilled, penetrating sediment before reaching basement at 42.7 mbsf. Five sediment cores with very low recovery (2%–16%) were obtained. The character of the sediment changes considerably between cores, and we identified five sedimentary units (I–V) in the sequence, which are described below (Fig. F2). Chemical analyses show a rapid downhole decrease in carbonate (C and $CaCO_3$) abundance (Fig. F3; Table T2). Several types of calcite-cemented silty sandstone were recovered, containing well-rounded to subrounded basalt clasts, bioclasts, and glassy ash fragments, as well as minor clay (Fig. F4A; also see "Site 1205 Smear Slides," p. 173). A notable component of the recovered sediment is silt-sized grains of hematite and other Fe oxides (Fig. F4B; see also "Site 1205 Smear Slides," p. 173).

Bioclasts include several recognizable fossil species, indicating varying but relatively shallow-water depths for the depositional environment, as documented by previous results of DSDP Leg 55, which penetrated the same sedimentary section at DSDP Site 432 (Jackson, Koizumi, et al., 1980).

Description of Lithologic Units

Unit I

Interval: 197-1205A-1R-1, 0 cm, to 1R-1, 9 cm
Depth: 0.00–0.09 mbsf
Age: early Eocene (Eocene/Paleocene boundary)

This interval consists of olive to dark gray silty sandstone cemented by calcite and containing well-rounded to subrounded basalt fragments, bioclasts, volcanic glass fragments, and minor clay. The bioclasts are benthic foraminifers, bryozoan fragments, and coralline red algae (Fig. F5). The inferred bryozoan fragments and the rounded pebbles of basalt and basaltic minerals (olivine, clinopyroxene, and plagioclase) are abundant.

Unit II

Interval: 197-1205A-1R-1, 9 cm, to 2R-1, 22 cm
Depth: 0.09–4.82 mbsf
Age: early Eocene (Eocene/Paleocene boundary)

Dark yellowish brown (10YR 4/4) fine-grained vitric sandstone contains palagonitic volcanic glass and hematite in a calcite cement. Bioclasts are benthic foraminifers, bryozoan fragments, and coralline red algae. Volcanic glass fragments in different stages of palagonitization dominate. Opaque grains of hematite are common. Bryozoan "worm fragments" increase downhole, giving the sediment a whitish yellow-brown appearance.

F2. Sedimentary units in Hole 1205A, p. 34.

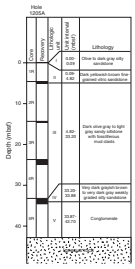

F3. Chemical analyses of carbonate, p. 35.

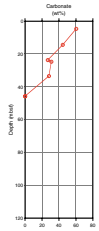

T2. Carbonate data, Hole 1205A, p. 93.

F4. Sedimentary components from smear slides, p. 36.

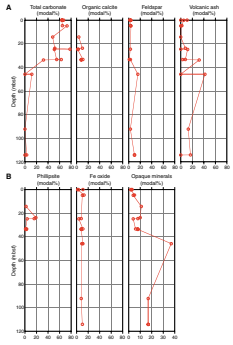

F5. Features from Hole 1205A, p. 37.

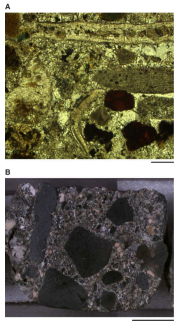

Unit III

Interval: 197-1205A-2R-1, 22 cm, to 4R-CC, 12 cm
Depth: 4.82–24.94 mbsf
Age: Eocene

Unit III is a dark olive-gray (5Y 3/2) to light gray sandy siltstone with prominent "wriggling" wisps of white bryozoans. Another distinguishing feature is indistinct "mud clasts," which are mainly present in interval 197-1205A-2R-1, 22–60 cm, and are composed of opaque minerals (15%), brown clay (60%), and calcite (25%). Rounded rock fragments (basalt and tuff) are present together with bioclasts (benthic foraminifers, red algae, and bryozoans).

Although separated from Section 197-1205A-3R-1 by a nonrecovered interval as thick as 17 m, we infer that Unit III continues through Core 197-1205A-4R, where it is a dark grayish brown (10YR 4/1) sandy siltstone with prominent white bryozoans throughout. In this lower part, the core is highly fractured by drilling. Carbonate debris of bryozoans and foraminifers is present with volcanic clasts and opaque minerals cemented by calcite. In interval 197-1205A-4R-1, 0–112 cm (23.7–24.82 mbsf), the sediment is a dark olive-gray (5Y 3/2) calcareous siltstone with abundant secondary phillipsite and opaque minerals (probably hematite). Bryozoans stand out clearly from the dark silty background.

Unit III has a fragile porous appearance in Sections 197-1205A-2R-1 and 3R-1. Farther downcore it contains a more loosely packed siltstone disturbed by drilling. At 24.3 mbsf the recovered sediment has been completely disturbed and reworked into a drilling slurry. The core catcher contains a 3-cm-long calcite-filled vug and shell fragments, which are indicative of a nearshore depositional environment.

Unit IV

Interval: 197-1205A-5R-1, 0–67 cm
Depth: 24.94–33.87 mbsf
Age: early Eocene (Eocene/Paleocene boundary)

Unit IV contains a very dark grayish brown (2.5Y 3/2) to very dark gray (5Y 3/1) weakly graded silty sandstone. Beds of brownish yellow (10YR 6/8) shell fragments are present in intervals 197-1205A-5R-1, 9–12 cm, 39–42 cm, and 59–61 cm. The bioclastic fragments have a size of ~5 mm. Charcoal and wood fragments are present in Section 197-1205A-5R-1 at 26 and 41 cm.

Unit V

Interval: 197-1205A-5R-2, 0–127 cm
Depth: 33.87–35.15 mbsf
Age: early Eocene (Eocene/Paleocene boundary)

This unit is a calcareous conglomerate (Fig. **F5B**) with 5- to 90-mm rounded to subrounded clasts of fine-grained to aphanitic dark green basalt as well as secondary hematite fragments. The matrix is calcite cement with bioclastic and volcaniclastic components ranging in size from 2 to 12 mm. In thin section the matrix displays a plethora of bioclastic forms. The observed species are bivalves (pelecypods [45%]), red algae

(40%), foraminifers (5%), algal borings (8%), and micrite envelopes (2%).

The color varies in shades of red, green, yellow, and gray, depending on the proximity of particular clasts. The volcanic components are highly altered, and it is difficult to recognize the protolith.

Depositional Environment

The sandstone consists primarily of resedimented volcanic material, where the chief constituent is slightly rounded altered glass fragments, indicating minimal abrasion during transport. Bryozoans and red algae live in water depths of 20–30 m or less. The basaltic clasts are well rounded, suggesting transport and deposition in a relatively high-energy erosional environment. These varying indicators all suggest deposition in a beach or near-beach environment.

Farther downhole, horizons of red soil indicate subaerial weathering between lava flows (see **"Physical Volcanology and Igneous Petrology,"** p. 8). The geologic history revealed at Site 1205 documents a subsiding volcanic island, resulting in subaerial units becoming capped by marine sediment deposited in a shallow-water, high-energy environment (see also Jackson, Koizumi, et al., 1980). The siltstone interval 197-1205A-4R-1, 0–112 cm, contains secondary phillipsite, indicating substantial burial of the sequence, which is typical of subsiding volcanic islands.

BIOSTRATIGRAPHY

Calcareous Nannofossils

Hole 1205A was drilled in a water depth of 1309 m using a rotary core bit. Five sediment cores were recovered above basalt, which was encountered in Section 197-1205A-5R-2. Core 197-1205A-1R was barren of nannofossils. Samples from Cores 197-1205A-2R to 5R contain nannofossils ranging from scarce to high in abundance. Nannofossil preservation is poor to moderate in samples from Cores 197-1205A-2R to 3R and poor to good (mostly moderate) in samples from Cores 197-1205A-4R to 5R.

We made biostratigraphic assignments to core catcher and other selected samples using calcareous nannofossils. Figure **F6** shows the biozonal assignment. Abundance and distribution of nannofossils in each sample studied were recorded in the paleontology (PAL) database and are shown in Table **T3.**

Zonation

We assign Samples 197-1205A-2R-1, 10–11 cm, to 5R-1, 32–33 cm, to nannofossil Zone NP10. The nannofossil assemblage is dominated by species typical of this zone (e.g., *Campylosphaera dela, Chiasmolithus bidens, Neochiastozygus chiastus, Neococcolithes protenus, Rhabdosphaera pinguis, Toweius eminens, Toweius gammation,* and *Toweius pertusus*). Rare specimens of *Discoaster binodosus, Discoaster multiradiatus, Zygodiscus adamas/bramlettei,* and *Tribrachiatus contortus* are also present. Zone NP10 straddles the upper Paleocene/lower Eocene boundary. However, the evolutionary first appearance of *T. contortus* occurs just above the lower NP10 zonal boundary. The first appearance datum of *T. contortus*

F6. Calcareous nannofossil zonation in Hole 1205A, p. 38.

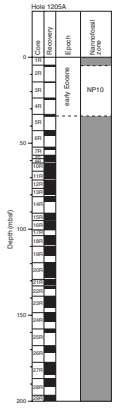

T3. Nannofossil abundance, distribution, and biozonal assignments, p. 94.

and the Paleocene/Eocene boundary are both estimated to be at 54.7 Ma (see "Biostratigraphy," p. 9, in the "Explanatory Notes" chapter). The presence of *T. contortus* therefore indicates these samples are in the lower Eocene part of Zone NP10 (estimated age range of 53.6–54.7 Ma).

All samples examined below Sample 197-1205A-5R-1, 32–33 cm, were barren.

Environment

Significant numbers of specimens belonging to the Family Braarudosphaeracea (viz., *Braarudosphaera bigelowii, Braarudosphaera discula, Micrantholithus* cf. *Microantholithus entaster,* and *Micrantholithus* spp.) are present in the samples. Members of this family are normally very rare in open-ocean sediments and suggest nearshore conditions at this site during Zone NP10 (see Siesser et al., 1992, for a review of the environmental preferences of the Braarudosphaeracea).

Discussion

During DSDP Leg 55, Holes 432 and 432A were drilled very close to Hole 1205A (Hole 432A is <100 m from Hole 1205A). A thin sedimentary section consisting of 5.5 m of Quaternary foraminiferal ooze overlying Paleogene volcanic sand was recovered from Hole 432. In Hole 432A, the upper 36 m of sediments was washed, after which ~3.5 m of volcanic sandstone, calcareous conglomerate, basalt, and red lateritic clay were recovered in Core 1 and Core 2. Basalt flows were reached in Core 3 (Shipboard Scientific Party, 1980).

In Hole 432, only Quaternary nannofossils were found; no nannofossils were found in Hole 432A. Planktonic foraminifers were found, however, in Holes 432 and 432A and suggested an age range of late Paleocene to early Eocene for the Paleogene sediments overlying basalt in both holes (Shipboard Scientific Party, 1980). As described earlier, nannofossils found in Hole 1205A show the sedimentary sequence here can be restricted to early Eocene.

Benthic foraminifers, ostracodes, and benthic macrofossils indicated a shallow-water reef environment for the Paleogene sediments in Holes 432 and 432A. However, the Leg 55 Shipboard Scientific Party (1980) believed the fossils had probably been reworked from a nearby reef complex and redeposited on the flanks of the seamount, rather than representing an in situ shallow-water reef environment at the drill site. The Braarudosphaeracea we found in Hole 1205A suggest simply "nearshore" conditions.

PHYSICAL VOLCANOLOGY AND IGNEOUS PETROLOGY

We encountered basement at 42.7 mbsf in Hole 1205A and penetrated 283.2 m into a sequence of subaerially erupted lava flows and interbedded sediment and soil horizons, of which 160.0 m was recovered (recovery = 56.5%). The minimum age of the basement in Hole 1205A is constrained to late Paleocene–early Eocene (nannofossil Zone NP10 [~53.6–55.0 Ma]) on the basis of three nannofossil assemblages recovered in Core 197-1205A-5R immediately above basement (see "Biostratigraphy," p. 7).

Basement in Hole 1205A was divided into 30 lithologic units, of which 25 are lava flows and 5 are composed of soil or sandstone (Table T4; Fig. F7). The lava flow units include a'a and pahoehoe, as well as transitional flow types. They range from aphyric to highly plagioclase- and olivine-phyric basalt and are variably affected by posteruption alteration. Shipboard geochemical analysis showed that two of the lava flow units recovered (Subunits 18b and 19b [230–250 mbsf]) consist of tholeiitic basalt, whereas the other units are all composed of alkalic basalt. Clasts of hawaiite were recovered from a conglomerate immediately overlying basement in Section 197-1205A-5R-2; this rock type was not found deeper in the basement section. The lithology and major element composition of the lavas from Nintoku Seamount are similar to those of lavas erupted during the postshield stage of young Hawaiian volcanoes, such as Mauna Kea Volcano. In detail, there are differences in the trace element compositions of lavas from Nintoku Seamount and volcanoes from the Hawaiian Islands, which may result either from differences in source composition or from variations in the degree of mantle melting.

Hole 1205A is located ~100 m southwest of Hole 432A (Fig. F1), which was drilled 31.9 m into basement during DSDP Leg 55 (Jackson, Koizumi, et al., 1980). Parts of three lava flow units were identified in the basement section in Hole 432A. The two upper flows are composed of feldspar-phyric alkali basalt with a combined thickness of 2.6 m, separated from underlying sparsely olivine-plagioclase-phyric alkali basalt by a 10-cm-thick layer of red clay soil. Dalrymple et al. (1980b) obtained an ^{40}Ar-^{39}Ar age of 56.2 ± 0.6 Ma for one sample of alkali basalt from the lowermost flow unit. The basement units from Hole 432A are very similar in lithology and chemistry to the youngest basement rocks recovered from Hole 1205A (see "Geochemistry," p. 16).

Macroscopic Description

In this section, we describe the different lithologies of the basement sequence in Hole 1205A. Detailed descriptions of each core section can be found in the "Site 1205 Core Descriptions," p. 1.

The Hole 1205A basement was divided into 30 lithologic units (Table T4; Fig. F7), composed of lava flows capped by red soil or deeply weathered flow tops, and one sandstone unit (Unit 4). We used several criteria for determining flow unit boundaries: major changes in lithology; the occurrence of weathered flow tops, soil horizons, or sedimentary interbeds; and the presence of basal flow breccia, glass-rich zones, or abrupt changes in vesicularity. We considered soil horizons (11 were recovered) to be subunits of the underlying flow, except in the few examples where the soil overlay relatively unaltered lava and no fragments of the underlying flow could be found in the soil (Fig. F8). In these examples, the soil was given a separate unit number (Units 2, 7, 23, and 25). Of the volcanic units, Units 9 and 10 and Subunits 12b, 15b, and 18b were composed of two or more lobes. These were identified by the presence of vesicular, glassy lobe boundaries (see "Physical Volcanology," p. 11); however, because the mineralogy and lithology of the different lobes were in all cases very similar, they were not divided into separate subunits.

T4. Distribution, thickness, and lithology of basement units, Hole 1205A, p. 95.

F7. Recovery, thickness, composition, and lithology of basement units, p. 39.

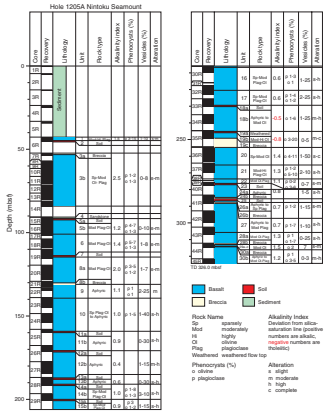

F8. Red clay soil and unweathered basalt units, p. 40.

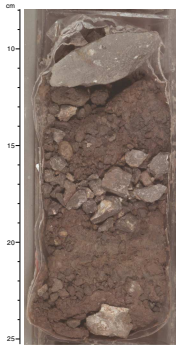

Lava Flow Units

The major lithologic features of each of the volcanic units in Hole 1205A are summarized in Figure F7. The thickness and vesicularity of the flows and the presence of oxidized flow tops and soil horizons indicate that the flows were erupted subaerially (see also Fig. F56, p. 83, in the "Leg 197 Summary" chapter).

Lava flow units above 230 mbsf are all composed of alkali basalt and are aphyric (Unit 9 and Subunits 11b, 12b, and 13b), plagioclase-phyric (Unit 10), or olivine- and plagioclase-phyric (Units 6, 16, and 17 and Subunits 3b, 5b, 8a, 14b, and 15b). Phenocrysts generally make up <7 modal% of the rock, although plagioclase phenocrysts comprise up to 15 modal% of the rock in Unit 1 (Fig. F9). In several Units (e.g., Units 9 and 27), plagioclase and olivine crystals up to 1 cm in diameter are present as xenocrysts and are intergrown in a cumulate texture. These crystals often have rounded and embayed outlines. Olivine phenocrysts are partially to completely altered to Fe oxyhydroxide, carbonate, and clay, and plagioclase is partially altered to sericite along cracks in the crystal structure (see "Alteration and Weathering," p. 18). The groundmass of the alkali basalt lava is composed of plagioclase, olivine, clinopyroxene, titanomagnetite, and glass. The glass is generally completely replaced by secondary minerals. Many of the flows are highly vesicular (up to 50%), with 1- to 10-mm-diameter vesicles, especially close to unit boundaries. Pipe vesicles are present close to flow bases. Vesicles are generally filled with secondary minerals, including carbonate, clay, and zeolite (see "Alteration and Weathering," p. 18).

Subunits 18b and 19b are composed of sparsely to highly olivine-phyric tholeiitic basalt. Olivine is present both as microphenocrysts and as larger phenocrysts up to 4 mm in diameter, which are partially to completely replaced by secondary minerals. The interior portion of Subunit 19b contains an olivine-enriched layer, consisting of up to 20 modal% altered olivine crystals. The groundmass of the tholeiitic units is composed of plagioclase, clinopyroxene, titanomagnetite, and minor glass; olivine is absent as a groundmass phase. Subunit 19b is underlain by a relatively thick breccia and soil horizon (Subunit 19c; 74 cm recovered).

Several units contain auto-breccia horizons, which were formed during emplacement of the flow and which may occur either at the base of the unit (e.g., Units 8, 19, 24, 26, and 28), at the top of the unit (Units 3 and 30), or both (Unit 29). Breccias are generally poorly sorted, clast supported, and composed of angular clasts of the associated lava unit cemented by carbonate, clay, zeolite, and Fe oxyhydroxide (Fig. F10).

The conglomerate immediately overlying basement in Section 197-1205A-5R-2 contains rounded clasts, up to 8 cm in diameter, of fine-grained aphyric lava with trachytic texture (Fig. F11). Shipboard inductively coupled plasma–atomic emmission spectroscopy [ICP-AES] analysis of two of these clasts showed them to be composed of hawaiite, a relatively evolved rock type that was not found deeper in the basement section.

Soils

The uppermost parts of lava flows range from slightly weathered (slight discoloration of the flow top) to deeply weathered (highly altered upper part of the flow), with an overlying red soil (Fig. F12). Soils are up to 30 cm thick (although recovery of these poorly consolidated

F9. Highly plagioclase-phyric alkali basalt, p. 41.

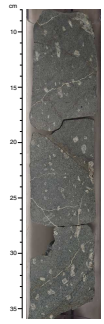

F10. Plagioclase-olivine-phyric basalt overlying aphyric basalt, p. 42.

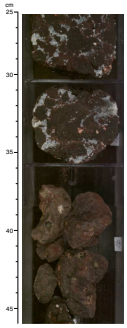

F11. Hawaiite clasts embedded in fossiliferous sand, p. 43.

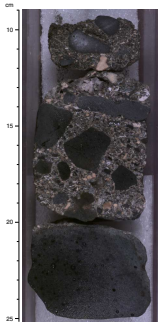

F12. Red clay soil overlying weathered aphyric basalt, p. 44.

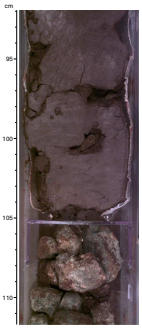

deposits is likely to be much lower than for the volcanic rocks), and they may represent substantial time intervals. Soils are present throughout the basement sequence; however, they tend to be more common in the upper 250 m of the basement (Fig. F7). The soils are red brown, generally structureless or poorly bedded, and usually contain round, highly altered clastlike domains composed of the underlying lava unit in a clay- to silt-sized matrix. Microscopic examination reveals that the matrix is composed of opaque minerals, rare unidentified organic material, amorphous iron oxide/oxyhydroxide, feldspar, and palagonite and smectite after volcanic glass, together with basaltic lava fragments in various stages of alteration. Most soil samples listed on Table T5 have total organic carbon contents close to the analytical detection limits (0.01 wt%) for shore-based analyses. The highest values were found in Unit 10 (0.12 wt%), Unit 20 (0.08–0.10 wt%), and Unit 23 (0.08–0.11 wt%). Organic carbon reported on Table T5 was determined by the difference between the total carbon and carbonate carbon. The analytical procedures involved are described in Shipboard Scientific Party (1998). The basal breccia of Subunit 19c also contains a significant amount of organic carbon (up to 0.10 wt%).

T5. Organic carbon contents of soils, p. 97.

Unit 4 is a 12-cm-thick laminated vitric sandstone composed of fragments of vesicular lava and tephra fragments (the latter almost completely replaced by smectite and palagonite), plagioclase, iron oxide, and opaque minerals.

Physical Volcanology

In this section we describe the internal architecture and key flow structures of the Site 1205 lavas and briefly discuss their volcanological implications. The terminology used in this section to describe the lavas is outlined in **"Physical Volcanology and Igneous Petrology,"** p. 10, in the "Explanatory Notes" chapter.

The volcanic basement at Site 1205 consists of at least 25 eruptive units, which range in thickness from 0.6 to ~31.5 m. The division into eruptive units is based principally on the presence of soils and deeply weathered lava tops, indicating that there was a significant time break between the emplacement of each subaerial lava flow unit (Table T4; Fig. F7). The greater abundance and thickness of the soils toward the top of the succession may indicate a longer time between emplacement of successive lava flows in that part of the section.

Because of good recovery of the lava units (average = ~70%; range = 33%–100%), we obtained sufficient information about the internal architecture of individual lava units to classify them according to flow type. Using the type of flow or lobe contacts, along with the arrangement of internal flow structures, we identified four flow types in the Site 1205 succession (see also **"Physical Volcanology and Igneous Petrology,"** p. 10, in the "Explanatory Notes" chapter). The Site 1205 lavas are categorized as compound pahoehoe (five units), simple pahoehoe (five units), or a'a (five units). A further 10 units were classified as transitional because the flows exhibit characteristics of both pahoehoe and a'a flows. The key features of the lava flow units are listed in Table T6, and the main characteristics of each lava type are summarized below.

T6. Structure and morphology of lava units, p. 98.

Compound Pahoehoe (Units 9, 10, 12, 15b, and 18b)

At Site 1205, the compound pahoehoe lava flow units range in thickness from 4 to 25 m (average = 13 m) (see Table T6) and account for

24.5% of the total cored thickness of flows in the succession. Each unit consists of 2 to >10 vertically stacked lobes, which range from 0.4 to 7 m in thickness.

The pahoehoe lobes generally have smooth glassy lobe margins grading sharply to aphanitic (hypohyaline to hypocystalline) groundmass with intersertal texture, whereas the lobe interiors are typically fine grained and are characterized by an intergranular texture. Most commonly, the lobes have highly vesicular upper and lower crusts and sparsely vesicular or nonvesicular lobe interiors. Some of the smaller lobes are vesicular throughout. Viscous flow fabric is not present in these lavas, and the vesicle fabric is isotropic, which is consistent with laminar flow of low viscosity lava beneath a stationary insulating crust. These lobes also commonly feature segregation structures, such as small pipe vesicles, vesicle cylinders, and megavesicles, which are indicative of lava flow inflation during emplacement (Fig. F13A).

F13. Architecture of pahoehoe lava, p. 45.

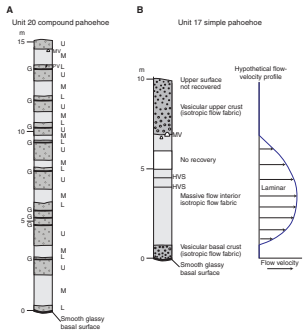

Simple Pahoehoe (Sheet Lobes; Units 13b, 16, 17, 20, and 21)

Five of the lava flow units at Site 1205 are categorized as "simple" pahoehoe because in addition to their characteristic pahoehoe morphology they consist of only one lobe. Simple pahoehoe accounts for ~18% of the total thickness of flows in the succession, and lobe thicknesses range from ~4 to 14 m (average = ~9.5 m). The morphology and internal structures of these flows are identical to those of the lobes in the compound pahoehoe flows (Fig. F13), the most significant differences being greater lobe thickness and the presence of a single lobe in the sampled section.

A'a (Units 8, 19b, 19c, 24, 29, and 30)

Five lava flow units in the Site 1205 basement succession were tentatively identified as a'a flows, and these account for ~17% of the total flow thickness (Table T6). The a'a lava flow units range in thickness from 0.5 to 17 m (average = 8.4 m) and are most common in the lower part of the succession (below 275 mbsf). At Site 1205 these units consist of a single lobe and have massive interiors that rest on and are capped by a thin breccia (5 to 95 cm recovered thickness) consisting of spinose and clinkerlike lapilli-sized basalt clasts (Fig. F14). The flow-top breccia of Subunit 14b and Unit 24 was not recovered (Table T6). Internally, these lavas are characterized by a central region with isotropic flow fabric that is flanked by zones showing distinct viscous flow fabric (Fig. F14). This fabric is expressed by subparallel arrangement of flow bands (present as 1- to 2-mm-thick dark gray and subhorizontal wispy bands), by alignment of tabular plagioclase phenocrysts, and by elongate vesicles drawn out in response to viscous flow at high strain rates. The observed flow fabric is best explained by sheared laminar flow around a flow center that was transported within a viscous flow as a plug.

F14. Architecture and flow velocity of a'a lava, p. 46.

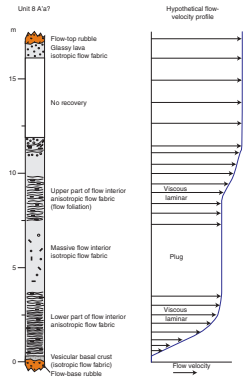

Transitional (Units 1, 3, 5b, 6, 11b, 14b, 22, 26a, 27, and 28)

Ten lava flow units are classified as transitional flow types. Consequently, they are the most common flow type at Site 1205, comprising ~40% of the total lava flow thickness in the succession (Table T6).

Cored thicknesses of the transitional flows range from ~3 to 32 m (average = 11 m), and all units consist of a single lobe in the cored section.

The morphology and structure of these lava units are highly variable, but all exhibit characteristics that are transitional between pahoehoe and a'a flows (Fig. F15). For example, Unit 3 has a pahoehoe flow base but is capped by breccia. Subunit 5b is capped by a smooth pahoehoe surface, but the internal flow fabric is similar to that of a'a flows. Subunit 11b is capped and floored by flow breccia and thus exhibits a surface morphology typical of an a'a flow; however, its internal flow architecture is more like that of a simple pahoehoe flow (Fig. F15).

F15. Architecture and flow velocity of transitional lava, p. 47.

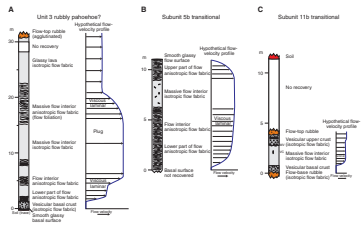

Remarks

The pahoehoe flows make up ~40% of the lava flow succession at Site 1205 and represent the low-viscosity end-member of the lava flow types. All of the pahoehoe flows exhibit an internal flow architecture identical to that found in modern pahoehoe flow fields in Hawaii and elsewhere (Hon et al., 1994; Self et al., 1998; Thordarson and Self, 1998). Consequently, an endogenous mode of emplacement (transport of lava beneath an insulating crust and growth by lava flow inflation) was an important mechanism for dispersing lava from source vents during the postshield stage at Nintoku Seamount. This mode of emplacement would have facilitated transport of lava in preferred pathways (e.g., lava tubes) over long distances without much cooling, which may account for the large thicknesses of the compound pahoehoe flows at Site 1205.

The a'a lavas represent flows that had the highest bulk viscosity at the time of emplacement. However, this should not be taken as an indication of higher initial melt viscosities, especially since the composition of the a'a lavas is identical to that of the pahoehoe lavas (see "Geochemistry," p. 16). The transition from pahoehoe to a'a is a common occurrence in modern basaltic lavas and, in principle, is controlled by two factors: viscosity and strain rate. These in turn are controlled by a range of parameters such as eruption or flow rates, slope, cooling rates, dissolved gas, and bubble content (e.g., Peterson and Tilling, 1980). Active pahoehoe flows have a plastic fluid surface that is stretched like rubber as the lobe advances, ensuring transport beneath a stationary and insulating crust. However, such ductile behavior breaks down if, for example, the lava is subjected to sufficiently high strain rates (e.g., by flowing over steeper terrain) that cause the hot plastic lava to be ripped apart, exposing the incandescent flow interiors. This process forms the spinose clinkerlike chunks that accumulate to form a flow-top breccia. This breccia rides on top of the flow and is dumped at the flow front, where it is later buried beneath the advancing lava.

Given the hybrid nature of the transitional lavas at Site 1205, it is possible that they are flows that solidified during different stages of the pahoehoe-to-a'a transition. However, some (e.g., Unit 3) exhibit flow structures (pahoehoe base and breccia top) similar to those found in rubbly pahoehoe flows. This implies a fundamentally different mode of emplacement, where the coherent crust on an inflating pahoehoe flow is disrupted by surges of lava through the molten flow interior and consequently causes large changes in the lava heat budget and rheology (Keszthelyi et al., 2000; Keszthelyi and Thordarson, 2000).

Petrography

Silicate Mineralogy

All the lavas from Site 1205 are aphyric to plagioclase- and/or olivine-phyric basalt. Plagioclase is typically the most abundant phenocryst phase (up to 15 modal% of the rock) and occurs as phenocrysts up to several centimeters in size (Fig. F16A). Olivine phenocrysts form up to 20 modal% of the rock and are generally smaller (up to 8 mm in size). In most cases, phenocrysts show evidence of being out of equilibrium with the groundmass. Plagioclase phenocrysts frequently display rounded edges (Fig. F16B), optical zonation (Fig. F16C), straining (Fig. F16D), fractures (Fig. F16E), resorption rims, and embayments (Fig. F16F). Olivine crystals occur in glomerocrysts with plagioclase (Fig. F16G), and olivine phenocrysts are also often embayed (Fig. F16H), rounded, or have hollow centers. Olivine phenocrysts in Subunits 18b and 19b contain inclusions of Cr spinel. Subunit 19b and Unit 20 appear to contain two generations of olivine phenocrysts: larger phenocrysts that are typically 1 mm in diameter and microphenocrysts that are of a similar size to the groundmass. Consequently, it is difficult to distinguish phenocrystic olivine from groundmass olivine in these rocks. In general, olivine microphenocrysts are recognized by their euhedral shape.

Olivine phenocrysts are partly to completely altered (see also "Alteration and Weathering," p. 18). In some cases, an unaltered relict remains, but fractures and crystal margins are altered to iddingsite, Fe oxyhydroxide, or green-brown clay (Fig. F16I). Completely altered crystals are replaced by Fe oxyhydroxide, iddingsite, or, rarely, calcite. In Unit 27, olivine phenocrysts are partially deuterically altered to biotite or phlogopite along crystal margins and fractures (Fig. F16J).

Gabbroic xenoliths are present in Subunit 5b and consist of 2- to 15-mm-sized glomerocrysts of plagioclase, olivine, and interstitial ophitic clinopyroxene (Fig. F16K). The similarity in mineralogy of these xenoliths to the host rock suggests that they may be cognate in origin. Plagioclase crystals in these xenoliths are rounded and show compositional zoning and are similar in appearance to those found as phenocrysts in the basalt, possibly indicating a common origin for both.

The groundmass typically contains plagioclase, clinopyroxene, devitrified glass, titanomagnetite, and olivine. Most rocks display a subophitic texture, with large (up to 4 mm) elongate clinopyroxene crystals enclosing smaller plagioclase laths and, more rarely, olivine (Fig. F16L). Clinopyroxene is typically pink in plane-polarized light and displays moderate pleochroism, reflecting a relatively high titanium content. Olivine and clay (replacing glass) tend to occur in patches around the ophitic clinopyroxene. Groundmass olivine was not always identified in thin section. In some units, olivine is probably not a groundmass phase (e.g., Subunits 18b and 19b), and in others, the degree of alteration renders recognition difficult. In addition, microphenocrystic olivine may be difficult to distinguish from groundmass olivine. The absence of groundmass olivine in Subunits 18b and 19b indicates that petrographically these units are composed of tholeiitic basalt, in contrast to the alkalic basalt that makes up the rest of the sequence. Groundmass olivine is occasionally unaltered but is typically replaced by Fe oxyhydroxide, iddingsite (e.g., Fig. F16M), or brown clay. In Unit 27 and Subunit 30b, groundmass olivine has been altered to strongly

F16. Plagioclase phenocryst features, p. 48.

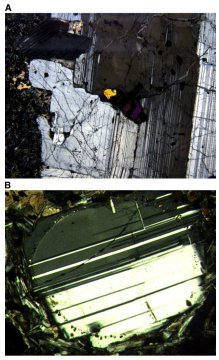

pleochroic biotite or phlogopite, although the Cr spinel inclusions remain.

Glass is usually completely altered to green and brown clay, Fe oxyhydroxide, zeolite, or chlorite. In Sample 197-1205A-35R-4, 77–79 cm (Subunit 19b), interstitial glass is replaced by a bright green and completely isotropic mineral, which may be palagonite.

Many basalts display a poorly to well-developed trachytic texture in which plagioclase crystals are aligned parallel to one another and frequently wrap around phenocrysts, indicating the flow direction. In Sample 197-1205A-10R-2, 73–75 cm (Fig. F16N), the foliation undulates on a millimeter scale. In the macroscopically flow-banded units (Units 28 and 29), this trachytic texture is particularly well developed and even the phenocrysts are aligned with their long axes parallel to the local flow direction. Some olivine phenocrysts (altered to clay) appear to have been sheared and deformed by the process (Fig. F16O).

Basalt from Site 1205 differs from that from Site 1203 (Detroit Seamount) in that phenocrysts are not generally glomerocrystic and also that they tend to be out of equilibrium with the surrounding groundmass. These disequilibrium features (resorbed margins, zoning, etc.) also characterize many of the phenocrysts in basalt from Holes 1204A and 1204B.

Opaque Mineralogy

The opaque mineralogy of the Site 1205 basement lavas is summarized in Table T7. The sequence is dominated by titanomagnetite. Exceptions are extensive development of maghemite in oxidized flow tops (e.g., Sample 197-1205A-24R-2 [Piece 9, 124–130 cm]) (Fig. F17A), basal flow breccias, and in the tholeiitic basalt that comprises Subunit 19b (Fig. F17B, F17C). Note that here, as in other Leg 197 site reports, we do not distinguish between maghemite and titanomaghemite (or Ti-bearing maghemite), as they are indistinguishable using reflected-light microscopy. We use the term Fe oxyhydroxide to include a number of Fe-rich secondary minerals that have poor crystal form, including amorphous goethite (α-FeOOH), akaganeite (ß-FeOOH), lepidocrocite (γ-FeOOH), ferroxyhyte (δ-FeOOH), and ferrihydrite ($5Fe_2O_3 \cdot 9H_2O$) (see Waychunas, 1991).

The morphology of the titanomagnetite crystals differs between the alkalic and tholeiitic basalt units recovered at Site 1205. The alkalic basalt contains almost exclusively equant, subhedral, skeletal octahedra (Fig. F17D, F17E), whereas the tholeiitic basalt contains dendritic morphologies, suggestive of high cooling rates, in addition to the equant octahedra (Fig. F17F, F17G). The hawaiite clasts from the conglomerate immediately overlying volcanic basement (Unit V) (see "Lithostratigraphy," p. 5) contain goethite and Fe oxyhydroxide and unaltered titanomagnetite (Fig. F17H). A dendritic form of titanomagnetite is also present and occurs in discrete layers that may be parallel or transverse to the plagioclase laths that define the trachytic texture. These dendritic forms distinguish the opaque mineralogy of these hawaiite cobbles from the basalt flows below (Fig. F17I). Titanomagnetite in other units and away from oxidized flow tops and basal breccias is generally unaltered, although ilmenite oxidation features (Buddington and Lindsley, 1964; Haggerty, 1991) are more extensive toward the bottom of the basement section. For example, in Subunit 3b ilmenite oxidation lamellae are present (Fig. F17J, F17K). In Unit 27 the titanomagnetite appears "twinned" because of ilmenite oxidation (Fig. F17L), but this feature

T7. Opaque mineralogy of basement rocks, p. 99.

F17. Titanomagnetite morphologies, p. 56.

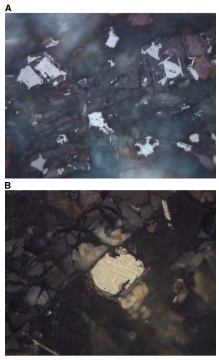

disappears when the microscope stage is rotated (Fig. F17M), consistent with the bireflectant nature of ilmenite. Rarely, maghemite is developed along cleavage planes and around crystal rims in those crystals of titanomagnetite that have been partially altered to ilmenite (Fig. F17N, F17O, F17P, F17Q).

Olivine is a ubiquitous silicate phase throughout the Site 1205 basement lava units and often contains inclusions of opaque minerals. The compositions of these inclusions are different in tholeiitic and alkalic basalt lava types. In alkali basalt, opaque mineral inclusions in the groundmass and phenocryst olivine are of titanomagnetite (Fig. F17R, F17S). However, in the tholeiitic Subunit 18b, such inclusions are of Cr spinel and are unaltered, although the host olivine crystals have been entirely replaced by clay and, occasionally, Fe oxyhydroxide (Fig. F17T). In Sample 197-1205A-35R-1 (Piece 1A, 32–34 cm), inclusions of Cr spinel have reacted with the melt to form rims of titanomagnetite (Fig. F17U, F17V).

Primary sulfide is rare in the basement lavas (Table T7). It occurs as <0.01-mm inclusions in silicate and oxide minerals in Subunits 3b (Sample 197-1205A-8R-1, 59–61 cm), 5b (Sample 197-1205A-15R-3, 37–39 cm), 8a (Sample 197-1205A-20R-5, 67–68 cm), and 13b (Sample 197-1205A-28R-3, 4–6 cm). These bleblike inclusions are probably composed of pentlandite. The presence of pentlandite indicates that subsolidus reequilibration has occurred (Augustithis, 1979).

Geochemistry

Major and trace element abundances were determined by ICP-AES (see "Physical Volcanology and Igneous Petrology," p. 10, in the "Explanatory Notes" chapter) for 27 samples of lava flows from the basement at Site 1205 and 2 lava clasts from the conglomerate overlying basement in Section 197-1205A-5R-2 (Table T8).

In the total alkali vs. silica diagram (Fig. F18), only two of the lava flows classify as tholeiitic basalt (Subunits 18b and 19b). The other flow units sampled are all composed of alkalic basalt. Compared to the other samples, the two lava clasts from the conglomerate have the highest total alkali contents (Fig. F18), the lowest MgO contents (1.6 and 3.2 wt%), relatively high Al_2O_3 and low CaO (Fig. F19), and are composed of hawaiite (West et al., 1988). The sequence of intercalated alkalic and tholeiitic basalt overlain by evolved alkalic lavas, such as hawaiites, found at Site 1205 is typical of the postshield stage of Hawaiian volcanism. For example, a similar sequence of subaerially erupted lava flows is exposed on the northeast flank of Mauna Kea Volcano (West et al., 1988; Frey et al., 1990, 1991).

The 32 m of alkalic basalt recovered from Nintoku Seamount at Site 432 during DSDP Leg 55 is very similar in composition to the volcanic rocks in the upper 184 m of the igneous basement at Site 1205 (Figs. F18, F19). Conglomerate containing clasts of hawaiite is present immediately above the volcanic basement at both Sites 1205 and 432. However, tholeiitic basalt was not recovered at Site 432.

In MgO variation plots (Fig. F19), lavas from Nintoku Seamount define trends that overlap with those defined by basalt from Site 433 Suiko Seamount (Kirkpatrick et al., 1980; M. Regelous et al., unpubl. data); such trends are typical of Hawaiian lava flows. The lowest abundances of Al_2O_3, Na_2O, K_2O, TiO_2, and Zr are in the two samples of tholeiitic basalt (Subunits 18b and 19b). Abundances of these oxides

T8. Major and trace elements, p. 101.

F18. Total alkali vs. SiO_2 plot, p. 67.

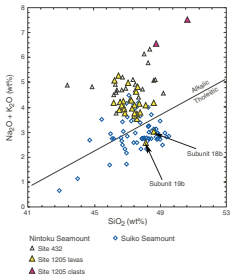

F19. Na_2O, K_2O, TiO_2, CaO, Al_2O_3, and Zr vs. MgO, p. 68.

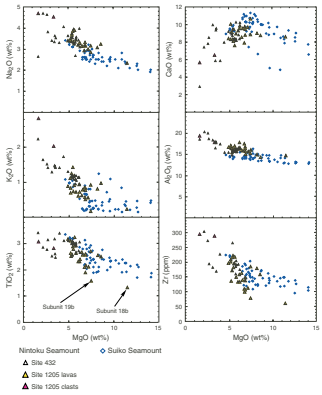

and Zr are inversely correlated with MgO and, except for TiO_2, they reach a maximum in lavas with the lowest MgO content (the hawaiite that occurs as clasts in the conglomerate overlying the basement lava flows). In contrast, the hawaiite lava has relatively low CaO content (Fig. **F19**). A notable contrast to data from Detroit Seamount (see **"Physical Volcanology and Igneous Petrology,"** p. 11, in the "Site 1203" chapter) is that the variation in K_2O content reflects magmatic rather than postmagmatic processes (see **"Alteration and Weathering,"** p. 18).

In the uppermost 184 m of the basaltic sequence (Units 1 through 17), MgO abundances vary only from 5.03 to 6.98 wt% (Table **T8**). These alkali basalt units, together with the underlying tholeiitic basalt of Subunits 18b and 19b, show systematic compositional variations with depth. For example, with increasing depth, the abundance of Zr, Ba, and alkalinity (a measure of the deviation of the sample from the tholeiitic-alkalic boundary line in Fig. **F18**) systematically decrease (Fig. **F19**). The systematic geochemical variations with depth do not extend below Subunit 19b; Units 20–30 are composed of alkali basalt with relatively high Zr and Ba contents (Fig. **F20**).

With increasing depth from Unit 1 to Subunit 19b, the Ti/Zr ratio systematically increases from ~80 to 130 but then decreases to ~85–106 in Units 20–30 (Fig. **F20**). Samples with the lowest Ti/Zr (from Unit 1 and Subunit 3b) also have relatively low Sc content (Fig. **F21**). The two hawaiite clasts also have a low Ti/Zr (~60) and low Sc, coupled with relatively low MgO and CaO content (Figs. **F19, F21;** Table **T8**). These geochemical characteristics are similar to those of postshield hawaiites from Mauna Kea Volcano (Frey et al., 1990) and indicate that clinopyroxene fractionation was an important process as the eruption rate decreased at Nintoku Seamount.

Although the geochemical characteristics of lavas from Nintoku and Suiko Seamounts and their variation with eruption age are broadly similar to Hawaiian lavas, there are important geochemical differences between lavas from these volcanoes. Such differences are not unexpected because even active Hawaiian volcanoes that are located close together, such as Kilauea and Mauna Loa Volcanoes, erupt geochemically distinct lavas (e.g., Frey and Rhodes, 1993). Lavas from Nintoku and Suiko Seamounts and Mauna Kea Volcano have significantly different Zr/Ba, Zr/Sr, Ti/Ba, and Ti/Sr ratios; in each case these ratios increase in the order Nintoku Seamount < Mauna Kea Volcano < Suiko Seamount (Fig. **F22**). These differences may be the result of systematic differences in the extent of mantle melting or differences in source composition. Resolving the effects of these processes will be a goal of shore-based research.

A plot of Y vs. Zr abundances clearly illustrates an important geochemical difference between East Pacific Rise mid-ocean-ridge basalt (MORB) and Hawaiian basalt; at a given Zr content the MORB has a higher Y content than Hawaiian lavas (Fig. **F23**). Since Y is a compatible element in garnet, the abundance of Y in a magma is controlled by the proportion of residual garnet present at the time of melt segregation, assuming similar source compositions. Therefore, garnet is a more important residual phase for Hawaiian basalt than for MORB. There are, however, differences between Hawaiian volcanoes. At a given Zr content, Y abundances increase in the order Mauna Kea Volcano = Koolau Volcano < Mauna Loa Volcano < Suiko Seamount. The trends for these Hawaiian volcanoes and for MORB define a fan-shaped array of lines. Surprisingly, the Nintoku Seamount trend clearly crosscuts the Suiko trend. Thus, the Zr/Y ratio is more variable (factor of 2.5) in lavas from Nin-

F20. Alkalinity, Ti/Zr, Zr, and Ba, p. 69.

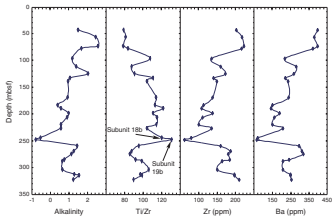

F21. Sc vs. MgO for Sites 1205 and 432, p. 70.

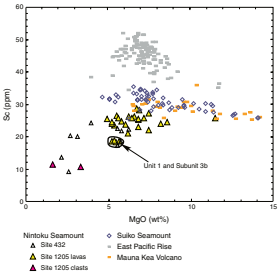

F22. Zr/Ba, Zr/Sr, Ti/Ba, and Ti/Sr vs. MgO, p. 71.

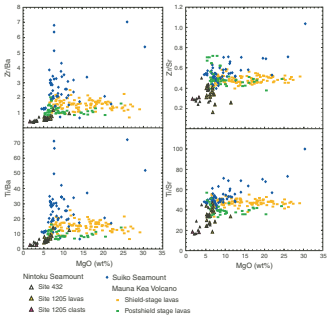

F23. Y and Zr/Y vs. Zr, p. 72.

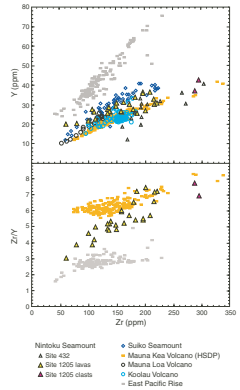

toku Seamount than in lavas from the Mauna Kea shield and from the East Pacific Rise (Fig. F23). The larger range for Nintoku Seamount lavas may result in part from variable extents of melting and proportions of residual garnet during the postshield stage of Nintoku Seamount and in part from the clinopyroxene-dominated fractionation that was important in creating the most evolved lavas with >200 ppm Zr (the hawaiite clasts and alkali basalt from Unit 1 and Subunit 3b).

ALTERATION AND WEATHERING

Thirty basement units were identified in Hole 1205A. In this hole, the sequence includes 25 units or subunits of basaltic composition, 7 volcaniclastic breccia units or subunits, and 12 soil horizons, defined as units or subunits. Unit 4 is a sandstone (see "Physical Volcanology and Igneous Petrology," p. 8).

All lava flows and volcaniclastic sediment have undergone secondary alteration. Alteration mineralogy and vesicle and vein fillings were defined in rocks from Site 1205 by color, habit, and hardness in hand specimen, by optical properties in thin section, and by analogy with well-studied minerals identified during previous legs. Some X-ray diffraction (XRD) analyses were conducted to confirm identification of secondary minerals. However, instrumental problems were encountered during the cruise and the XRD data should be used only as a general guide for mineral recognition.

The effects of alteration in rocks from Site 1205 are identified in the lava flow units in terms of (1) alteration assemblages and vein and vesicle filling and (2) alteration chemistry.

Alteration Assemblages and Vein and Vesicle Fillings

All lava flows recovered are slightly to highly altered basalt (Fig. F24). Overall, the degree of alteration is slight in the Hole 1205A basement sequence. However, several thin weathered flow tops were identified and present higher degrees of alteration (see "Physical Volcanology and Igneous Petrology," p. 8). The alteration degree increases slightly downhole toward flows of tholeiitic composition (see "Physical Volcanology and Igneous Petrology," p. 8), although the degree of alteration remains low.

The sample color is the first indication of the alteration conditions. Cores fall mainly in the range dark gray (N3) to medium-light gray (N6), which are characteristic of unaltered basalt. In more altered intervals, colors are variable between light brown (5YR 5/6), moderate yellowish brown (10YR 5/4), dark yellowish orange (10YR 6/6), grayish orange (10YR 7/4), or greenish gray (5G 6/1). No clear zonation was observed in the cores of Hole 1205A that could be related to different redox conditions in the sequence.

In the following sections, the alteration assemblages and vesicle and vein fillings are described. For a summary of downhole alteration assemblages and vesicle and vein fillings, see Figure F24. All vein information was also recorded in the alteration and vein logs (see "Site 1205 Alteration Logs," p. 220, and "Site 1205 Vein Logs," p. 223). The alteration assemblages and vein and vesicle fillings are generally homogeneous downhole.

The alteration assemblages are dominated by Fe oxyhydroxide, clay, and zeolite. Green clay such as smectite (saponite and nontronite) and

F24. Alteration, minerals, vesicles, and vesicle and vein fillings, p. 73.

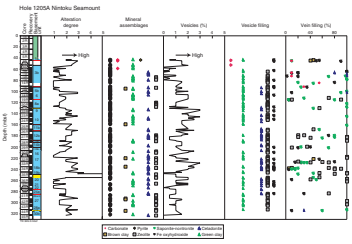

blue-green clay such as celadonite are the main phases. Some brown clay is also present. Zeolite minerals are present in almost all of the sequence. The main zeolite mineral was identified by XRD as phillipsite. A small amount of carbonate was identified in the uppermost units (Subunits 1a and 3b) as well as some secondary pyrite in Subunit 1a. In the most altered intervals, Fe oxyhydroxide dominates and is sometimes well crystallized as goethite. From examination of thin sections (see **"Site 1205 Thin Sections,"** p. 174), we identified small amounts of micas next to the bottom of Hole 1205A (Subunits 28a, 29b, and 30b). These minerals partly replace olivine (as phlogopite-biotite) or are incipient in the groundmass (as chlorite and stilpnomelane?).

Vesicularity is high in some intervals of the Hole 1205A sequence (see also **"Physical Volcanology and Igneous Petrology,"** p. 8). Vesicles are variably unfilled, lined, or filled by secondary minerals. Figure **F25** shows an example of vesicles filled and/or lined with celadonite. As for alteration assemblages, the dominant minerals are clay (saponite/nontronite and celadonite), Fe oxyhydroxide (sometimes as goethite), and zeolite. Zeolite is often present as well-shaped crystals. In the uppermost units of the Hole 1205A sequence, vesicles are also filled with carbonate.

The basement sequence in Hole 1205A is very sparsely veined. Veins are usually very thin (~0.5 mm wide) and do not present a preferred orientation. Veins are filled with variable proportions of green clay (saponite/nontronite), blue-green clay (celadonite), Fe oxyhydroxide, and zeolite minerals (Fig. **F24**). Overall, zeolites are the dominant alteration minerals.

F25. Vesicle with celadonite and saponite, p. 74.

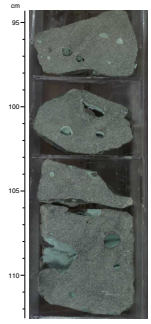

Alteration Chemistry

ICP-AES analyses of major and trace element contents were conducted on board and are used in this section to evaluate the effects of alteration on the whole-rock chemistry. It should be noted, however, that mainly the freshest samples were analyzed and these data might not be representative of the overall effect of alteration processes. Variations in the abundances and ratios of some chemical elements (K_2O and Cu/Zr, Co/Zr, and Zn/Zr ratios) and loss on ignition (LOI) vs. depth are reported in Figure **F26.** LOI is low in the whole sequence, varying from ~1 to 3 wt%. LOI in one sample from volcaniclastic Subunit 19b (Sample 197-1205-35R-4, 77–79 cm) is higher (5.52 wt%). LOI increases slightly downhole toward the tholeiitic basalt units, which confirms the hand-specimen observations and the visual estimations of the degree of alteration (Fig. **F24**).

F26. LOI, K_2O, Cu/Zr, Co/Zr, and Zn/Zr with depth, p. 75.

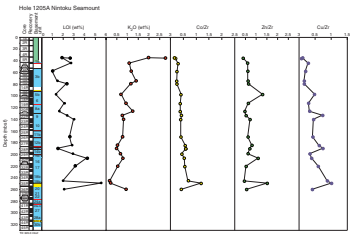

K_2O abundance is low in the Hole 1205A sequence except for the two first samples (e.g., Samples 197-1205A-5R-2, 31–33 cm, and 5R-2, 101–103 cm), which are clasts within a conglomerate. K_2O abundance decreases slightly downhole from ~1.5 to 0.5–1 wt%. This feature is more likely related to a change in the parental composition of the magma than a change of the alteration conditions, as the uppermost units are alkali basalt and several of lowermost units are tholeiitic basalt (see **"Physical Volcanology and Igneous Petrology,"** p. 8). The sample from Subunit 19b, which has high LOI, does not have a high K_2O abundance, indicating that K_2O might not be highly mobilized during alteration of the Hole 1205A sequence.

Co/Zr ratios are constant downhole, with values of ~0.5. The only exception is the sample from Subunit 19b, which displays a higher ratio

(~1.2). Zn/Zr ratios are also fairly constant downhole, with values of ~0.5. Three samples have higher ratios at ~1: Subunit 5b (e.g., Sample 197-1205A-16R-2, 84–86 cm), Unit 16 (e.g., Sample 197-1205A-32R-2, 114–116 cm), and Subunit 19b (e.g., Sample 197-1205A-35R-4, 77–79 cm). Cu/Zr ratios are also fairly constant downhole, with values of ~0.5. Cu/Zr ratios slightly increase downhole toward tholeiitic units. The constant Cu/Zr, Co/Zr, and Zn/Zr ratios of the Hole 1205A sequence indicate that these trace metals were not likely mobilized during alteration processes.

Volcaniclastic Units

Subunits 3a, 8b, 19c, 24b, 26b, 28b, and 30a are described as volcaniclastic basaltic breccia (see **"Physical Volcanology and Igneous Petrology,"** p. 8). Subunits 3a, 8b, and 30a are olivine-plagioclase-phyric basalt breccia, Subunit 19c is composed of olivine-phyric basalt breccia, and Subunits 24b and 26b are aphyric basalt breccia. Alteration features associated with these breccia are similar to those described for basaltic lava flow units. Cement is composed of carbonate in Subunit 3a and variable proportions of Fe oxyhydroxide and zeolite in the other units.

Summary

All igneous rocks recovered at Site 1205 (Hole 1205A) have undergone low-temperature alteration. Alteration features are defined in the basaltic units in terms of secondary mineral assemblage, apparent as vesicle filling, vein filling, and replacement of groundmass and primary minerals. Overall, the lava flows are slightly altered with a small increase downhole toward the units of tholeiitic basalt composition. Weathered flow tops were recognized where the degree of alteration is higher (see also **"Physical Volcanology and Igneous Petrology,"** p. 8). The alteration assemblage is homogeneous downhole and is composed of Fe oxyhydroxide, saponite and/or nontronite, celadonite, and zeolite. Vesicle and vein fillings present the same assemblages. Veining is very sparse in the entire Hole 1205A sequence, indicating small focused fluid circulation. Most of the secondary alteration probably developed in diffuse fluid circulation systems.

All these minerals are characteristic of very low temperature conditions. The estimated temperatures for the formation of celadonite and nontronite are within the range 30°–60°C (Alt, 1995), and saponite can form at slightly higher temperature (from 15° to 170°C) (Alt, 1995). The presence of micas replacing olivine (phlogopite-biotite?) is interpreted as high-temperature deuteric alteration during the last stages of magma cooling. The presence of incipient micas in the groundmass is more difficult to interpret because there is no evidence for high-temperature hydrothermal fluid circulation in the basement sequence of Hole 1205A, and further shore-based studies are needed to resolve their origin.

In contrast to the first two sites of Leg 197 (Sites 1203 and 1204) K_2O was not greatly mobilized during alteration event(s) at Site 1205. Other trace elements (e.g., Cu, Zr, and Zn) do not show evidence for mobilization, as expected for low-temperature alteration events.

PALEOMAGNETISM AND ROCK MAGNETISM

Paleomagnetic and rock magnetic measurements at Site 1205 on Nintoku Seamount focused on assessing the nature of the natural remanent magnetization (NRM) of basement rock and obtaining a preliminary estimate of the paleolatitude of the site during basement formation (a minimum of 55 Ma, as estimated by nannofossil biostratigraphy) (see "Biostratigraphy," p. 7). The basement section at Site 1205 is dominated by basaltic lava flows with some units separated by soil horizons or weathered flow tops (see "Physical Volcanology and Igneous Petrology," p. 8). Fossiliferous sandstone was recovered in Cores 197-1205A-1R through 4R. The sandstone/basalt contact is represented by a basalt cobble conglomerate. Because of limited recovery, paleomagnetic analysis of the sandstone and conglomerate units was reserved for shore-based study. All shipboard samples for paleomagnetic investigations were collected as drilled minicores.

Rock Magnetism

Magnetic Susceptibility, Koenigsberger Ratio, and Median Destructive Field

Low-field volume-normalized magnetic susceptibility was measured on all oriented samples after alternating-field (AF) demagnetization with the Kappabridge KLY-2 magnetic susceptibility meter. In addition to oriented samples, 24 unoriented core chips (~1–5 g/cm^3 in size) were measured. Three measurements were taken for each sample and then averaged. Measurements were repeatable to within 1% of the average value. The range of magnetic susceptibilities is 0.6×10^{-3} to 84.4×10^{-3} SI, with an arithmetic mean of 27.5×10^{-3} SI.

The Koenigsberger ratio (Q) was calculated for each sample using a present geomagnetic field intensity of 34.2 A/m (International Geomagnetic Reference Field; Barton et al., 1995). Koenigsberger ratios range from 0.7 to 80.0 (mean = 8.8). Median destructive field (MDF), calculated based on detailed stepwise AF demagnetization data used for constraining characteristic remanent directions (see below), range from 3.1 to 63.3 mT (mean = 21.6 mT).

Figure F27 shows a plot of volume magnetic susceptibility (K), the Koenigsberger ratio (Q), and MDF vs. depth. A peak in Q-ratio values corresponds to basement Unit 10, a sparsely plagioclase-olivine phyric to aphyric basalt lava flow with little alteration. A peak in MDF values corresponds to a number of unoriented oxidized pebbles from Unit 9 that were not used for paleomagnetic studies (see below). These samples also have a relatively low Q-ratio and magnetic susceptibility, possibly corresponding to slight maghemitization of iron oxides in this unit (see "Physical Volcanology and Igneous Petrology," p. 8).

F27. Magnetic susceptibility, Koenigsberger ratio, and MDF, p. 76.

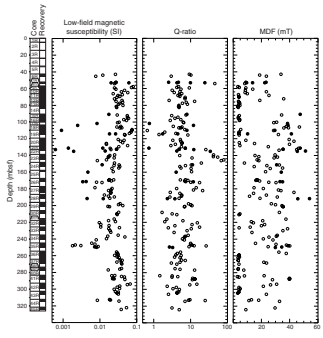

Lowrie-Fuller Tests and Coercivity of Remanence Measurements

An estimation of magnetic domain state can be made using the Lowrie-Fuller test (Lowrie and Fuller, 1971). Generally, multidomain grains require larger destructive fields to remove strong-field thermoremanent magnetization (TRM) than a weak-field TRM. The strong-field TRM is approximated with a saturation isothermal remanent magnetization

(SIRM); the weak field is approximated with an anhysteretic remanent magnetization (ARM). A caveat for use of this test, however, is that the magnetic mineralogy is uniform. Changes in magnetic coercivity related to different magnetic minerals can mimic changes in magnetic domain size. Isothermal remanent magnetization (IRM) acquisition and backfield IRM acquisition were also measured to estimate the coercivity of remanence of the samples (Table T9).

Samples displaying single-domain (SD) magnetic behavior generally have ARM and SIRM demagnetization curves as shown in Figure F28C, F28D, and F28E. They are characterized by high coercive force (H_{cr}) and MDF values (Fig. F29C, F29D, F29E). Rapid decay of NRM, ARM, and SIRM and low values of H_{cr} usually indicate multidomain-like behavior (Fig. F29A, F29B, F29F).

In some samples (e.g., Samples 197-1205A-20R-6, 12–14 cm, and 35R-2, 36–38 cm) (Fig. F30), the NRM has an SD-like decay, whereas the ARM and SIRM demagnetization curves suggest that the behavior should be multidomain. The presence of superparamagnetic (SP) grains with sizes close to the SD/SP threshold (~30–50 nm) (Dunlop and Özdemir, 1997) might explain this discrepancy. In the presence of a magnetic field, the magnetization vector in an SD grain will rotate to align with the magnetic field. When the field is removed, the remanent magnetization will decay with time. The time it takes for an assemblage of SD grains to decay is called the relaxation time. Superparamagnetic grains have very short relaxation times compared to stable SD grains and typically carry an unstable magnetization in the presence of a magnetizing field. The rapid decay of the ARM and SIRM curves for the samples mentioned above might represent the unstable acquisition of magnetization in the SP grains. An alternative explanation for the data is that some samples have a mixture of large multidomain and single-domain grains. Detailed hysteresis measurements planned for shore-based study should help distinguish between these scenarios.

Magnetically "Soft" Components and Rock Alteration

Two types of AF demagnetization behavior observed in analyses of samples at this site merit additional rock magnetic consideration. Univectorial decay of remanence (e.g., Fig. F31F) is often observed, but samples with relatively large magnetically soft components (which are readily demagnetized up to 20 mT) were also seen (e.g., Fig. F31A, F31D). As the stable remanence of this site is characterized by a negative inclination, the NRM intensity may be reduced if the soft component is oriented in a direction roughly antiparallel to the primary remanence, as would be expected for a present-day viscous or Brunhes field overprint (e.g., Cottrell and Tarduno, in press). In this case, the decay curve of remanence with AF demagnetization will not be monotonic, and, therefore, the MDF may not be a useful measure of the hardness of magnetic remanence.

We calculate the vector difference between peak field AF demagnetization steps (here called ΔRM) to show the portion of the magnetically soft component relative to the intermediate coercive component as follows:

$$\Delta RM = (RM_0 - RM_5)/(RM_{20} - RM_{50}),$$

where,

T9. Rock magnetic parameters for basalt, p. 104.

F28. Lowrie-Fuller tests on basalt samples, p. 77.

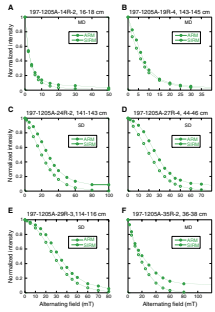

F29. IRM acquisition and demagnetization, p. 78.

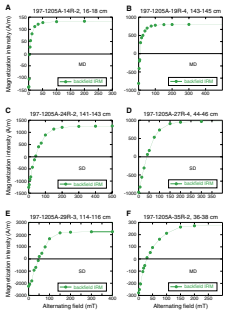

F30. Samples with possible superparamagnetic grains, p. 79.

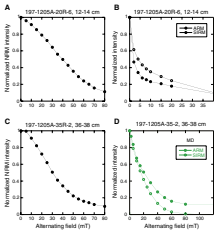

F31. Orthogonal vector plots of basalt, p. 80.

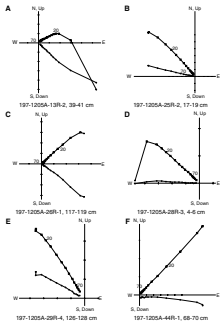

RM = the remanent vector,
$RM_0–RM_5$ = the vector difference between the untreated NRM and NRM after demagnetization at 5 mT, and
$RM_{20}–RM_{50}$ = the difference between the NRM after 20-mT treatment and NRM after 50-mT treatment.

We selected the interval between 20 and 50 mT as a basis for comparison because the stable remanent component was often isolated in this interval of AF demagnetization in samples from Site 1205. Figure F32 shows a positive correlation between the logarithm of ΔRM and the compressional wave velocity (V_P) measured on paleomagnetic samples with a PWS3 contact probe system (see "Physical Properties," p. 25). As V_P is a function of density and rigidity of the sample, this may indicate the degree of void space and chemical alteration, both of which may correlate with the amount of clay minerals. Samples having a relatively large magnetically soft component as characterized by the ΔRM factor appear to be less altered. Thermal demagnetization studies are needed to determine the magnetic unblocking temperatures and, hence, the magnetic mineralogy of the samples. Nevertheless, the degree of alteration appears to control the demagnetization behavior of some of the samples.

In general, the *Q*-ratios, median destructive field values, and results of the Lowrie-Fuller tests suggest that most of the recovered basalt samples preserve a primary magnetization suitable for paleolatitude analyses. The magnetic mineralogy of the Site 1205 basalt samples does not appear to be as variable or as altered as that of Sites 1203 and 1204 (see "Physical Volcanology and Igneous Petrology," p. 8, and "Alteration and Weathering," p. 18).

F32. ΔRM vs. compressional wave velocity, p. 81.

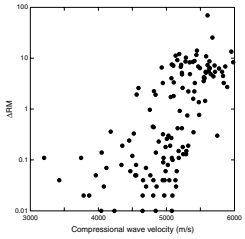

Paleomagnetism of Basalt

Twenty-five lava flows were recovered and sampled for paleomagnetic analysis. For most lava flows, four or more samples were measured. Where limited recovery occurred or a thin unit was cored (Units 1, 14b, 15b, 21, 22, 28a, 29b, and 30b), fewer samples were taken for shipboard analysis so that sufficient material would be available for high-resolution shore-based studies. Sample inclinations for each unit were averaged using the method of McFadden and Reid (1982).

Minicore samples of basalt from Site 1205 were measured using the 2-G Enterprises superconducting quantum interference device magnetometer. After the measurement of the untreated NRM, samples were progressively demagnetized by AF demagnetization. A 5-mT field increment was used between 5 and 70 mT. In addition, 80 mT was measured. A total of 152 basalt minicores were drilled.

Demagnetization Behavior

Orthogonal vector diagrams were used to characterize the demagnetization behavior and assess the number of magnetization components represented in the Site 1205 basalt samples. With few exceptions, samples showed stable demagnetization curves. Approximately one-third of the samples had a large normal polarity overprint that was removed after demagnetization to 25 mT (Fig. F33D, F33E). For 45% of the samples, AF demagnetization to 80 mT resulted in the reduction of intensity to <10% of the NRM (Fig. F31). Approximately 50% of samples were not demagnetized to <10% of the NRM intensity after treatment to 80 mT. Nevertheless, the remanence directions after each demagneti-

F33. Orthogonal vector plots of nonideal basalt, p. 82.

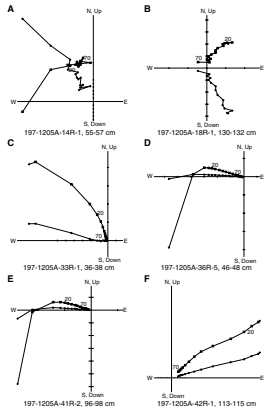

zation step define a clear trend toward the origin of orthogonal vector diagrams (Fig. F34). We attribute the failure of AF treatment at relatively high peak fields to adequately demagnetize the NRM to the presence of high-coercivity minerals. In some samples (Fig. F33C, F33F), the demagnetization vectors are curved at low-field steps, suggesting that two magnetic components are being demagnetized simultaneously. Five percent of samples did not have a stable remanence that could be fit with principal component analysis (Fig. F33A, F33B).

F34. Orthogonal vector plots of incompletely demagnetized basalt, p. 83.

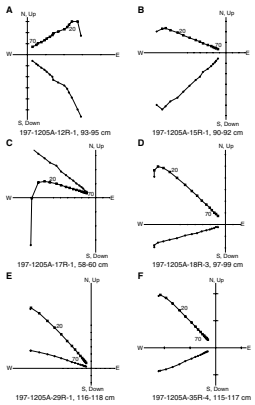

Characteristic Remanent Magnetization Directions

All samples analyzed were of reversed polarity; one apparent normal polarity sample (197-1205A-7R-2, 43–45 cm) was taken from a core catcher sample. The core piece may have been accidently inverted. The sedimentary column above the basalt flows is in nannofossil Zone NP10, which has an age range of ~53.5 to ~55 Ma (Berggren et al., 1995), corresponding to Chron 24r (Cande and Kent, 1995). Characteristic remanent magnetization directions were fit using principal component analysis (Kirschvink, 1980). In general, the characteristic remanent directions were defined between 20 and 70–80 mT for basalt samples that did not show a large normal polarity overprint. Samples with a large overprint were generally fit between 35 and 70–80 mT. Maximum angular deviations of line fits to the demagnetization data were generally <5°–10°.

Inferred Paleolatitudes and Discussion

Previous drilling on Nintoku Seamount at DSDP Site 432 penetrated 38 m of sandstone and basalt (Jackson, Koizumi, et al., 1980). Because Site 1205 is located ~100 m from Site 432, we can compare our results with those of Kono (1980), who analyzed the paleomagnetic record of DSDP Site 432. The first two basalt units identified at DSDP Site 432, which are the equivalent of a single basement unit at Site 1205 (see "Physical Volcanology and Igneous Petrology," p. 8), have inclination values of –65.2° and –66.4°. These yield a mean based on 13 samples that is shallower than that derived from the equivalent basement unit at Site 1205 (–72.0°), although the latter is based on only three samples and has a high uncertainty (±17.5°). We also note that the inclination values for DSDP Site 432 basalt flows were derived from the demagnetization step with minimum dispersion in inclination (Kono, 1980) rather than by principal component analysis. Unit 3 from DSDP Site 432 yielded an inclination (–28.6°) similar to that observed from the equivalent basement unit at Site 1205 (–29.5°).

Lava flows at Site 1205 that are separated by flow tops rather than soils (Units 15b, 16, and 17) (see "Physical Volcanology and Igneous Petrology," p. 8) may have been emplaced during relatively short periods with respect to time scales typical of secular variation (see "Paleomagnetism and Rock Magnetism," p. 23, in the "Explanatory Notes" chapter). We combine paleomagnetic data from such lava flows and treat other lava flows separated by soils as independent time units. This results in 22 paleomagnetic inclination groups (Table T10), which together (following the averaging method of McFadden and Reid, 1982) yield a mean inclination of –45.7° (95% confidence interval = +10.5°/–6.3°). The mean inclination indicates a paleolatitude of 27.1° (+10.8°/–5.2°).

T10. ChRM inclination averages and statistics, p. 105.

The estimated polar angular dispersion (S = 20.4°) (Cox, 1970; Tarduno and Sager, 1995) suggests that secular variation has been sampled. The value derived from the Site 1205 data is greater than expected using global reference curves (McFadden et al., 1991), which predict a value of S = 13.4° (+1.6°/–1.1°). The high dispersion is also apparent in the rather broad distribution of the inclination unit means (Fig. F35).

Several factors could account for the relatively high observed inclination dispersion. The most likely explanation, however, is that AF demagnetization is not adequately defining the characteristic remanent magnetization for some samples. This is supported by the rock magnetic and paleomagnetic evidence for high-coercivity magnetic minerals in some samples and the relatively high directional dispersion in some inclination units (Table T10). We also note that three inclination groups in our preliminary analysis are represented by only one or two samples because material was limited (Table T10). Shore-based analyses using thermal demagnetization should address these limitations.

The preliminary paleolatitude derived from the Site 1205 basalt samples differs from the present-day latitude of the Hawaiian hotspot (~19°). The data are similar to those obtained from paleomagnetic analysis of 65-Ma lava flows sampled at Suiko Seamount (DSDP Site 433) (Kono, 1980), a data set believed to average secular variation. Our data are preliminary, and therefore a determination of whether the paleolatitude of Nintoku Seamount during its formation is offset from the paleolatitude of Suiko Seamount is not possible; we expect the answer to this question will come from shore-based work employing thermal demagnetization procedures. Nevertheless, the paleomagnetic results from Site 1205 together with those from Suiko Seamount (Kono, 1980) and Detroit Seamount Sites 884 (Tarduno and Cottrell, 1997; Cottrell and Tarduno, in press), 1203, and 1204 form a consistent data set compatible with southward motion of the Hawaiian hotspot since the Late Cretaceous.

F35. Inclination of lava flows vs. Fisher distribution, p. 84.

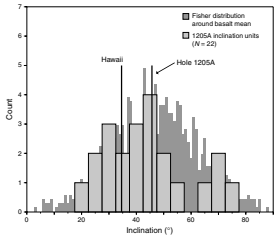

PHYSICAL PROPERTIES

All cores from Core 197-1205A-4R through 45R were run through the multisensor track (MST). For Sections 197-1205A-4R-1 and 5R-1, which contained sedimentary material, measurements were made of magnetic susceptibility, gamma ray attenuation (GRA) bulk density, and natural gamma radiation (NGR) on unsplit core sections. For Cores 197-1205A-5R-2 to 45R, which contained basement material, only NGR measurements were made on the MST on unsplit core sections. Index properties (bulk density, grain density, and porosity) and thermal conductivity were determined on discrete samples at a sampling frequency of one per core. Compressional wave velocities were measured at a sampling frequency of approximately one per section.

MST Measurements

Magnetic Susceptibility

Volume-normalized magnetic susceptibility was determined on core Sections 197-1205A-4R-1 and 5R-1 at 5-cm intervals (Table T11). Values generally range between ~300 × 10^{-6} and 1600 × 10^{-6} SI. A number of low values at 24.2, 24.4, 33.25, 33.5, and 33.85 mbsf appear to be due to voids in the liner, since there were also low GRA densities measured at

T11. Magnetic susceptibility, p. 106.

the same depths (see "GRA Density," p. 26). The highest value, at 24.75 mbsf at the base of Section 197-1205A-4R-1, could be attributed to drilling contamination. The remaining values increase with depth from ~700 × 10^{-6} to ~1300 × 10^{-6} SI in Section 197-1205A-4R-1 but remain relatively constant at ~1000 × 10^{-6} to 1100 × 10^{-6} SI in Section 197-1205A-5R-1.

GRA Density

Bulk density was measured by the GRA densitometer every 5 cm on whole-core Sections 197-1205A-4R-1 and 5R-1 (Table T12). Low density values at 24.2, 24.4, 33.25, 33.5, and 33.85 mbsf probably reflect voids in the liner. A general increase with depth from ~1.5 to ~2 g/cm³ was observed in Section 197-1205A-4R-1, but values remain relatively constant at ~2 g/cm³ in Section 197-1205A-5R-1.

T12. GRA bulk density, p. 107.

Natural Gamma Radiation

NGR was measured every 10 cm on both unsplit sediment and basalt cores from Hole 1205 (Table T13; Fig. F36A). Total counts are reported here because the corrected counts (which are less by ~16 counts per second [cps]) include negative values that are physically unreasonable. The sediment section in Hole 1205A consists of fossiliferous sandstones and a basalt conglomerate (see "Lithostratigraphy," p. 5). For the sandstones, NGR values between 17 and 25 cps were measured (mean = 20 cps). For the basalt conglomerate, NGR values between 17 and 32 cps were measured (mean = 22 cps).

In the basement, total NGR counts varied between 12 and 39 cps. The data points show considerable variation with depth. High NGR counts of ~31 cps in basement Units 1, 2, and 3 at depths >79.2 mbsf are followed by a rather abrupt decrease to ~16 cps at ~84 mbsf. These lower gamma ray values are present at the base of basement Subunit 3b (see "Physical Volcanology and Igneous Petrology," p. 8). Below 90 mbsf, NGR counts again increase to ~26 cps at ~110 mbsf then gradually decrease again to ~19 cps at ~180 mbsf. This is followed by a slight increase to ~22 cps at ~225 mbsf. At ~242 mbsf, total NGR counts decrease rapidly to ~14 cps; these low gamma ray values are present in basement Subunits 19a and 19b, a weathered flow top and moderately to highly olivine-phyric basalt (see "Physical Volcanology and Igneous Petrology," p. 8). At depths >250 mbsf, NGR counts are higher again and remain so to the base of the hole, ranging from ~20 to 30 cps.

T13. Natural gamma ray measurements, p. 108.

F36. Physical properties, p. 85.

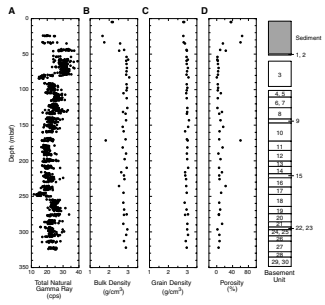

Core Imaging

Whole-round core images were taken of cylindrical pieces from the Hole 1205A core. Owing to the massive nature of many of the recovered core pieces, 153 m of images was recorded, representing ~93% of the recovered material. However, because of an obstruction, downhole logging was canceled. Hence, correlation of core image and logging data is not possible at this site.

Thermal Conductivity

Thermal conductivity was measured at a frequency of one per core from Cores 197-1205A-5R through 45R. Cores 197-1205A-1R through 4R did not contain suitable samples for thermal conductivity measure-

ment. For the sample from Core 197-1205A-5R, a basalt cobble/boulder conglomerate, a value of 1.331 W/(m·K) was measured. All other measurements were made on basalt samples. For these, thermal conductivity values ranged from 1.515 to 1.985 W/(m·K) (average = 1.70 W/[m·K]) (Table T14; Fig. F37). Particularly high thermal conductivity was recorded in samples from basement Units 3, 10, 13, 16, and 22.

T14. Thermal conductivity, p. 109.

F37. Thermal conductivity, p. 86.

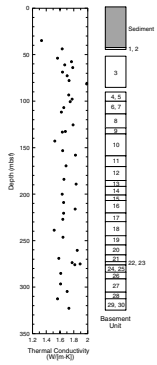

Index Properties

Index properties of sediments were determined on two discrete samples from Core 197-1205A-2R and one sample from each of Cores 197-1205A-4R and 5R. There were no suitable samples in Cores 197-1205A-1R and 3R. In the basement units from Cores 197-1205A-5R through 45R, index properties were usually determined on one sample per core. Uncommonly, more than one sample per core was taken if different lithologies were present in the recovered core. Values of wet mass, dry mass, and dry volume of the samples were measured and used to calculate moisture content, bulk density, grain density, and porosity (Table T15; Fig. F36B, F36C, F36D).

For all four sediment samples, grain densities between 2.78 and 2.83 g/cm³ were determined. However, porosity for the samples from Cores 197-1205A-4R and 5R is much higher (64% and 60%, respectively) than samples from Core 197-1205-2R (35% and 37%). Consequently, bulk density in Cores 197-1204A-4R and 5R is much lower (1.65 and 1.74 g/cm³, respectively) than in Core 197-1205A-2R (2.14 and 2.19 g/cm³). In Cores 197-1205A-4R and 5R, bulk density values are somewhat lower (~10% to 20%) than the GRA density at the respective depths. GRA density was not measured in Core 197-1205-2R.

In the basement, bulk density ranges from 2.52 to 3.06 g/cm³ for the basalt samples (mean = 2.83 g/cm³). Low bulk density (1.82 g/cm³) was recorded in a soil horizon/weathered flow top from basement Unit 12a (see **"Physical Volcanology and Igneous Petrology,"** p. 8); this sample also has correspondingly high porosity (~60%). For the remainder of the basement samples, all of which were taken from basalt sections, bulk density shows very little systematic variation with depth. Grain density also varies very little downhole, ranging from 2.85 to 3.08 g/cm³ (mean = 2.97 g/cm³). Porosity in the basement section of Hole 1205A is relatively low, generally ranging from 0% to 22.6% (mean = 7.2%). It shows very little systematic variation with depth.

T15. Index properties, p. 110.

Compressional Wave Velocity

Compressional wave velocity was determined in the x-direction for two split-core sediment sections from Hole 1205A (Sections 197-1205A-4R-1 and 5R-1) and for two sediment pieces from Core 197-1205A-2R. In these four sediment samples, *P*-wave velocities range from ~1774 to 2710 m/s (mean = 2322 m/s).

For basement material, compressional wave velocity measurements were made on approximately one discrete sample per section. *P*-wave velocity was measured in the x- and z-directions for the basement samples. On selected samples, *P*-wave velocity was also measured in the y-direction. *P*-wave velocity ranges from ~3200 to 6000 m/s (mean = ~5100 m/s) (Table T16; Fig. F38). Velocities determined in the x-, y-, and z-directions differ by up to 300 m/s, and it is not immediately apparent whether this relates to anisotropy or to the difference in quality of coupling between sampling and transducers described in previous

T16. Compressional wave velocity, p. 111.

F38. Compressional wave velocity, p. 87.

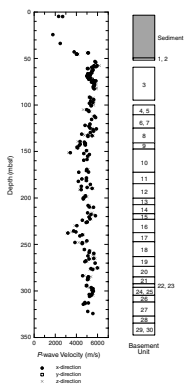

site chapters. In the upper part of the basement, from ~50 to 135 mbsf, velocity is relatively high. The decrease in velocity toward the center of basement Unit 3 may be related to an increase in devitrification (see "Physical Volcanology and Igneous Petrology," p. 8). Similarly, but less clearly, this tendency of velocity to decrease toward the center of a unit can also be seen in basement Units 6, 8, 10, and 18, whereas basement Unit 27 shows the opposite trend. Other basement units are thinner, and, hence, fewer samples were measured and no trends were apparent.

At ~135 mbsf, the base of Unit 9, velocity decreases slightly. Highly variable velocity was recorded in basement Unit 10, ranging from 3425 to 5228 m/s; this may reflect variable amounts of vesicles in the unit. Velocity then shows a slight increase with depth until ~225 mbsf, where a sharp decrease in velocity is observed. Particularly low velocity (<4000 m/s) was recorded in basement Unit 18 (predominantly aphyric to moderately olivine-phyric basalt), which is probably due to its high vesicularity (see "Physical Volcanology and Igneous Petrology," p. 8). From ~245 to 278 mbsf, an increase in *P*-wave velocity with depth is observed, the highest values occurring in basement Unit 22, a moderately olivine-plagioclase-phyric basalt; elevated thermal conductivity was also recorded in this unit (see above). Lower velocity was recorded in basement Units 24 to 26, which include aphyric basalt breccias (see "Physical Volcanology and Igneous Petrology," p. 8). Slightly higher velocity (~5760 m/s) is present throughout basement Unit 27, an aphyric to moderately plagioclase-phyric basalt.

At Site 1205, *P*-wave velocities were measured on all minicores drilled for paleomagnetic measurement and index properties were frequently determined on chips left after cutting of paleomagnetism minicore samples; therefore, it was possible to compare bulk densities and *P*-wave velocities at the same sampling depth (Fig. F39). *P*-wave velocity and bulk density data appear to be correlated:

$$(\Delta\rho/\rho)/(\Delta V_p/V_p) = \sim 0.4.$$

A possible explanation for this relationship is that high vesicularity causes both low bulk density and low seismic velocity. This interpretation is further supported by the absence of any obvious relationship between grain density and *P*-wave velocity.

F39. Compressional wave velocity vs. bulk density, p. 88.

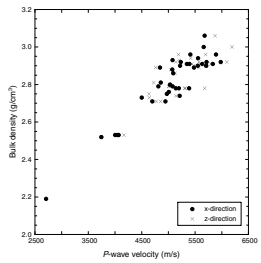

UNDERWAY GEOPHYSICS

Seismic Reflection Profiling

Initial selection of proposed Site HE-4A, which became Site 1205, was based on data gathered at DSDP Site 432, where basement was reached at ~42 mbsf (Jackson, Koizumi, et al., 1980). We conducted a single-channel seismic profile, 3.5-kHz PDR, and magnetometer survey in the vicinity of Site 432 to ensure proper hole location and suitability for basement drilling. Analog seismic data (*Glomar Challenger,* 8 August 1977, 2230 hr Universal Time Coordinated [UTC], and *S.P. Lee,* 8-76-NP, 8 October 1976, 2230 hr UTC) were acquired in the vicinity of Site 432. Figure F40 shows the track line of the Leg 197 survey superimposed on ETOPO5 seafloor bathymetry with a contour interval of 100 m. Tick marks along our survey lines mark half-hour intervals. Line 1 is approximately in the same location and azimuth as the *S.P. Lee* 8-76-NP line.

F40. Site 1205 seismic reflection, p. 89.

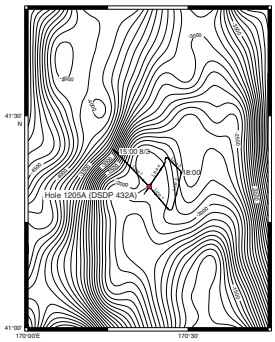

Survey Lines 1 and 4 pass directly over Site 1205, which is 100 m southeast of DSDP Site 432. Approximately 3-km-long sections from Lines 1 and 4 are shown in Figures **F41** and **F42,** respectively. The midpoint of the active portion of the streamer was ~218 m astern of the water gun source, which was ~4.5–6 m deep. The midpoint between the active section of the streamer and the water gun source was ~191 m astern of the ship's recorded GPS position. Firing of the water gun was set at every 4 s. Each shot record is 3 s in record length, beginning 100 ms before the water gun was triggered. This 100-ms delay, created by the trigger control panel, was removed in SIOSEIS record processing. Ship speed averaged 5.12 kt (2.77 m/s) during Line 1 and 4.57 kt (2.48 m/s) during Line 3. All three lines were processed with SIOSEIS seismic processing software (version 2001.3) (**http://sioseis.ucsd.edu**), using predictive deconvolution, bandpass filtering from 60–150 Hz, and Fk-migration with a velocity of 2000 m/s. Table **T17** shows the SIOSEIS script processing parameters for each line.

At Site 1205, a thin sequence of sediment overlies the volcanic basement. A strongly coherent reflection at 1.81 s two-way traveltime (TWT) marks the contact between the ~40-m-thick sediment and the basement. This contact, dipping to the west, shows little relief except for a shallow trough seen on Line 4. The truncation of dipping lava flows beneath the sediment/basement contact suggests an erosional unconformity (Fig. **F42**). The lack of lateral coherence of the seafloor reflector is possibly due to very low velocity sediment producing a velocity gradient relative to the seawater velocity.

Two different types of basement are present in the vicinity of Site 1205, producing distinctly different seismic signatures. The upper sequence of dominantly alkalic basalt lava flow units interbedded with soil layers (see **"Physical Volcanology and Igneous Petrology,"** p. 8) produces laterally coherent, low-frequency, and west-dipping reflections beneath the sediment layer. This section was penetrated in Hole 1205A, at ~1.88 s TWT. Basement underlying this soil-lava sequence, which appears to be more massively bedded given its lack of laterally coherent internal reflectivity, rises gently upward to the southeast. The strongly reflective upper sequence of lava flows and soil interbeds continues to thin to the southeast until it is only ~0.02 s TWT thick at shotpoint 1431 on Line 1 (Fig. **F41**). The prominent rise in the top of the lower incoherently reflective basement at shotpoint 1351 (Fig. **F41**) does not appear to be fault controlled and is more likely an erosional or constructional surface. The change in acoustic character of the basement sequences might be related to soil horizons occurring far less commonly below Core 197-1205A-29R (~203 mbsf) than above this depth, which corresponds to ~1.88 s TWT.

The boundary in the two types of basement might mark the top of dominantly tholeiitic flow units, having higher eruption rates, and thus leaving less time for the formation of soil horizons and interbedded sediment necessary to produce the layered character of the upper basement section.

F41. Fk-migrated section of survey Line 1, p. 90.

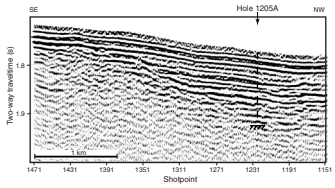

F42. Fk-migrated section of survey Line 4, p. 91.

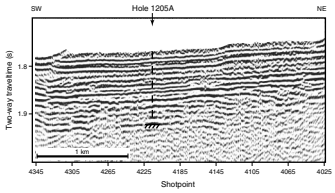

T17. SIOSEIS process parameter, p. 112.

REFERENCES

Alt, J.C., 1995. Subseafloor processes in mid-ocean ridge hydrothermal systems. *In* Humphris, S.E., Zierenberg, R., Mullineaux, L., and Thomson, R. (Eds.), *Seafloor Hydrothermal Systems: Physical, Chemical, Biological and Geological Interactions within Hydrothermal Systems*. Geophys. Monogr., Am. Geophys. Union, 91:85–114.

Augustithis, S.S., 1979. The mineralogical and geochemical distribution of sulphides in basic and ultrabasic rocks. *In Atlas of the Textural Patterns of Basic and Ultrabasic Rocks and their Genetic Significance:* Berlin (Walter de Gruyter), 83–85.

Barton, C.E., Baldwin, R.T., Barraclough, D.R., et al., 1995. International Geomagnetic Reference Field, 1995 revision presented by IAGA Division V, Working Group 8. *Phys. Earth Planet. Int.,* 97:23–26.

Berggren, W.A., Kent, D.V., Swisher, C.C., III, and Aubry, M.-P., 1995. A revised Cenozoic geochronology and chronostratigraphy. *In* Berggren, W.A., Kent, D.V., Aubry, M.-P., and Hardenbol, J. (Eds.), *Geochronology, Time Scales and Global Stratigraphic Correlation*. Spec. Publ.—Soc. Econ. Paleontol. Mineral., 54:129–212.

Buddington, A.F., and Lindsley, D.H., 1964. Iron-titanium oxides minerals and synthetic equivalents. *J. Petrol.,* 5:310–357.

Cande, S.C., and Kent, D.V., 1995. Revised calibration of the geomagnetic polarity timescale for the Late Cretaceous and Cenozoic. *J. Geophys. Res.,* 100:6093–6095.

Clague, D.A., and Dalrymple, G.B., 1989. Tectonics, geochronology, and origin of the Hawaiian-Emperor volcanic chain. *In* Winterer, E.L., Hussong, D.M., and Decker, R.W. (Eds.), *The Eastern Pacific Ocean and Hawaii*. Geol. Soc. Am., Geol. of North America Ser., N:188–217.

Cottrell, R.D., and Tarduno, J.A., in press. A Late Cretaceous pole for the Pacific plate: implications for apparent and true polar wander and the drift of hotspots. *Tectonophysics*.

Cox, A.V., 1970. Latitude dependence of the angular dispersion of the geomagnetic field. *Geophys. J. R. Astron. Soc.,* 20:253–269.

Dalrymple, G.B., Greene, H.G., Ruppel, B.D., Bear, T.E., and Clague, D.A., 1980a. Pre-Leg 55 site survey geophysical data from R/V *S.P. Lee* cruise LEE8-76-NP. *In* Jackson, E.D., Koizumi, I., et al., *Init. Repts. DSDP,* 55: Washington (U.S. Govt. Printing Office), 801–844.

Dalrymple, G.B., Lanphere, M.A., and Clague, D.A., 1980b. Conventional and $^{40}Ar/^{39}Ar$ K-Ar ages of volcanic rocks from Ojin (Site 430), Nintoku (Site 432) and Suiko (Site 433) seamounts and the chronology of volcanic propagation along the Hawaiian-Emperor Chain. *In* Jackson, E.D., Koizumi, I., et al., *Init. Repts. DSDP,* 55: Washington (U.S. Govt. Printing Office), 659–676.

Dunlop, D.J., and Özdemir, Ö., 1997. *Rock Magnetism: Fundamentals and Frontiers:* Cambridge (Cambridge Univ. Press).

Fisher, R.A., 1953. Dispersion on a sphere. *Proc. R. Soc. London A,* 217:295–305.

Frey, F.A, Garcia, M.O., and Roden, M.F., 1994. Geochemical characteristics of Koolau Volcano: implications of intershield geochemical differences among Hawaiian volcanoes. *Geochim. Cosmochim. Acta,* 58:1441–1462.

Frey, F.A., Garcia, M.O., Wise, W.S., Kennedy, A., Gurriet, P., and Albarede, F., 1991. The evolution of Mauna Kea Volcano, Hawaii: petrogenesis of tholeiitic and alkalic basalts. *J. Geophys. Res.,* 96:14347–14375.

Frey, F.A., and Rhodes, J.M., 1993. Intershield geochemical differences among Hawaiian volcanoes: implications for source compositions, melting process and magma ascent paths. *Phil. Trans. R. Soc. Lond.,* A342:121–126.

Frey, F.A., Wise, W.S., Garcia, M.O., West, H., Kwon, S.-T., and Kennedy, A., 1990. Evolution of Mauna Kea Volcano, Hawaii: petrologic and geochemical constraints on postshield volcanism. *J. Geophys. Res.,* 95:1271–1300.

Greene, H.G., Clague, D.A., and Dalrymple, G.B., 1980. Seismic stratigraphy and vertical tectonics of the Emperor Seamounts, DSDP Leg 55. *In* Jackson, E.D., Koizumi, I., et al., *Init. Repts., DSDP,* 55: Washington (U.S. Govt. Printing Office), 759–788.

Haggerty, S.E., 1991. Oxide textures: a mini-atlas. *In* Lindsley, D.H. (Ed.), *Oxide Minerals: Petrologic and Magnetic Significance.* Rev. Mineral., 25:129–219.

Hon, K., Kauahikaua, J.P., Denlinger, R., and Mackay, K., 1994. Emplacement and inflation of pahoehoe sheet flows: observations and measurements of active lava flows on Kilauea, Hawaii. *Geol. Soc. Am. Bull.,* 106:351–370.

Jackson, E.D., Koizumi, I., et al., 1980. *Init. Repts. DSDP,* 55: Washington (U.S. Govt. Printing Office).

Keszthelyi, L., McEwen, A.S., and Thordarson T., 2000. Terrestrial analogs and thermal models for Martian flood lavas. *J. Geophys. Res.,* 105:15027–15049.

Keszthelyi, L., and Thordarson, T., 2000. Rubbly pahoehoe: a previously undescribed but widespread lava type transitional between a'a and pahoehoe, *Geol. Soc. Am. Abstr. Progr.,* 32:7.

Kirkpatrick, R.J., Clague, D.A., and Freisen, W., 1980. Petrology and geochemistry of volcanic rocks, DSDP Leg 55, Emperor Seamount Chain. *In* Jackson, E.D., Koizumi, I., et al., *Init. Repts. DSDP,* 55: Washington (U.S. Govt. Printing Office), 509–557.

Kirschvink, J.L., 1980. The least-squares line and plane and the analysis of palaeomagnetic data. *Geophys. J. R. Astron. Soc.,* 62:699–718.

Kono, M., 1980. Paleomagnetism of DSDP Leg 55 basalts and implications for the tectonics of the Pacific plate. *In* Jackson, E.D., Koizumi, I., et al., *Init. Repts. DSDP,* 55: Washington (U.S. Govt. Printing Office), 737–752.

Lowrie, W., and Fuller, M., 1971. On the alternating field demagnetization characteristics of multidomain thermoremanent magnetization in magnetite. *J. Geophys. Res.,* 76:6339–6349.

Macdonald, G.A., and Katsura, T., 1964. Chemical composition of Hawaiian lavas. *J. Petrol.,* 5:82–133.

McFadden, P.L., Merrill, R.T., McElhinny, M.W., and Lee, S., 1991. Reversals of the Earth's magnetic field and temporal variations of the dynamo families. *J. Geophys. Res.,* 96:3923–3933.

McFadden, P.L., and Reid, A.B., 1982. Analysis of paleomagnetic inclination data. *Geophys. J. R. Astron. Soc.,* 69:307–319.

McKenzie, J., Bernoulli, D., and Schlanger, S.O., 1980. Shallow-water carbonate sediments from the Emperor Seamounts: their diagenesis and paleogeographic significance. *In* Jackson, E.D., Koizumi, I., et al., *Init. Repts DSDP,* 55: Washington (U.S. Govt. Printing Office), 415–455.

Peterson, D.W., and Tilling, R. I., 1980. Transition of basaltic lava from pahoehoe to aa, Kilauea Volcano, Hawaii: field observations and key factors. *J. Volcanol. Geotherm. Res.* 7:271–293.

Rhodes, J.M., 1996. Geochemical stratigraphy of lava flows sampled by the Hawaii Scientific Drilling Project. *J. Geophys. Res.,* 101:11769–11780.

Self, S., Keszthelyi, L., and Thordarson, T., 1998. The importance of pahoehoe. *Ann. Rev. Earth Planet. Sci,* 26:81–110.

Shipboard Scientific Party, 1980. Site 432: Nintoku Seamount. *In* Jackson, E.D., Koizumi, I., et al., *Init. Repts., Deep Sea Drilling Project,* 55: Washington (U.S. Govt. Printing Office), 95–125.

————, 1998. Explanatory Notes. *In* Wefer, G., Berger, W.H., and Richter, C., et al., *Proc. ODP, Init. Repts.,* 175: College Station, TX (Ocean Drilling Program), 27–46.

Siesser, W.G., Bralower, T.J., and De Carlo, E.H., 1992. Mid-Tertiary *Braarudosphaera*-rich sediments on the Exmouth Plateau. *In* von Rad, U., Haq, B.U., et al., *Proc. ODP, Sci. Results,* 122: College Station, TX (Ocean Drilling Program), 653–663.

Tarduno, J.A., and Cottrell, R.D., 1997. Paleomagnetic evidence for motion of the Hawaiian hotspot during formation of the Emperor Seamounts. *Earth Planet. Sci. Lett.,* 153:171–180.

Tarduno, J.A., and Sager, W.W., 1995. Polar standstill of the mid-Cretaceous Pacific plate and its geodynamic implications. *Science,* 269:956–959.

Thordarson, T., and Self, S., 1998. The Roza Member, Columbia River Basalt Group—a gigantic pahoehoe lava flow field formed by endogenous processes. *J. Geophys. Res.,* 103:27411–27445.

Waychunas, G.A., 1991. Crystal chemistry of oxides and oxyhydroxides. *In* Lindsley, D.H. (Ed.), *Oxide Minerals: Petrologic and Magnetic Significance.* Rev. Mineral., 25:11–68.

West, H.B., Garcia, M.O., Frey, F.A., and Kennedy, A., 1988. Nature and cause of compositional variation among the alkalic cap lavas of Mauna Kea Volcano, Hawaii. *Contrib. Mineral. Petrol.,* 100:383–397.

Yang, H.-J., Frey, F.A., Rhodes, J.M., and Garcia, M.O., 1996. Evolution of Mauna Kea Volcano: inferences from lava compositions recovered in the Hawaii Scientific Drilling Project. *J. Geophys. Res.,* 101:11747–11767.

Figure F1. Bathymetry in the region of Nintoku Seamount, central Emperor Seamount chain, from ETOPO2 database. Shown are the *S.P. Lee* cruise LEE8-76-NP seismic reflection survey track line and the locations of DSDP Site 432 and Ocean Drilling Program (ODP) Site 1205 (41°20.0′N, 170°22.7′E).

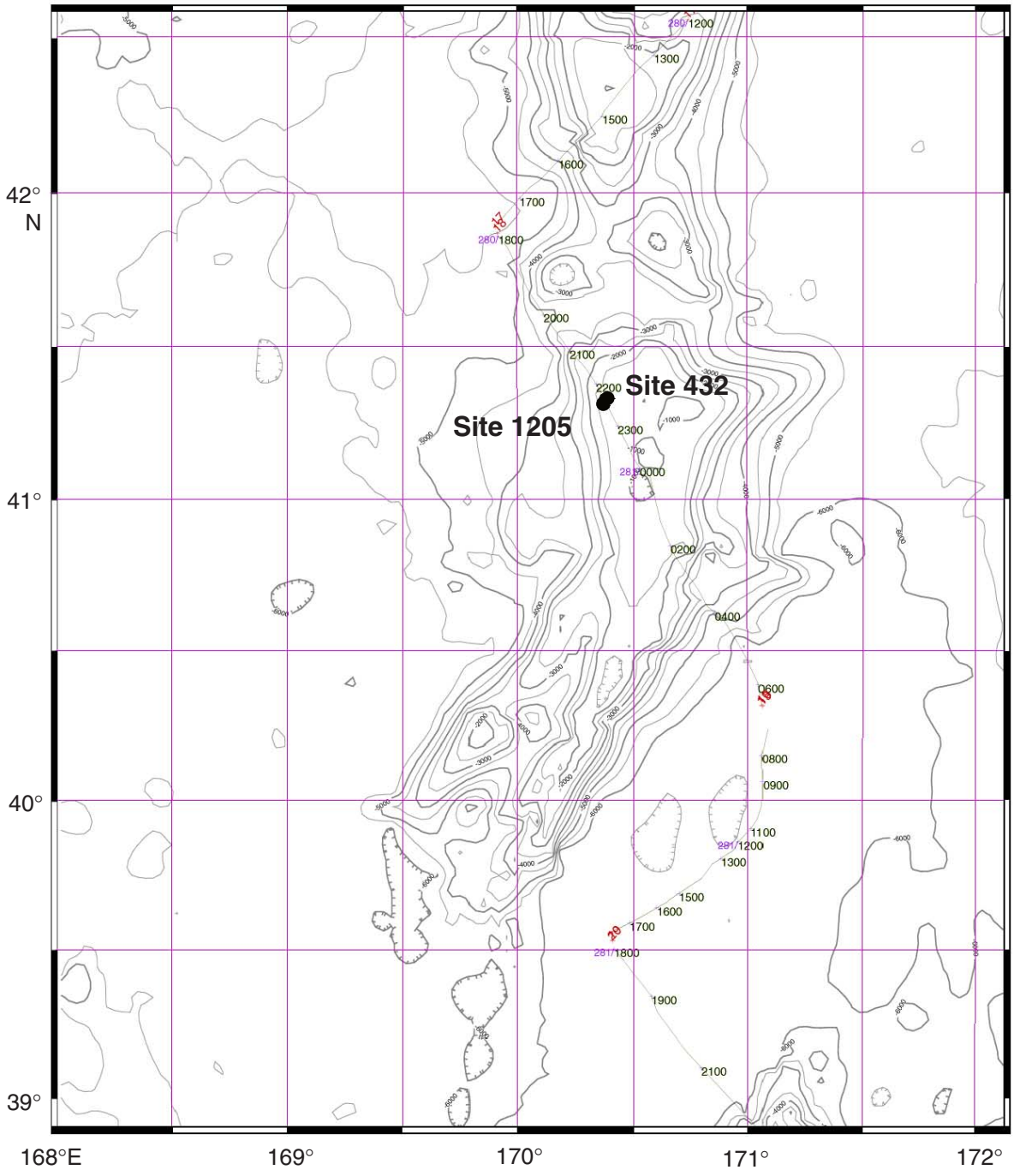

Figure F2. Sedimentary units in Hole 1205A.

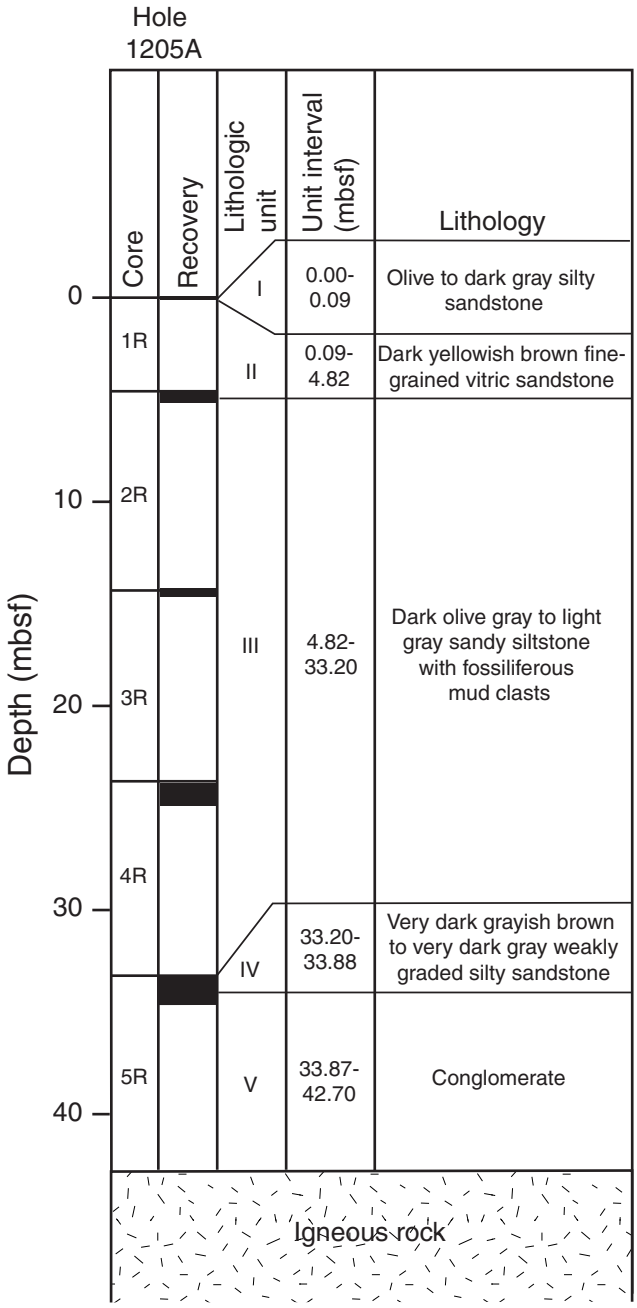

Figure F3. Chemical analyses of carbonate at Site 1205.

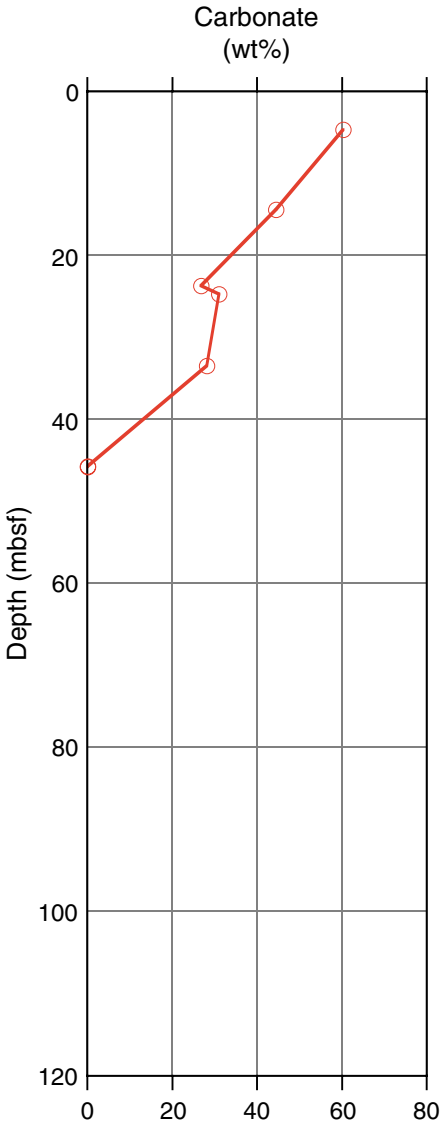

Figure F4. Downhole variation of sedimentary components from smear slide analysis. **A.** Total carbonate, organic calcite including bioclasts, feldspar, and volcanic ash. **B.** Phillipsite, Fe oxide, and opaque minerals.

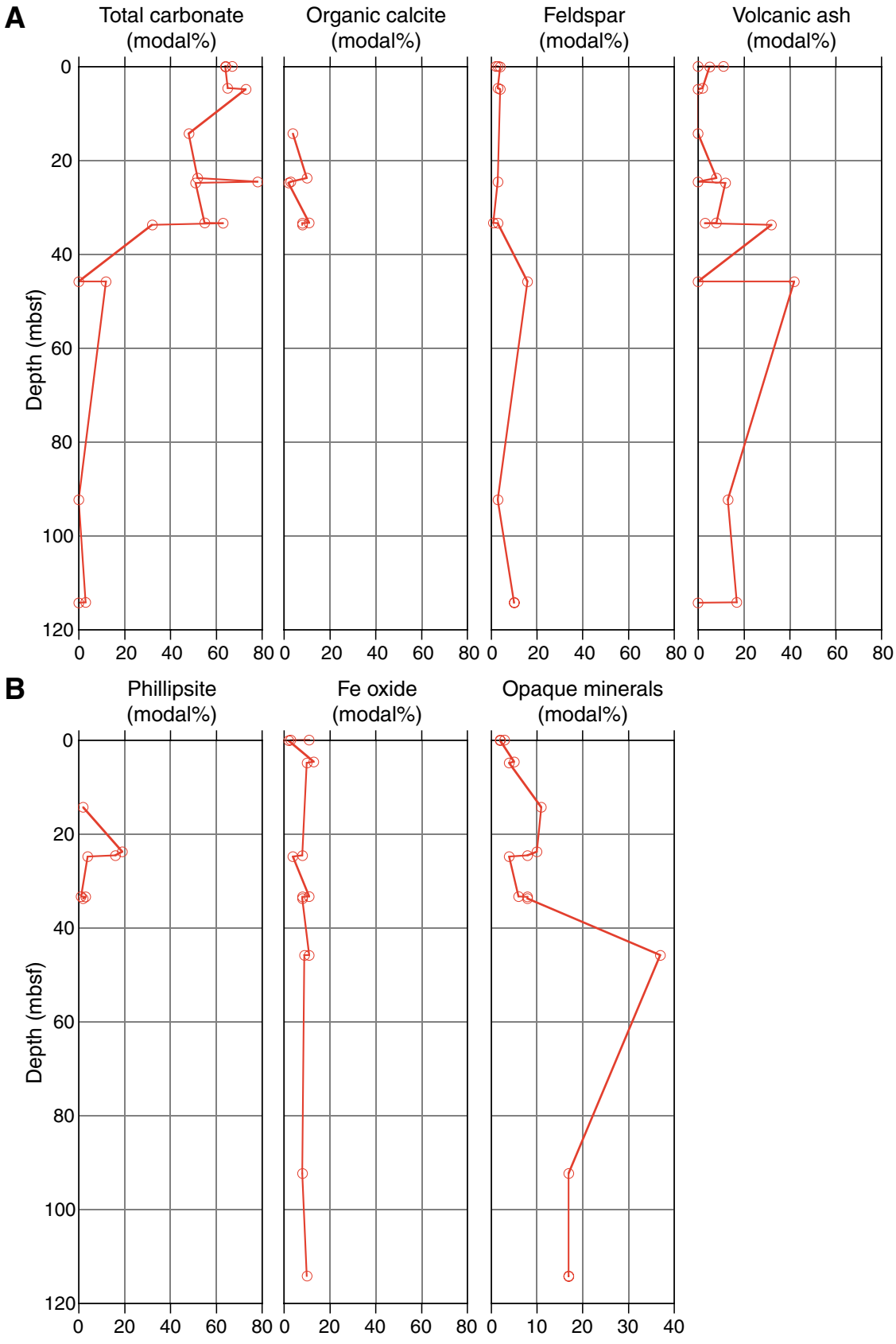

Figure F5. A. Photomicrograph of red algae, bryozoan, and bivalve assemblage (interval 197-1205A-1R-1, 5–8 cm) (scale bar = 150 µm). **B.** Close-up photograph of calcareous conglomerate (interval 197-1205A-5R-2, 12–20 cm) (scale bar = 2.75 cm).

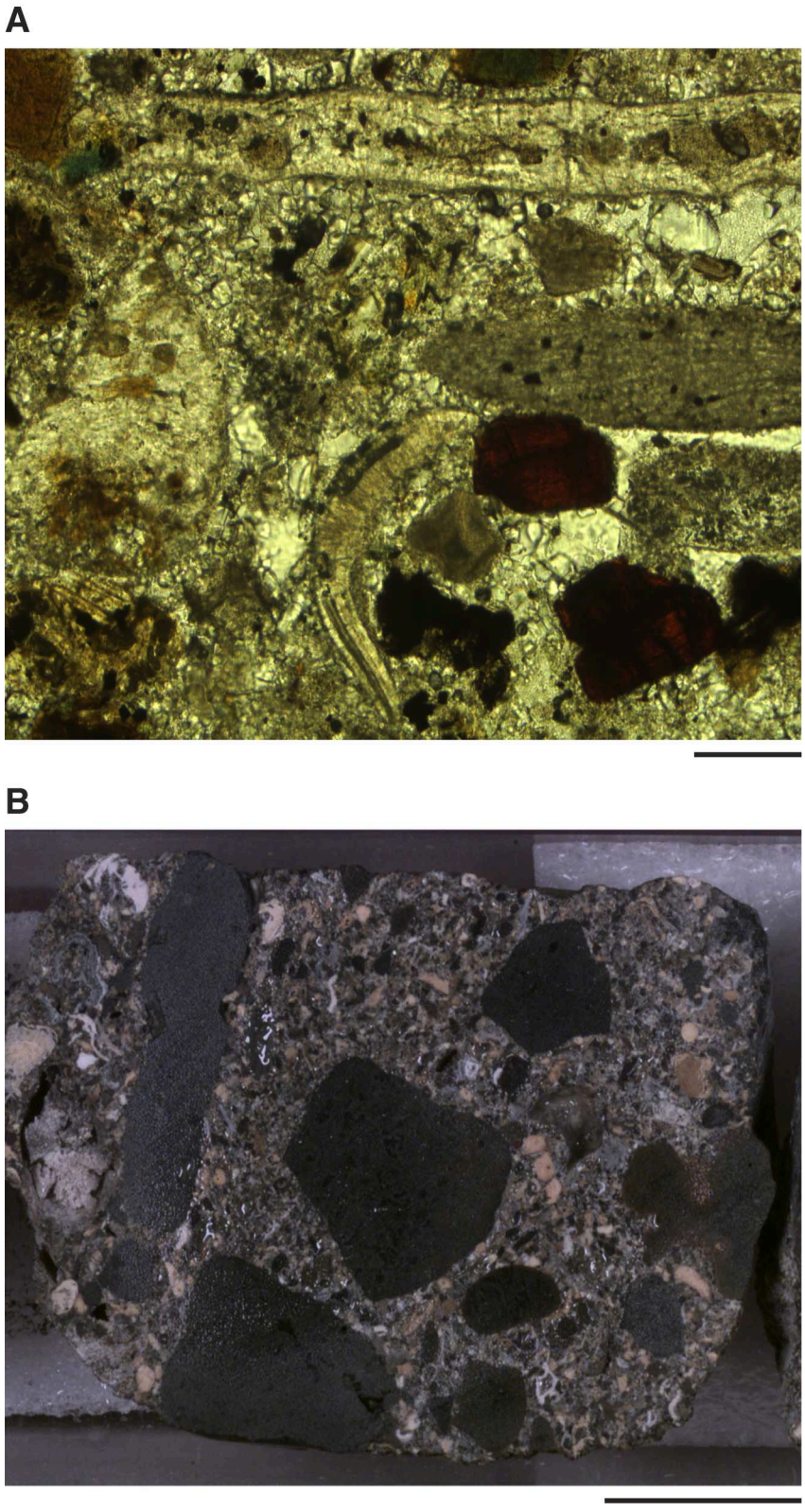

Figure F6. Calcareous nannofossil zonation in Hole 1205A, plotted against core recovery and epochs. Positions of zonal boundaries are only approximate, owing to the scale of the diagram. See **"Zonation,"** p. 7, in "Calcareous Nannofossils" in "Biostratigraphy" for accurate positions of boundaries.

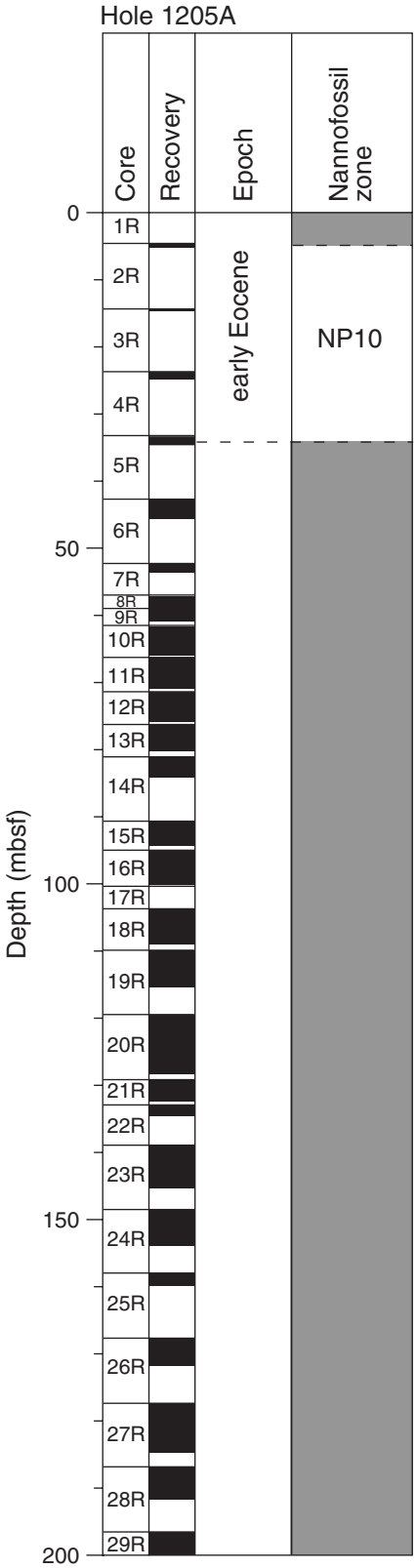

Figure F7. Diagram summarizing the recovery, thickness, chemical composition, and major lithologic features of the basement units from Hole 1205A.

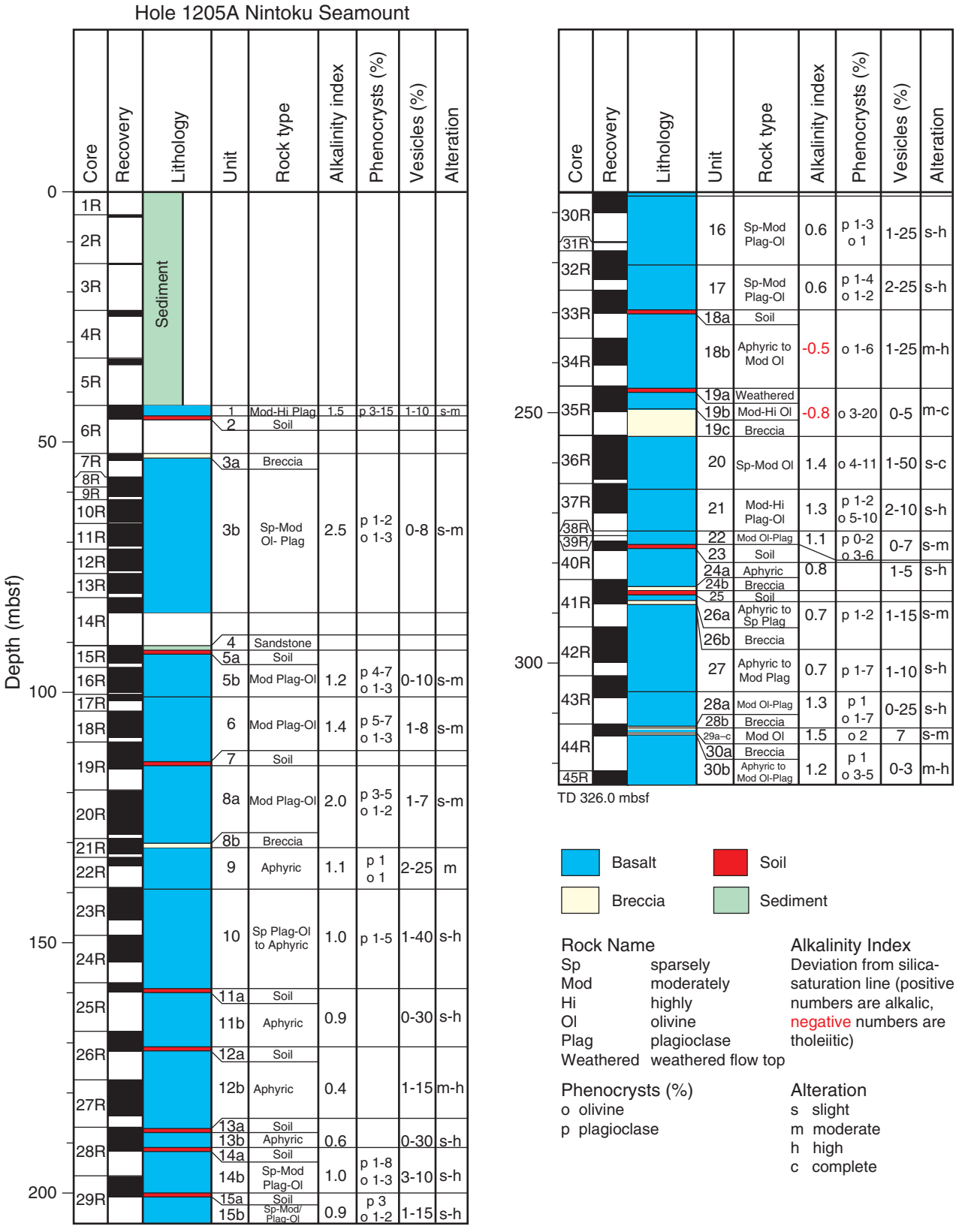

Figure F8. Photograph showing red clay soil of Unit 7 and relatively unweathered basalt units immediately above (to the left) and below (interval 197-1205A-19R-4, 8–25 cm).

Figure F9. Photograph showing highly plagioclase-phyric alkali basalt of basement Unit 1 (interval 197-1205A-6R-1, 8–36 cm).

Figure F10. Photograph showing basal breccia of plagioclase-olivine-phyric basalt (Subunit 8b) overlying the weathered and rubbly top of an aphyric basalt flow (Unit 9) (interval 197-1205A-21R-2, 25–46 cm).

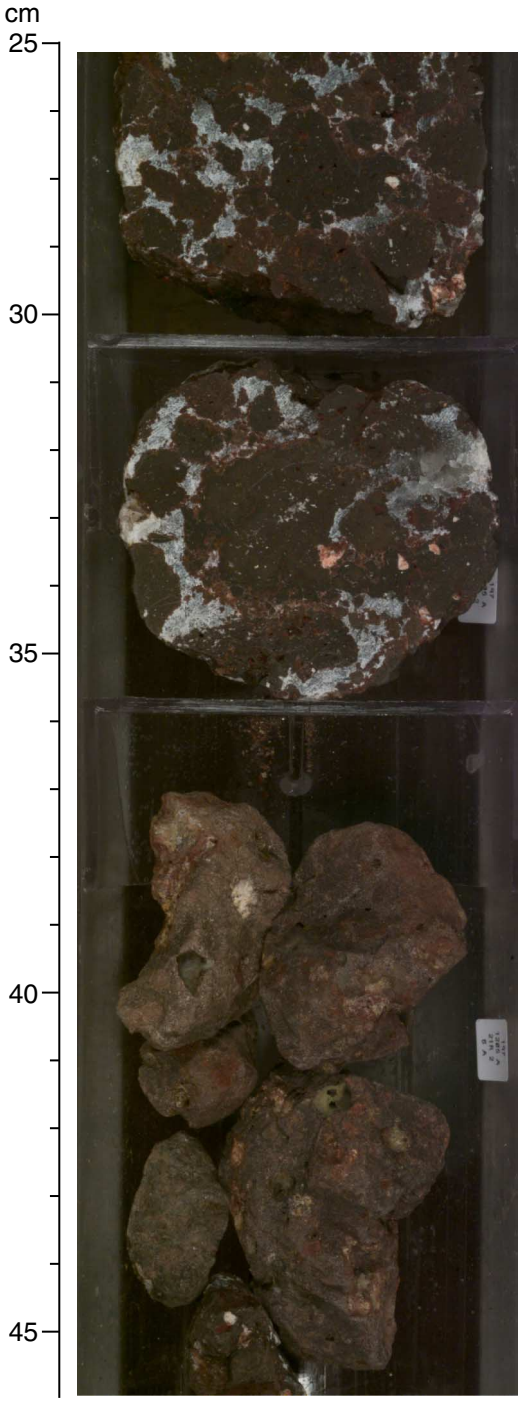

Figure F11. Photograph of conglomerate overlying basement showing clasts of hawaiite up to 8 cm in diameter embedded in a poorly sorted, fossiliferous sandy matrix (interval 197-1205A-5R-2, 9–25 cm).

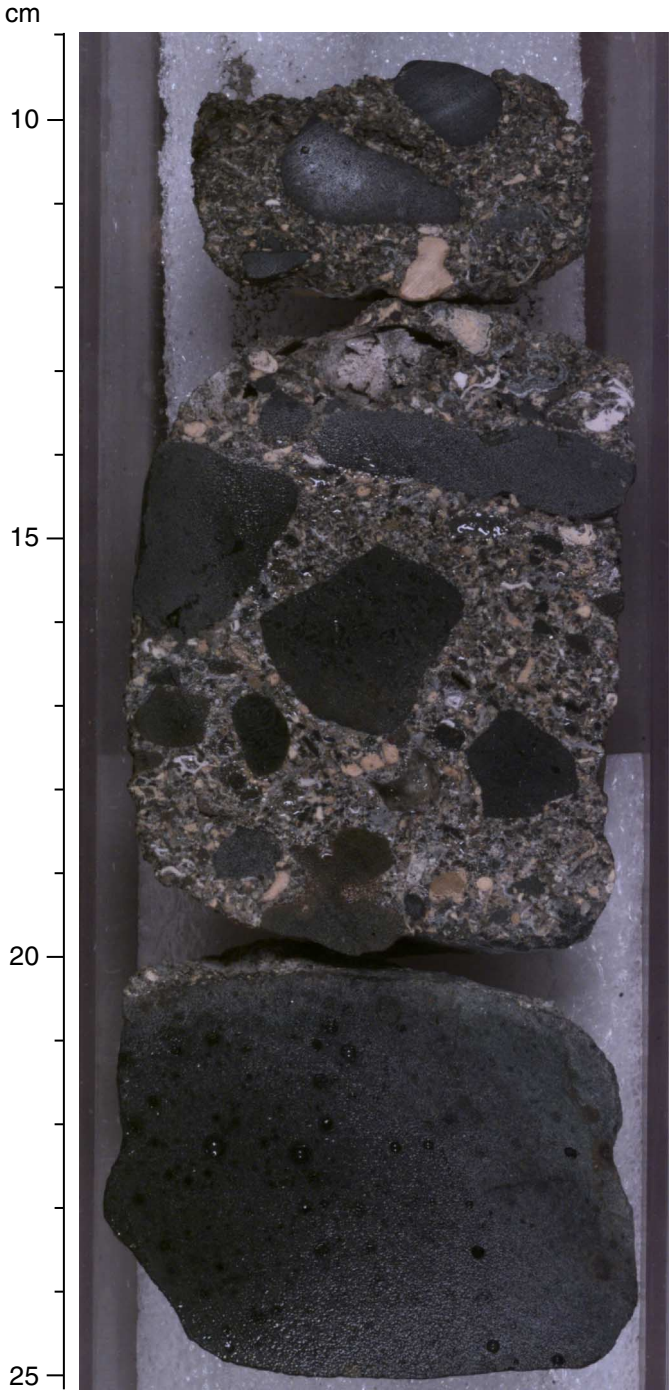

Figure F12. Photograph showing red clay soil (Subunit 12a) overlying the weathered flow top of Subunit 12b (aphyric basalt) (interval 197-1205A-26R-3, 92–112 cm).

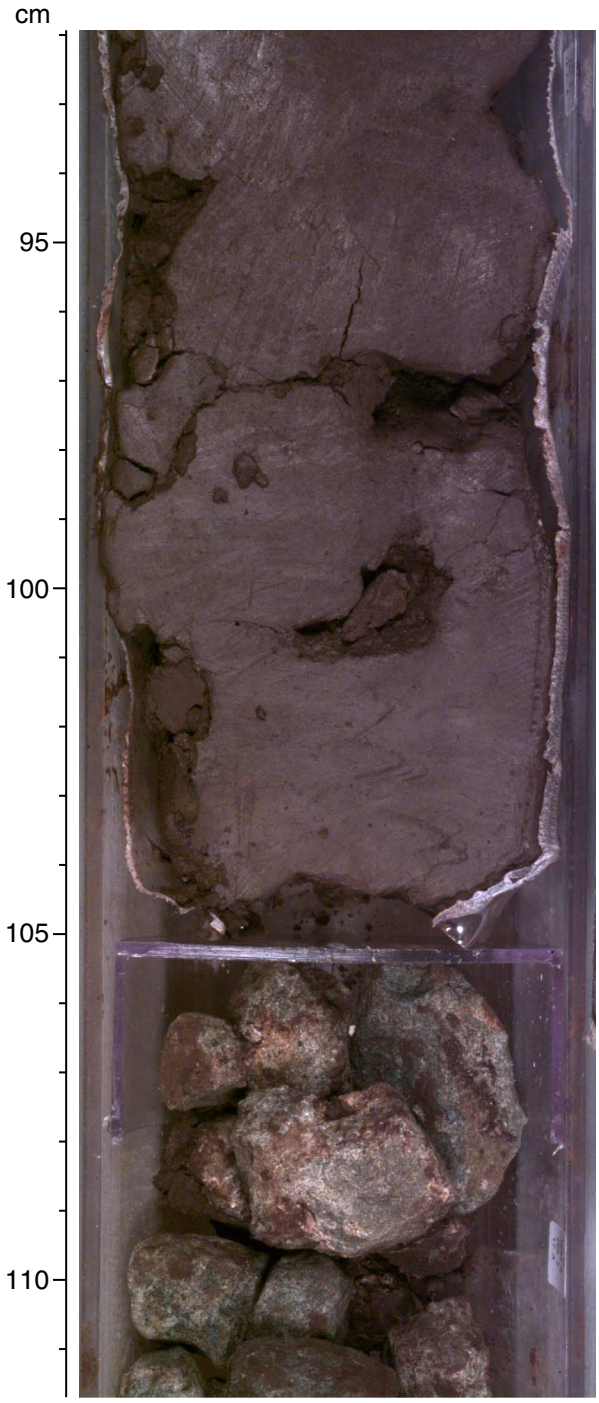

Figure F13. Examples of the characteristic internal architecture of (**A**) compound pahoehoe (Unit 20) and (**B**) simple pahoehoe lava flows (Unit 17) at Site 1205. In detail, the arrangements of lobe structures in Unit 20 are identical to those shown for Unit 17. Also shown is a inferred flow-velocity profile for an inflated pahoehoe lobe. G = lobe margins, U = upper vesicular crust, M = massive lobe interior, L= lower vesicular crust, MV = megavesicles, PV = pipe vesicles, HVS = horizontal vesicle sheets (i.e., segregation veins).

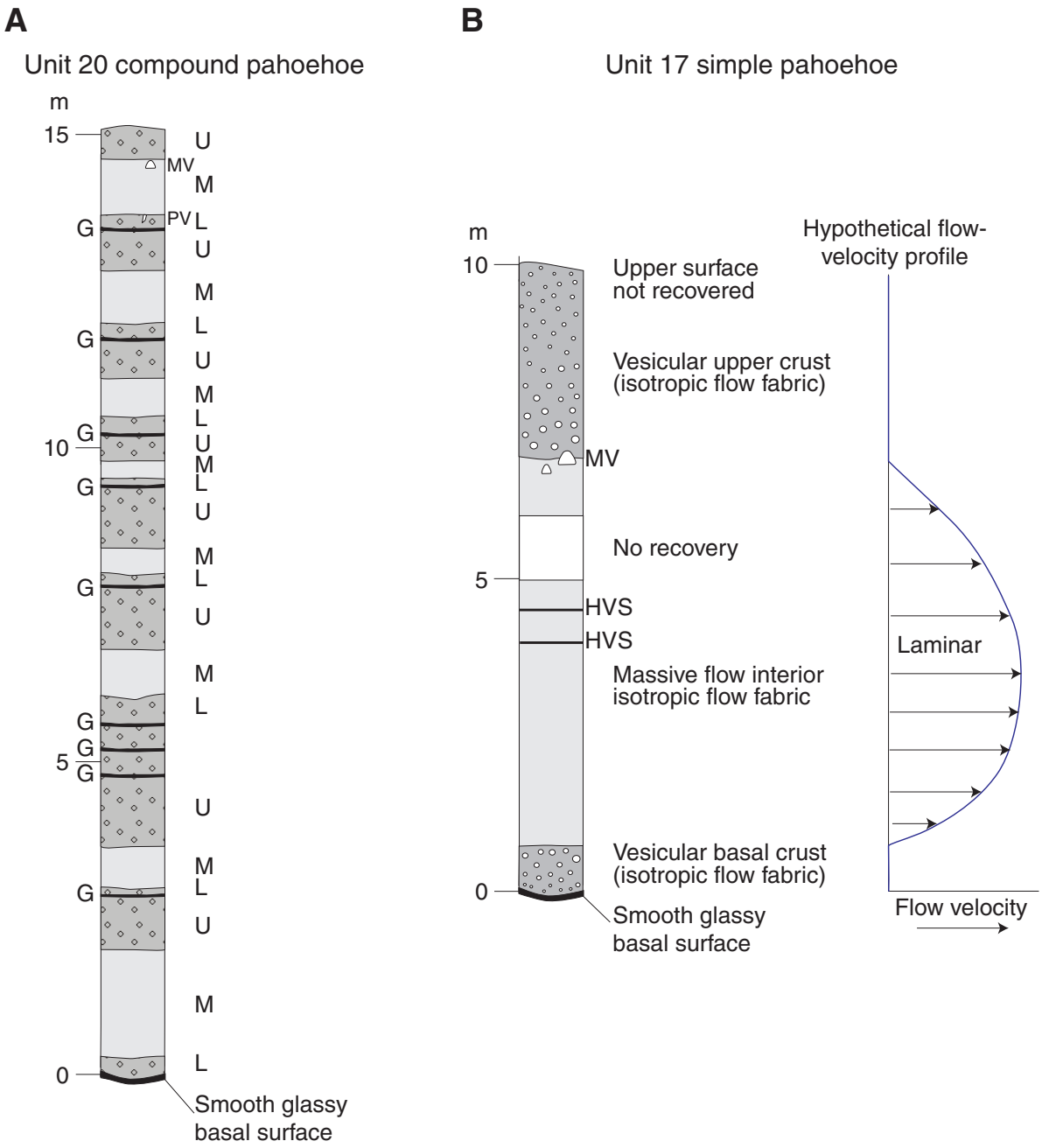

Figure F14. Example of the characteristic internal architecture and inferred flow-velocity profile of a'a lava flow (Unit 8) at Site 1205.

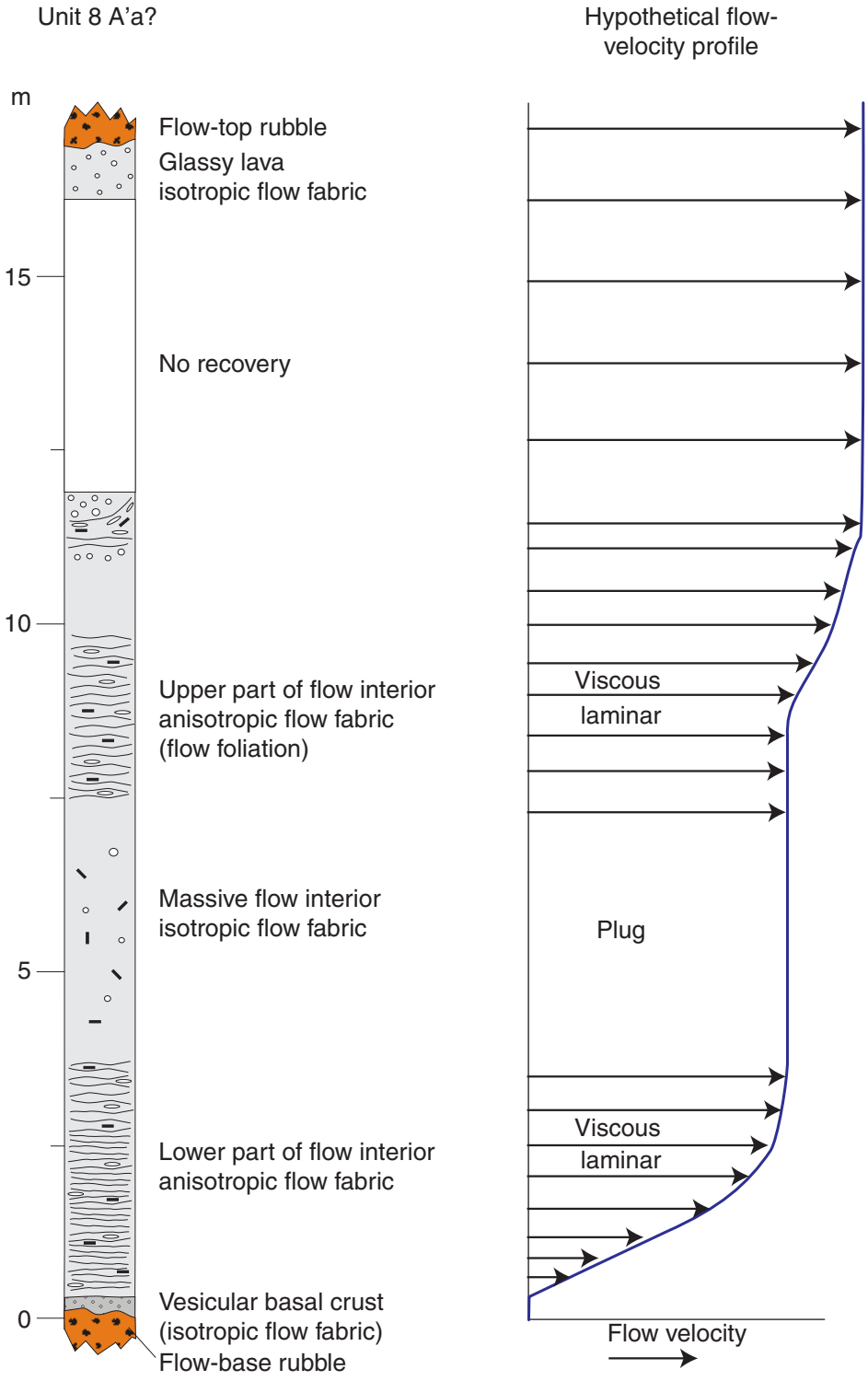

Figure F15. Examples of the characteristic internal architecture and inferred flow-velocity profiles of transitional lava types at Site 1205. **A.** Unit 3. **B.** Subunit 5b. **C.** Subunit 11b. MV = megavesicles, VC = vesicle cylinder (i.e., segregation veins).

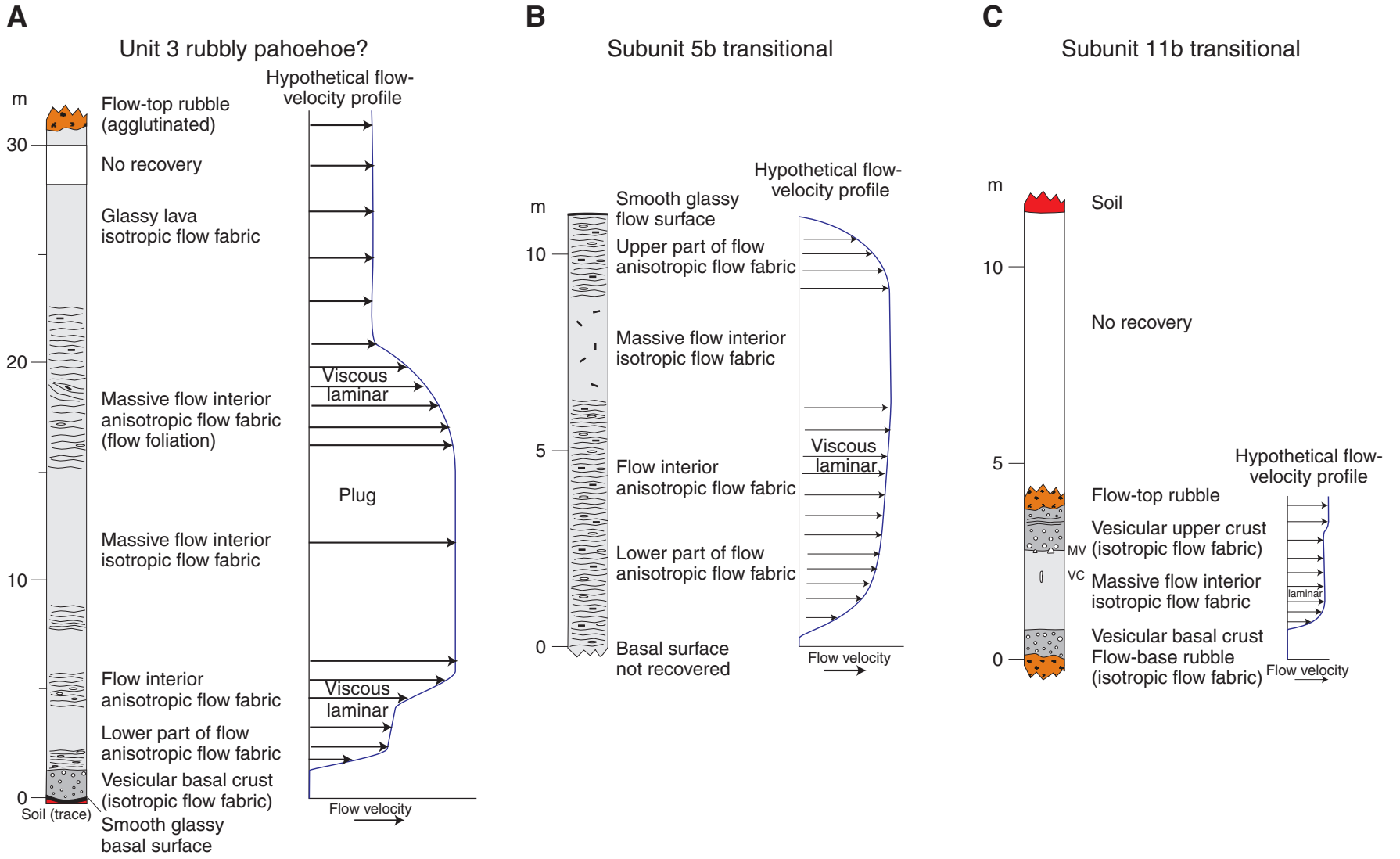

Figure F16. Photomicrographs showing plagioclase phenocrysts. **A.** Plagioclase megacryst with inclusion of olivine (Sample 197-1205A-15R-2, 138–140 cm) (cross-polarized light; field of view = 5 mm; photomicrograph 1205A-211). **B.** Rounded plagioclase phenocryst with resorption rim (Sample 197-1205A-13R-3, 27–29 cm) (cross-polarized light; field of view = 1.25 mm; photomicrograph 1205A-206). (Continued on next seven pages.)

A

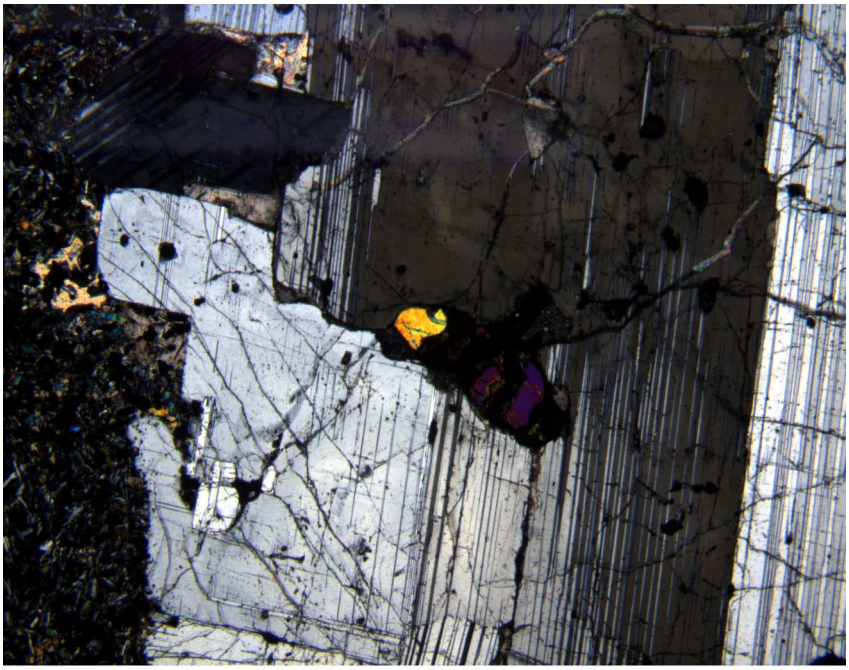

B

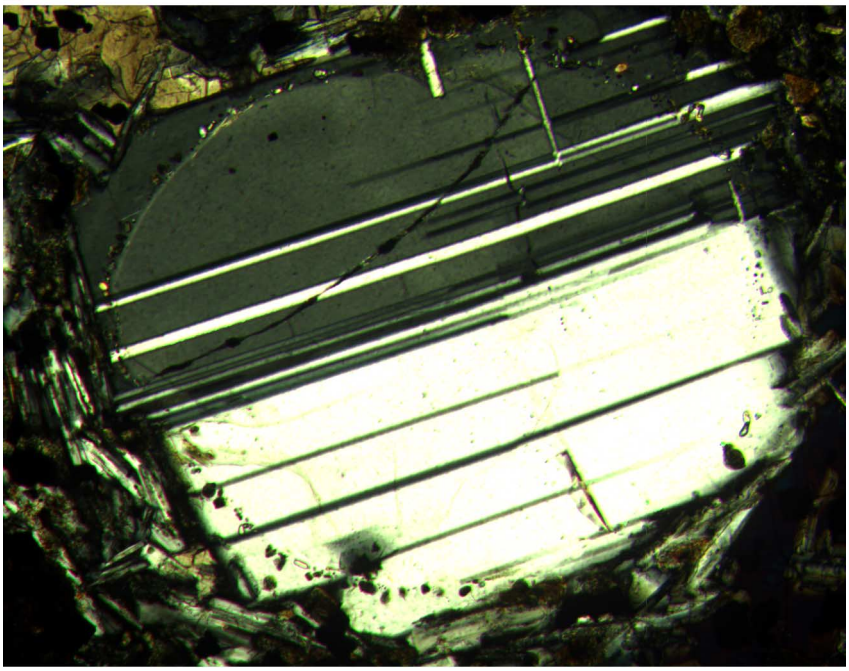

Figure F16 (continued). **C.** Compositional zonation in a plagioclase phenocryst from Subunit 8a (Sample **197-1205A-20R-5, 67–68 cm**) (cross-polarized light; field of view = 1.25 mm; photomicrograph 1205A-216). **D.** Strain lamellae in a plagioclase megacryst (Sample **197-1205A-11R-1, 73–75 cm**) (cross-polarized light; field of view = 5 mm; photomicrograph 1205A-204). (Continued on next page.)

C

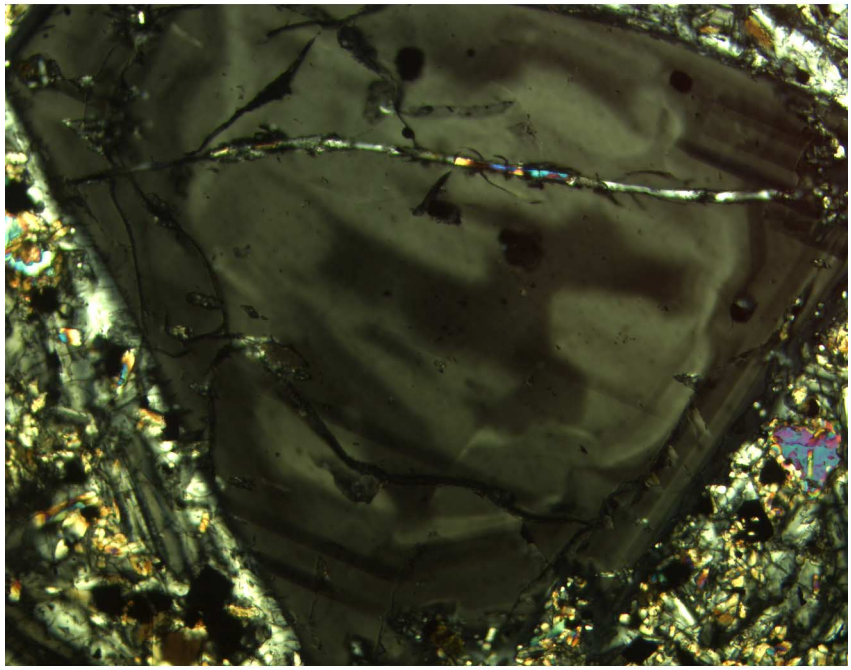

D

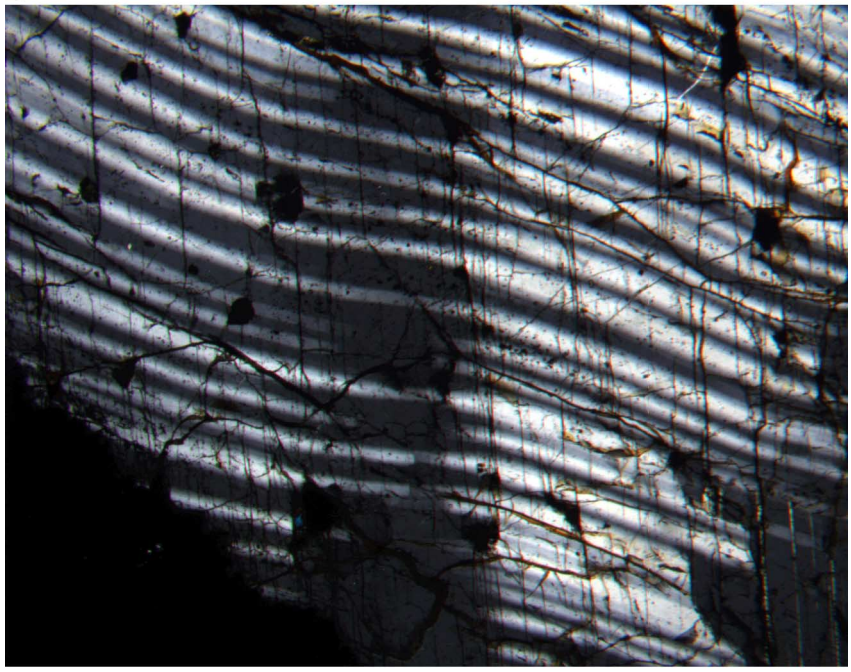

Figure F16 (continued). E, F. Plagioclase phenocrysts from Subunit 14b (Sample **197-1205A-29R-2, 55–58 cm**) (cross-polarized light; field of view = 5 mm): (E) zoned, fractured, and strained plagioclase phenocryst (photomicrograph 1205A-236); (F) highly embayed plagioclase phenocryst (photomicrograph 1205A-237). (Continued on next page.)

E

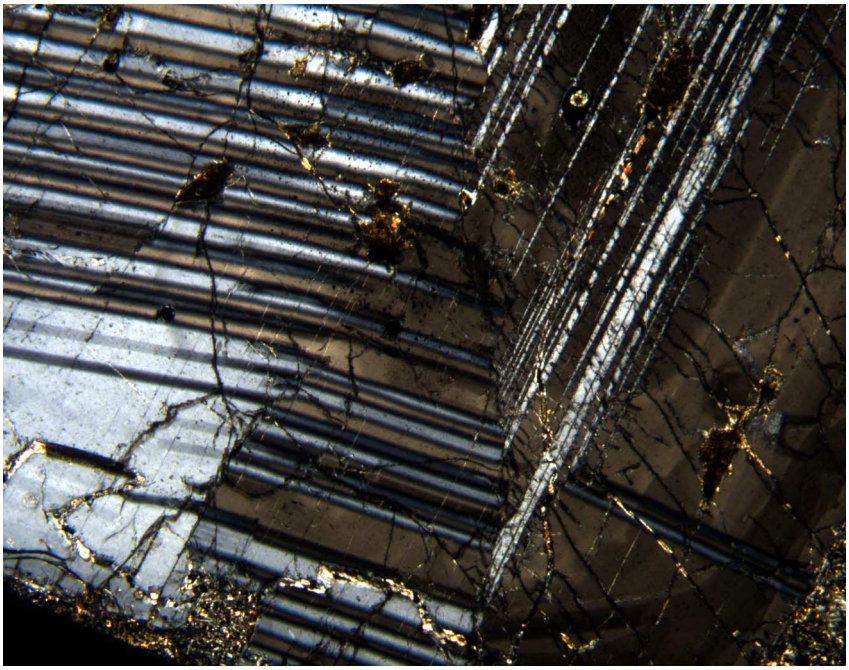

F

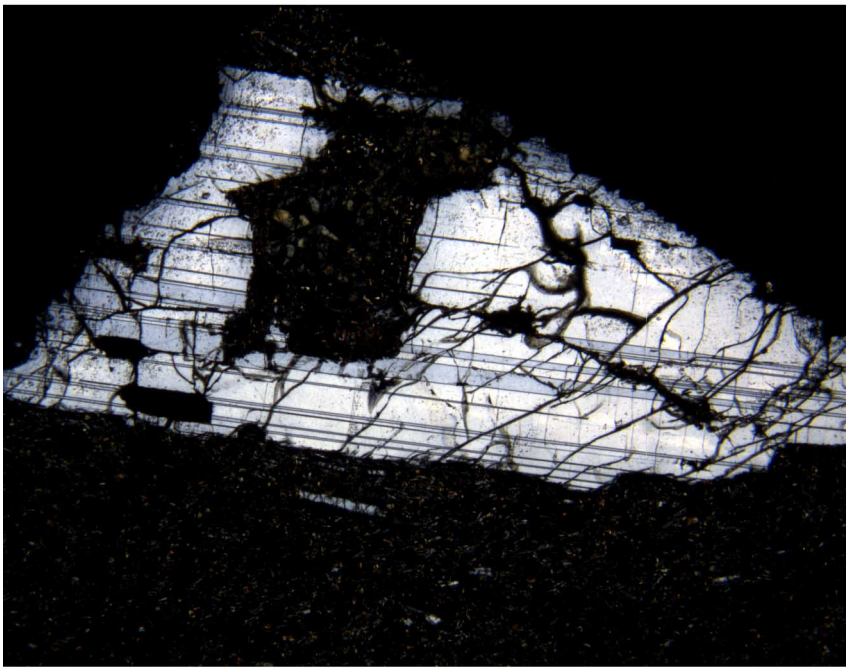

Figure F16 (continued). G. Plagioclase-olivine glomerocrysts (Sample **197-1205A-29R-2, 55–58 cm**) (cross-polarized light; field of view = 5 mm; photomicrograph 1205A-235). **H.** Highly embayed olivine phenocryst from Unit 21 (Sample **197-1205A-37R-5, 28–29 cm**) (cross-polarized light; field of view = 5 mm; photomicrograph 1205A-257). (Continued on next page.)

G

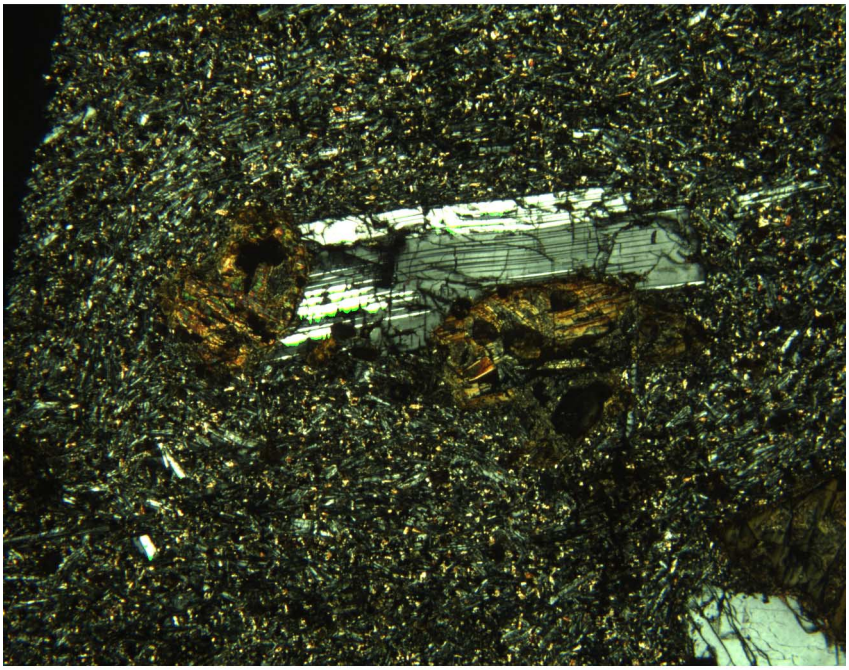

H

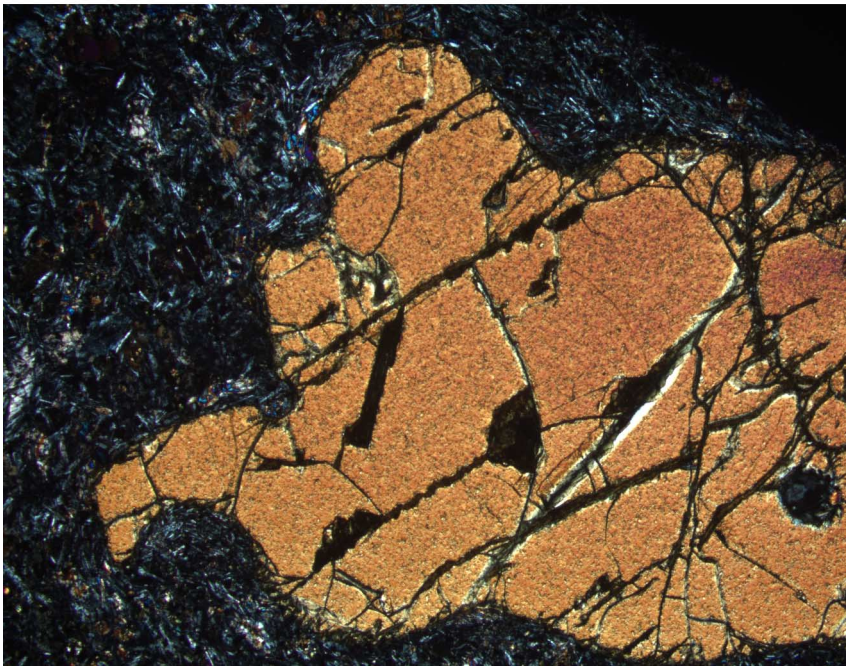

Figure F16 (continued). I. Partially altered olivine phenocrysts in Subunit 3b (Sample **197-1205A-8R-1, 59–61 cm**) (plane-polarized light; field of view = 1.25 mm; photomicrograph 1205A-190). **J.** Partially altered olivine phenocryst rimmed by biotite in Unit 27 (Sample **197-1205A-43R-2, 58–60 cm**) (plane-polarized light; field of view = 5 mm; photomicrograph 1205A-274). (Continued on next page.)

I

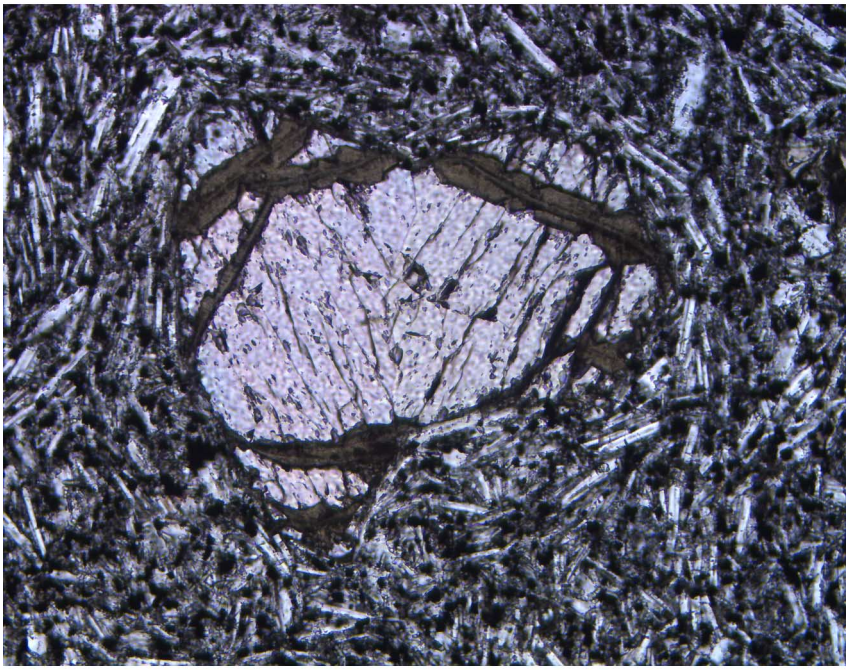

J

Figure F16 (continued). K. Glomerocryst from Subunit 5b, composed of plagioclase, pyroxene, opaque minerals, and partially altered olivine (Sample **197-1205A-16R-2, 84–86 cm**) (cross-polarized light; field of view = 5 mm; photomicrograph 1205A-214). **L.** Subophitic texture in Subunit 3b, with a large groundmass clinopyroxene crystal enclosing a partially altered olivine phenocryst (Sample **197-1205A-12R-2, 114–116 cm**) (cross-polarized light; field of view = 1.25 mm; photomicrograph 1205A-205). (Continued on next page.)

K

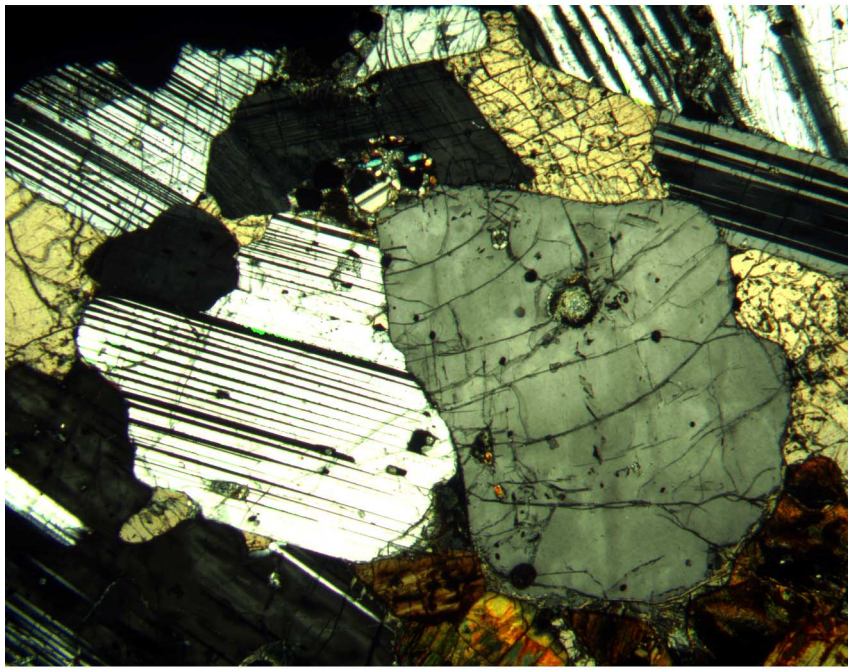

L

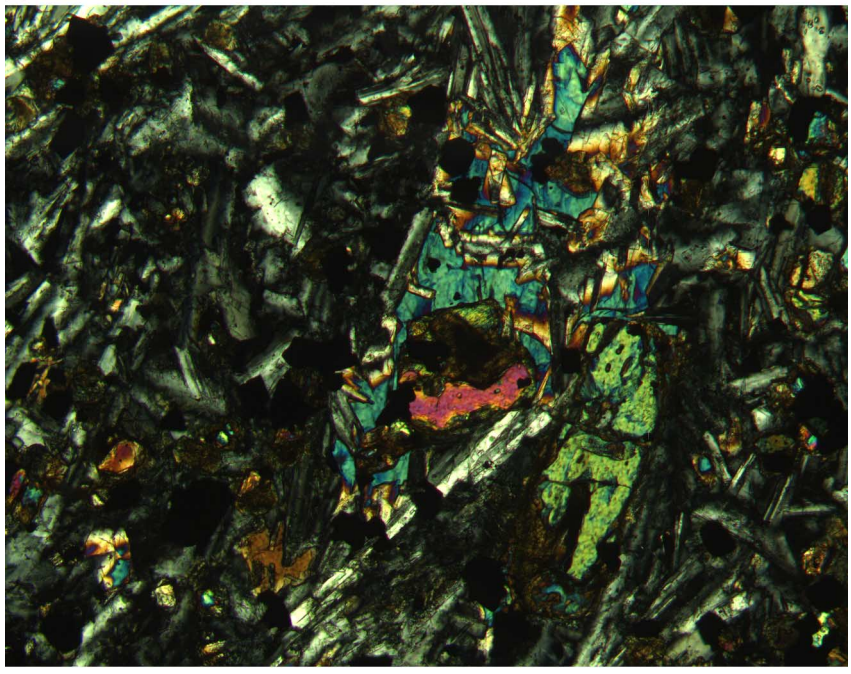

Figure F16 (continued). M. Close-up view of groundmass olivine completely altered to Fe oxyhydroxide or iddingsite (Sample **197-1205A-24R-2, 124–130 cm**) (plane-polarized light; field of view = 1.25 mm; photomicrograph 1205A-222). **N.** Strain bands in trachytic texture, Subunit 3b (Sample **197-1205A-10R-2, 73–75 cm**) (cross-polarized light; field of view = 5 mm; photomicrograph 1205A-202). (Continued on next page.)

M

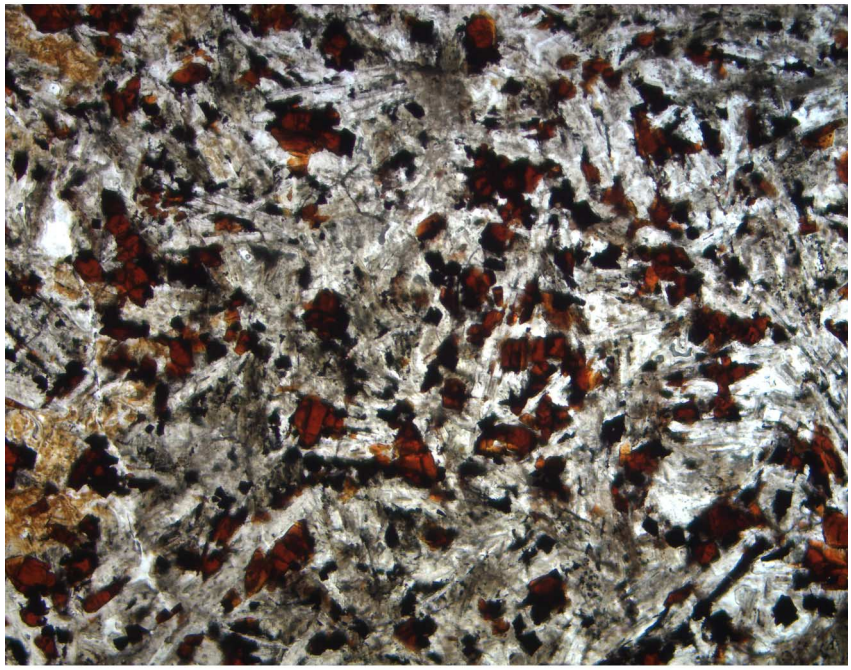

N

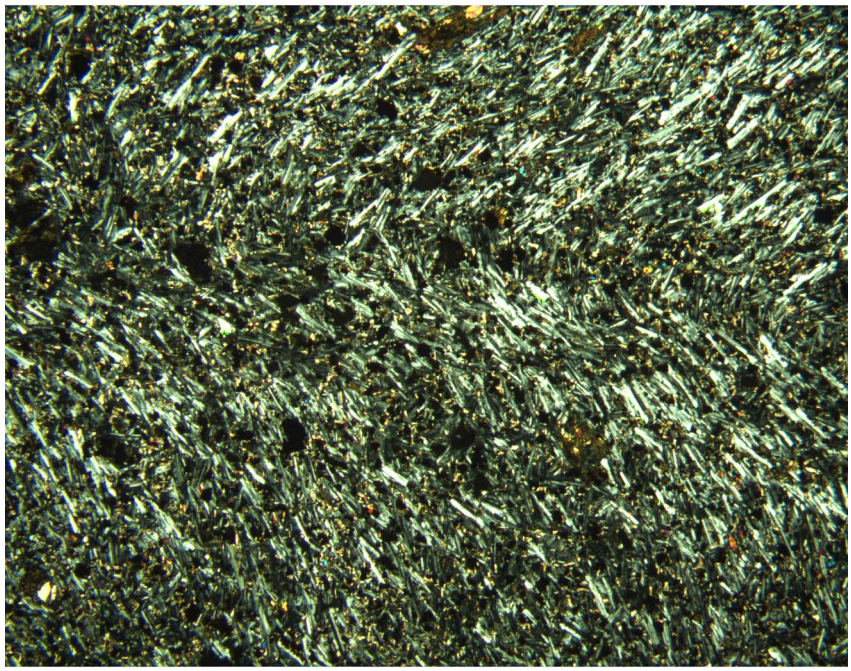

Figure F16 (continued). O. Sheared, relict olivine phenocryst in Subunit 29b (Sample **197-1205A-44R-2, 110–112 cm**) (cross-polarized light; field of view = 1.25 mm; photomicrograph 1205A-262).

O

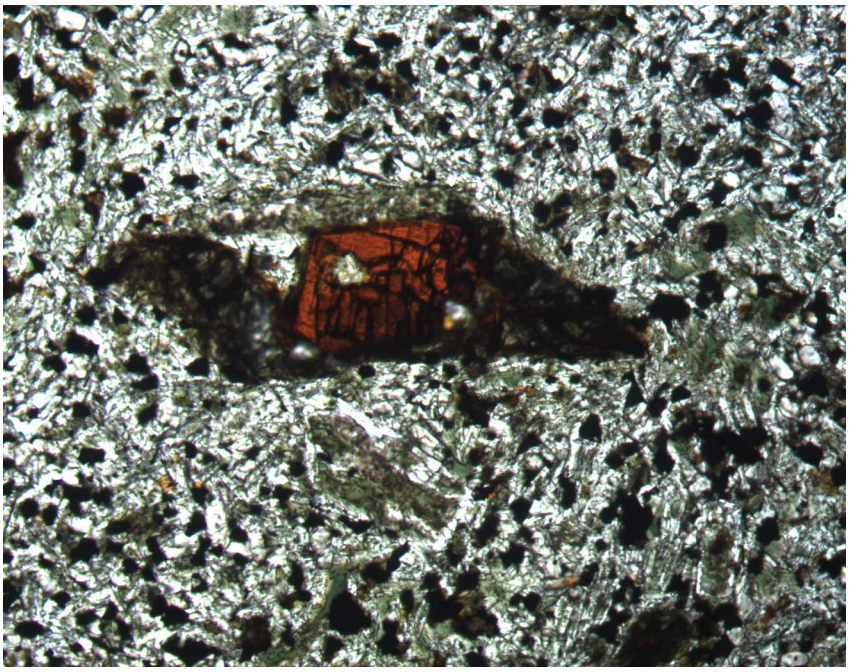

Figure F17. Photomicrographs showing titanomagnetite morphologies. **A.** Alteration of titanomagnetite to maghemite along cleavage planes and around rims in the weathered flow top of Unit 10 (Sample **197-1205A-24R-2 [Piece 19, 124–130 cm]**) (reflected light; field of view = 0.25 mm; photomicrograph 1205A-286). **B.** Alteration of titanomagnetite to maghemite in tholeiitic Subunit 19b (Sample **197-1205A-35R-4 [Piece 1C, 77–79 cm]**) (reflected light; field of view = 0.25 mm; photomicrograph 1205A-268). (Continued on next 10 pages.)

A

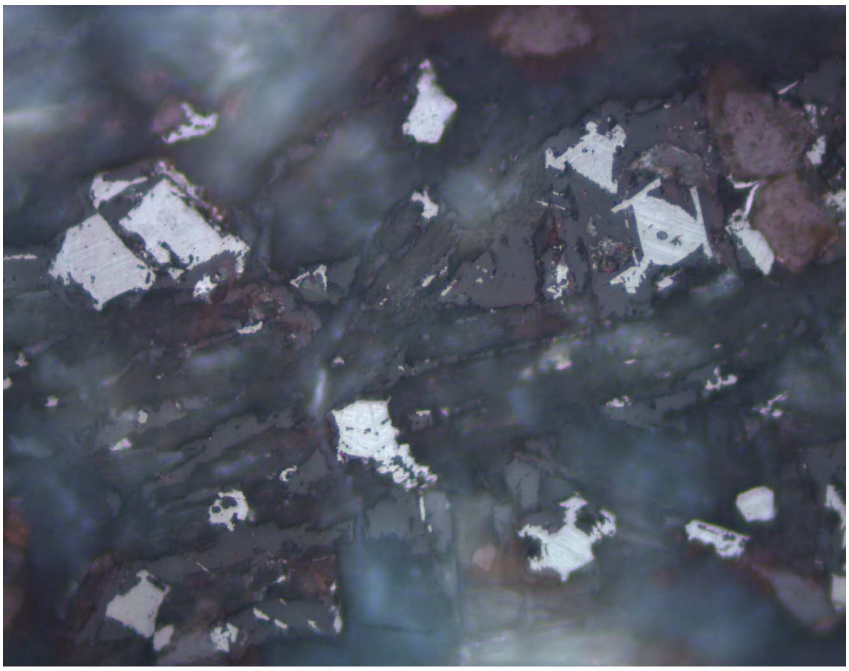

B

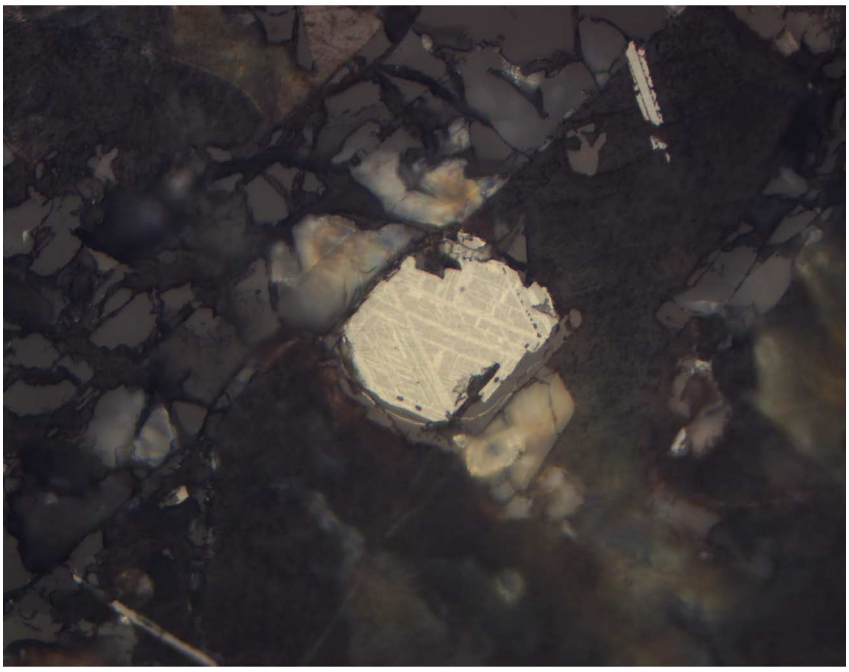

Figure F17 (continued). **C.** Alteration of titanomagnetite to maghemite in tholeiitic Subunit 19b (Sample 197-1205A-35R-4 [Piece 1C, 77–79 cm]) (reflected light; field of view = 0.25 mm; photomicrograph 1205A-280). **D.** Typical titanomagnetite morphologies in the alkali basalt from Unit 20 (Sample 197-1205A-36R-5 [Piece 2D, 50–51 cm]) (reflected light; field of view = 1.25 mm; photomicrograph 1205A-283). (Continued on next page.)

C

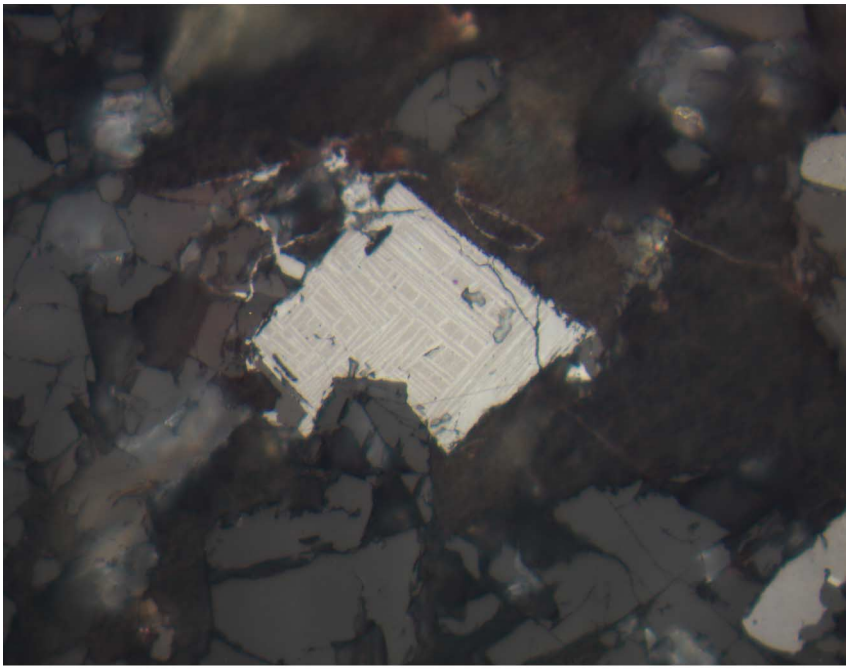

D

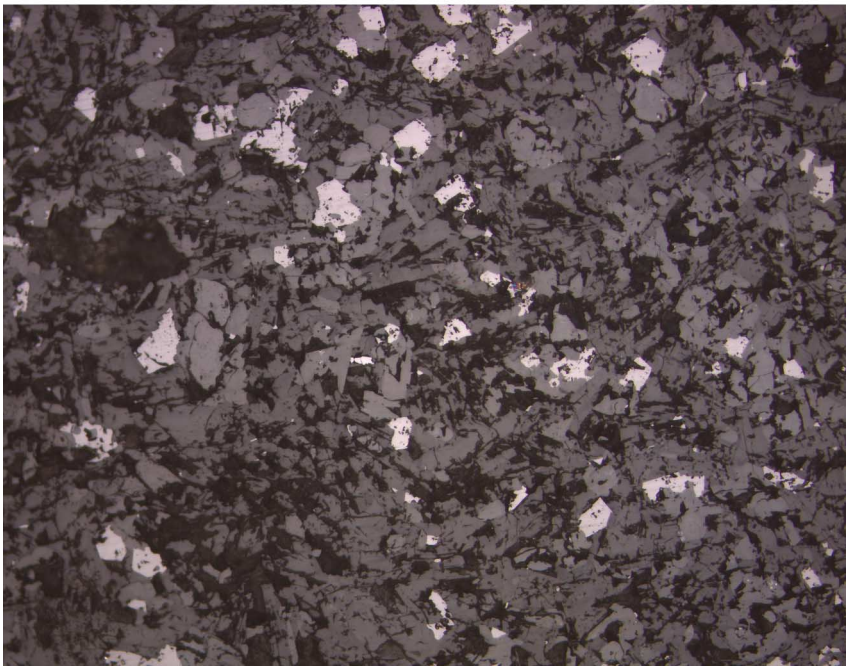

Figure F17 (continued). E, F. Typical titanomagnetite morphologies in the alkali basalt (reflected light; field of view = 1.25 mm) (E) Unit 20 (Sample **197-1205A-44R-1 [Piece 5A, 87–88 cm]**) (photomicrograph 1205A-284); (F) Subunit 19b (Sample **197-1205A-35R-4 [Piece 1C, 77–79 cm]**) (photomicrograph 1205A-281). (Continued on next page.)

E

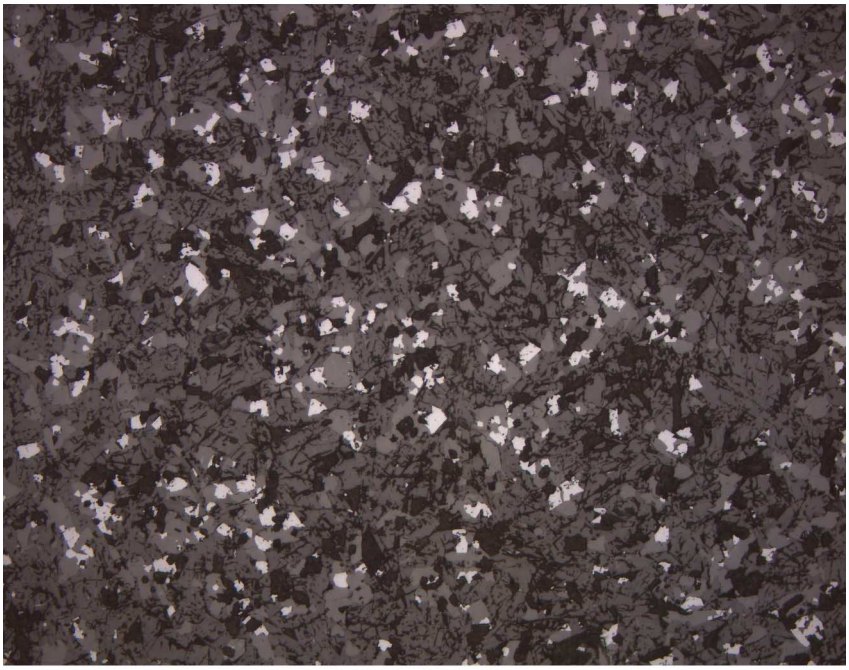

F

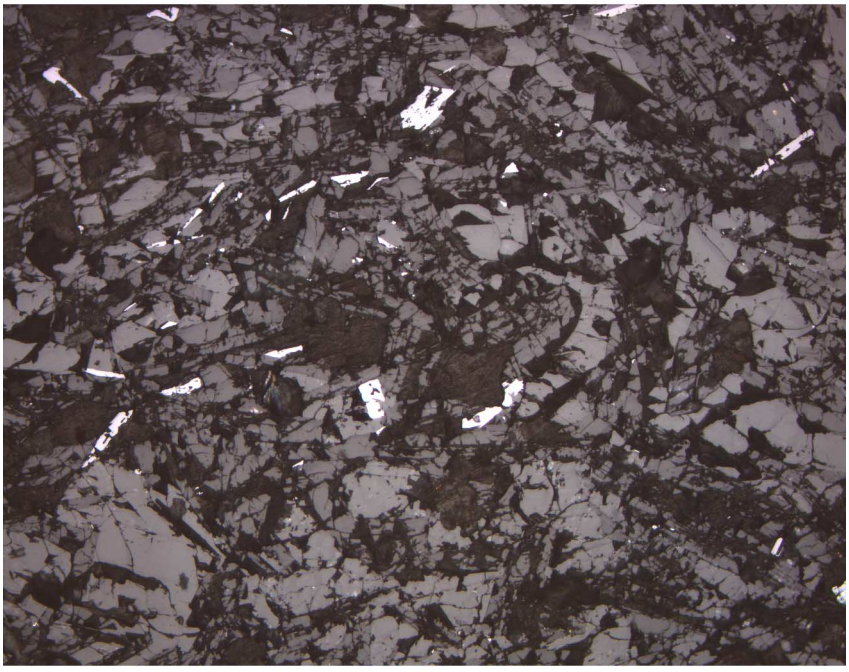

Figure F17 (continued). G. Typical titanomagnetite morphologies in the alkali basalt of Subunit 19b (Sample **197-1205A-35R-4 [Piece 1C, 77–79 cm]**) (reflected light; field of view = 1.25 mm; photomicrograph 1205A-282). **H.** Lithologic Unit V conglomerate immediately above basement. Development of goethite in a hawaiite cobble; note that titanomagnetite is relatively unaltered (Sample **197-1205A-5R-2 [Piece 21, 101–103 cm]**) (reflected light; field of view = 0.25 mm; photomicrograph 1205A-182). (Continued on next page.)

G

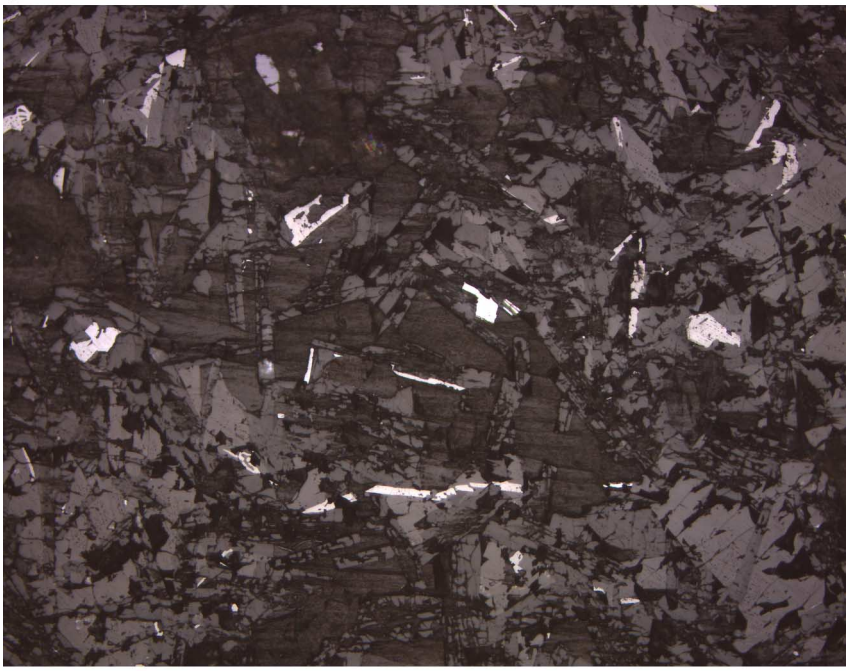

H

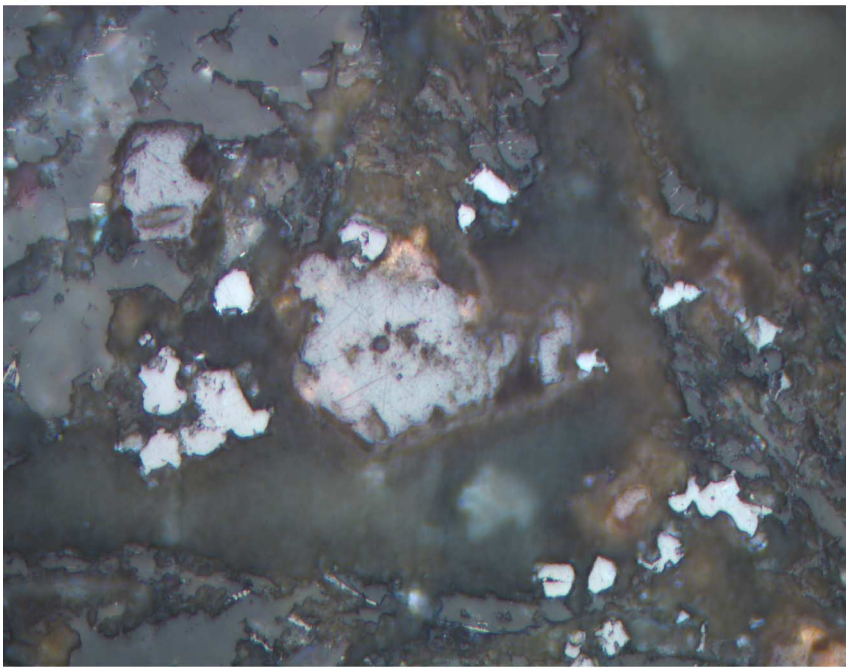

Figure F17 (continued). I. Lithologic Unit V conglomerate immediately above basement. Distinctive morphology of groundmass titanomagnetite in the hawaiite cobbles; such dendritic forms are present in distinct zones that may be parallel or transverse to the plagioclase laths that define the trachytic texture (Sample **197-1205A-5R-2 [Piece 21, 101–103 cm]**) (reflected light; field of view = 0.25 mm; photomicrograph 1205A-287). **J.** Bireflectance of ilmenite and highlighting the development of ilmenite oxidation lamellae in titanomagnetite from Subunit 3b. Ilmenite oxidation lamellae are illuminated (Sample **197-1205A-13R-3, 27–29 cm**) (reflected light; field of view = 0.25 mm; photomicrograph 1205A-226). (Continued on next page.)

I

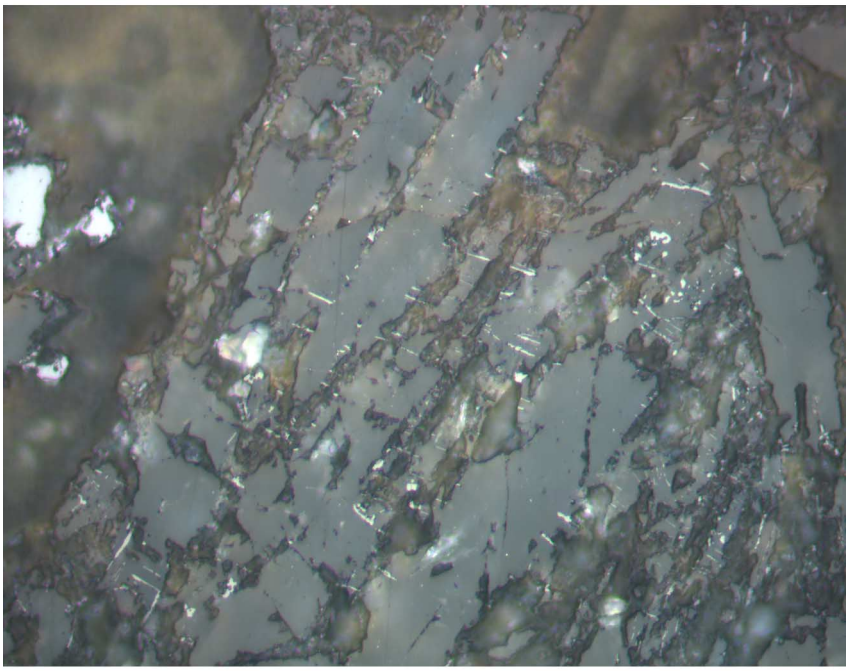

J

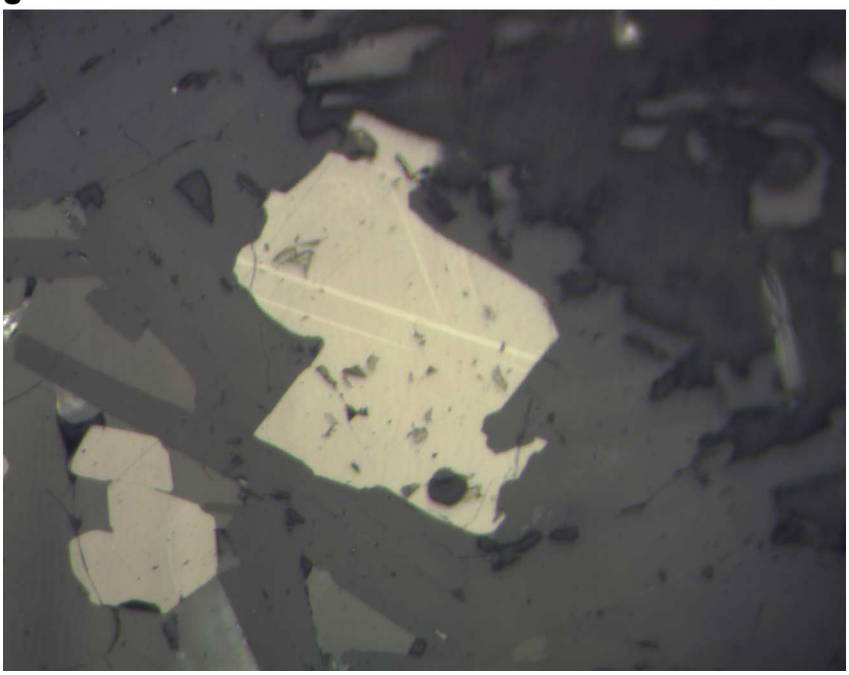

Figure F17 (continued). K. Bireflectance of ilmenite and highlighting the development of ilmenite oxidation lamellae in titanomagnetite from Subunit 3b. After rotating the stage 90°, the ilmenite oxidation lamellae are not illuminated (Sample **197-1205A-13R-3, 27–29 cm**) (reflected light; field of view = 0.25 mm; photomicrograph 1205A-227). **L.** Ilmenite oxidation not restricted to lamellae in Unit 27. Ilmenite is illuminated (Sample **197-1205A-43R-2 [Piece 2A, 58–60 cm]**) (reflected light; field of view = 0.25 mm; photomicrograph 1205A-252). (Continued on next page.)

K

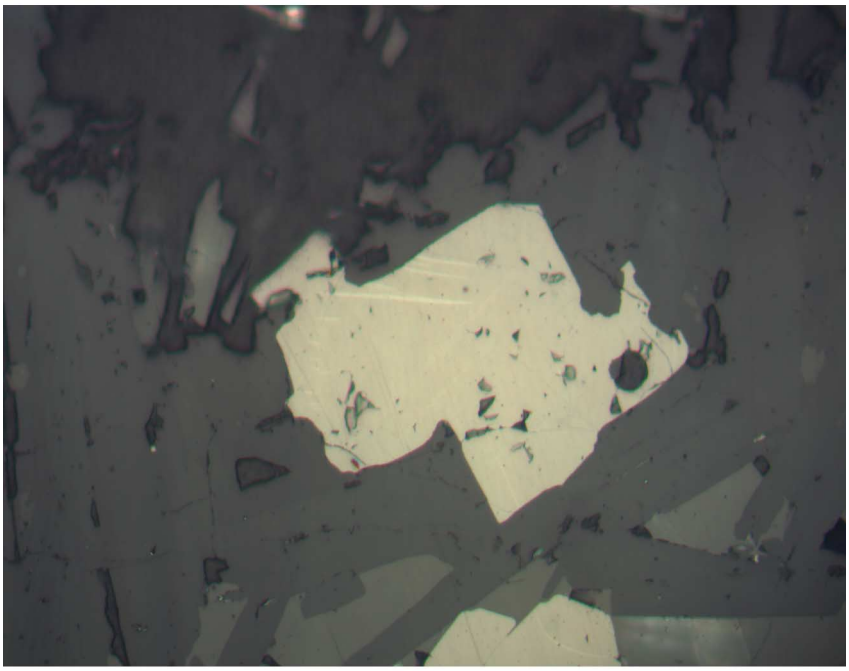

L

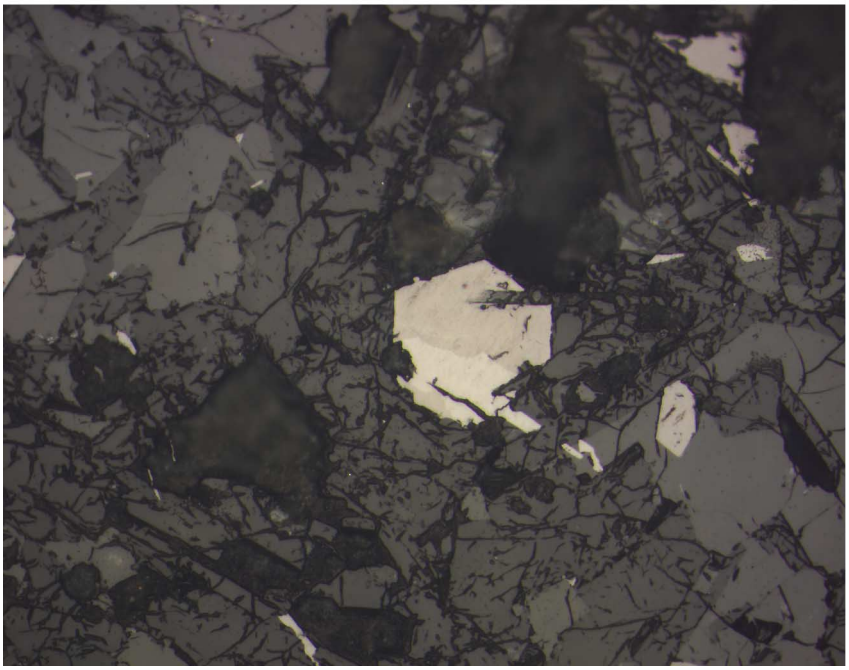

Figure F17 (continued). M. Ilmenite oxidation not restricted to lamellae in Unit 27. After rotating the stage 90°, ilmenite is not illuminated (Sample **197-1205A-43R-2 [Piece 2A, 58–60 cm]**) (reflected light; field of view = 0.25 mm; photomicrograph 1205A-253). **N.** Early stages of maghemite (bright blue-gray) replacement of titanomagnetite (dull pink-gray) in the Site 1205 basement lava units: maghemite development along titanomagnetite cleavage planes in Subunit 12b (Sample **197-1205A-27R-5 [Piece 5, 103–105 cm]**) (reflected light; field of view = 0.25 mm; photomicrograph 1205A-224). (Continued on next page.)

M

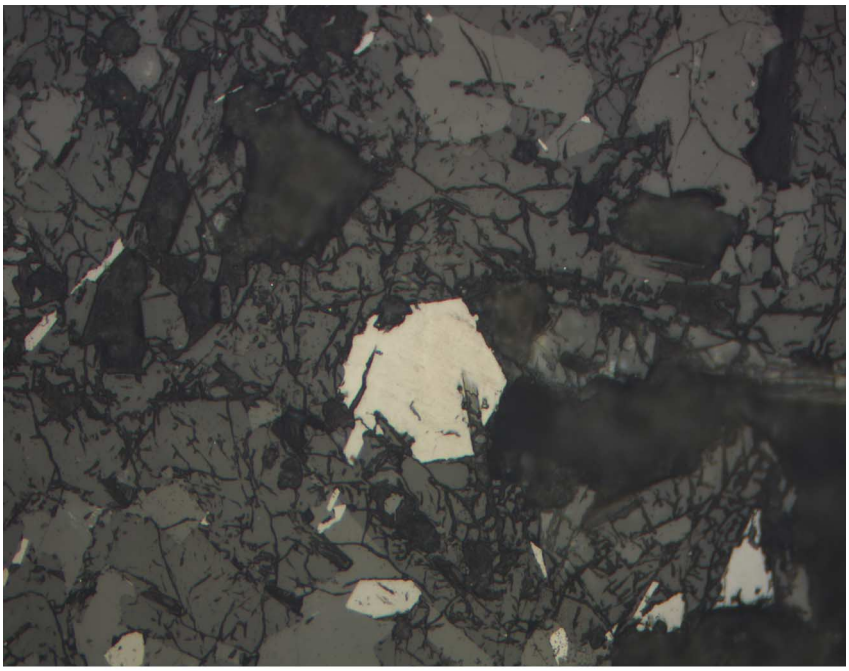

N

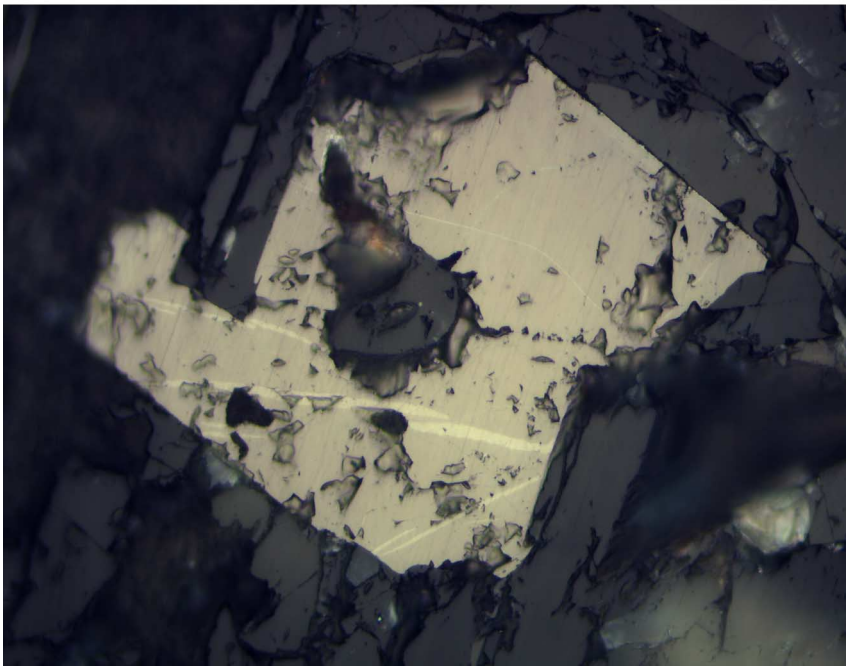

Figure F17 (continued). O, P. Early stages of maghemite (bright blue-gray) replacement of titanomagnetite (dull pink-gray) in the Site 1205 basement lava units (reflected light; field of view = 0.25 mm): (O) maghemite development around the rim of and along a fracture in titanomagnetite in Subunit 26a; ilmenite oxidation lamellae are also evident (Sample **197-1205A-41R-5 [Piece 1A, 24–26 cm]**) (photomicrograph 1205A-267). (P) maghemite development along titanomagnetite cleavage planes in Unit 27; one titanomagnetite crystal is unaltered (Sample **197-1205A-43R-2, 58–60 cm**) (photomicrograph 1205A-254). (Continued on next page.)

O

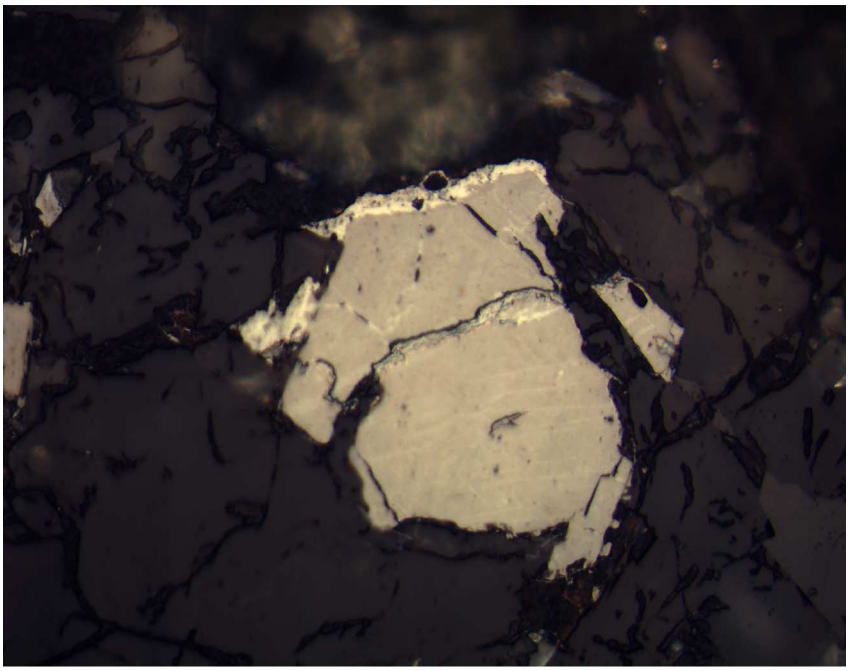

P

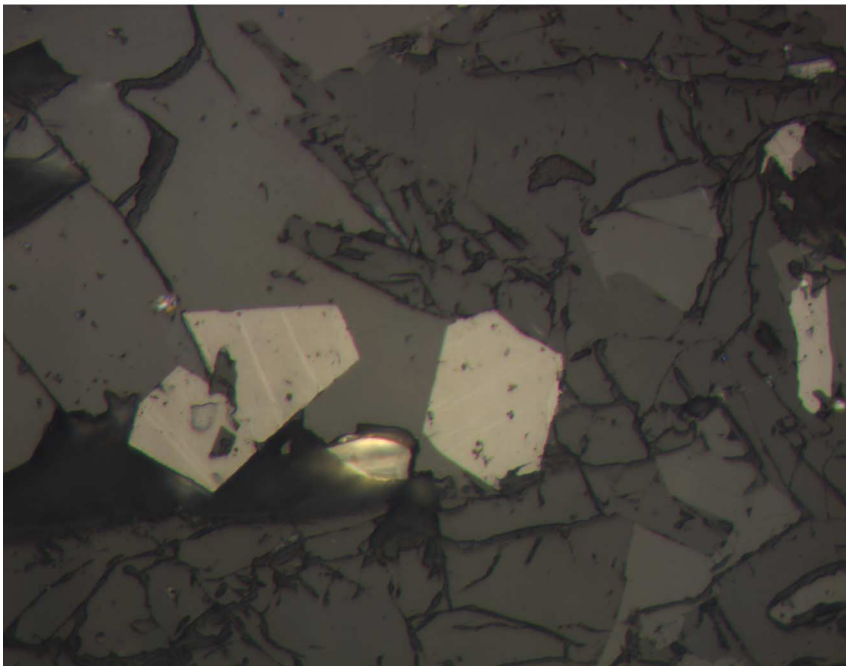

Figure F17 (continued). Q. Early stages of maghemite (bright blue-gray) replacement of titanomagnetite (dull pink-gray) in the Site 1205 basement lava units: maghemite development along titanomagnetite cleavage planes and fractures in Subunit 30b; note that several crystals are unaltered (Sample **197-1205A-45R-1, 126–128 cm**) (reflected light; field of view = 0.25 mm; photomicrograph 1205A-265). **R.** Titanomagnetite inclusions in olivine from alkali basalt compared with groundmass titanomagnetite: two inclusions (arrows) in an olivine phenocryst in Subunit 3b (Sample **197-1205A-8R-1 [Piece 4, 59–61 cm]**) (reflected light; field of view = 0.25 mm; photomicrograph 1205A-192). (Continued on next page.)

Q

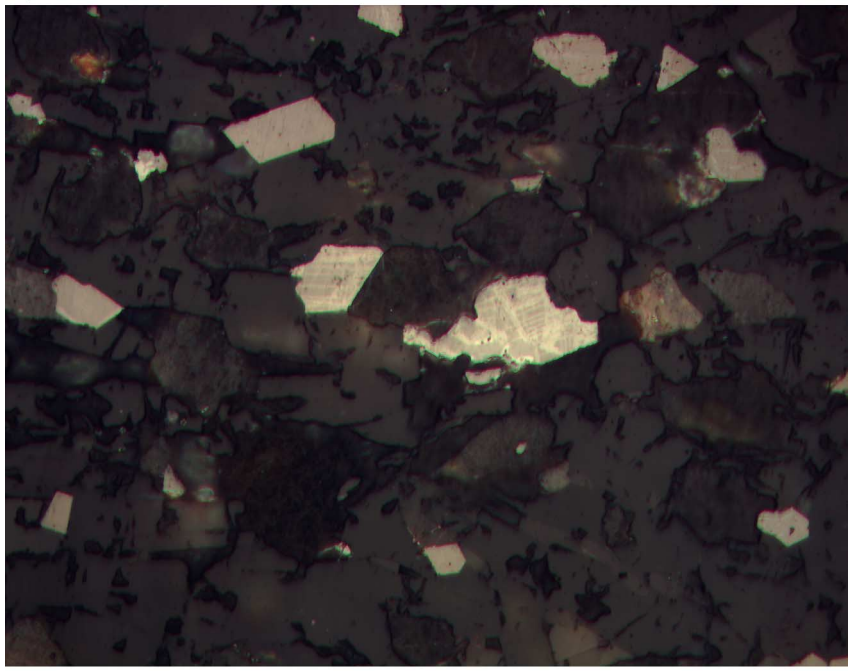

R

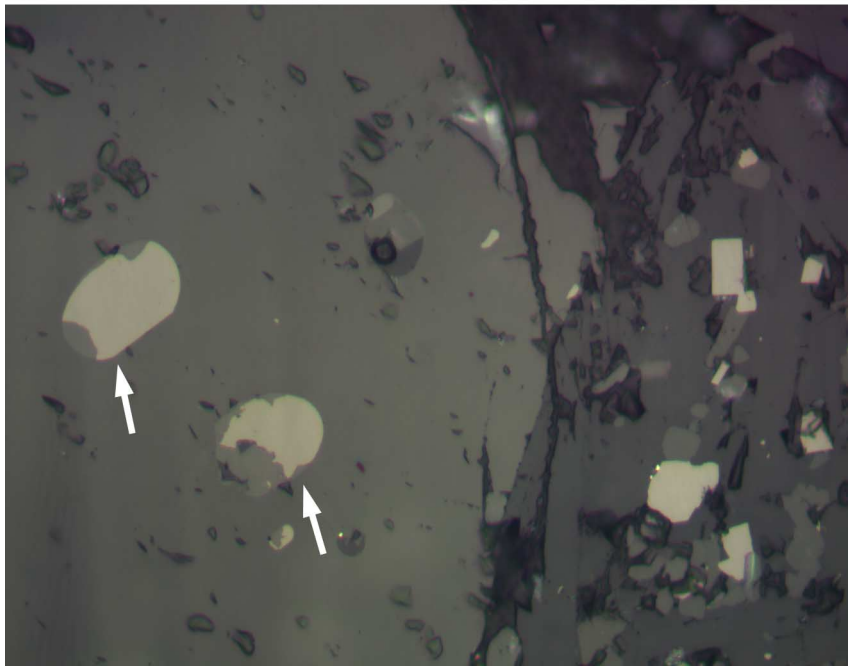

Figure F17 (continued). S. Titanomagnetite inclusions in olivine from alkali basalt compared with groundmass titanomagnetite: four small inclusions (arrows) in a groundmass olivine crystal from Unit 20; note that the groundmass titanomagnetite exhibits extensive development of ilmenite oxidation lamellae (Sample **197-1205A-36R-5 [Piece 2D, 50–51 cm]**) (reflected light; field of view = 0.25 mm; photomicrograph 1205A-250). **T.** Opaque inclusions in olivine phenocrysts from tholeiitic basalt Subunit 19b. Olivine is completely altered and two Cr spinel inclusions have been completely replaced by titanomagnetite (pink-gray). One unaltered Cr spinel inclusion remains (dull blue-gray) (Sample **197-1205A-35R-4 [Piece 1C, 77–79 cm]**) (reflected light; field of view = 0.25 mm; photomicrograph 1205-288). (Continued on next page.)

S

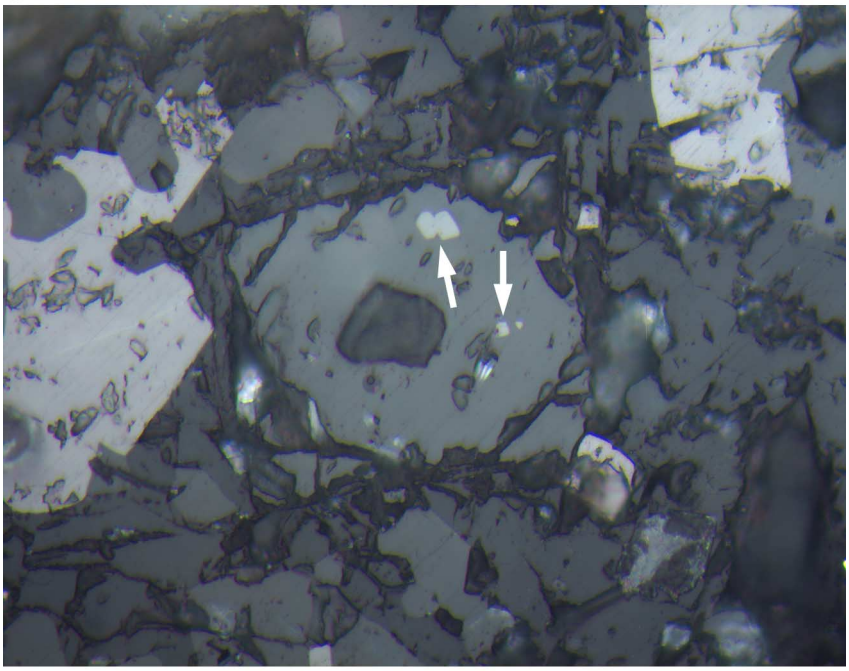

T

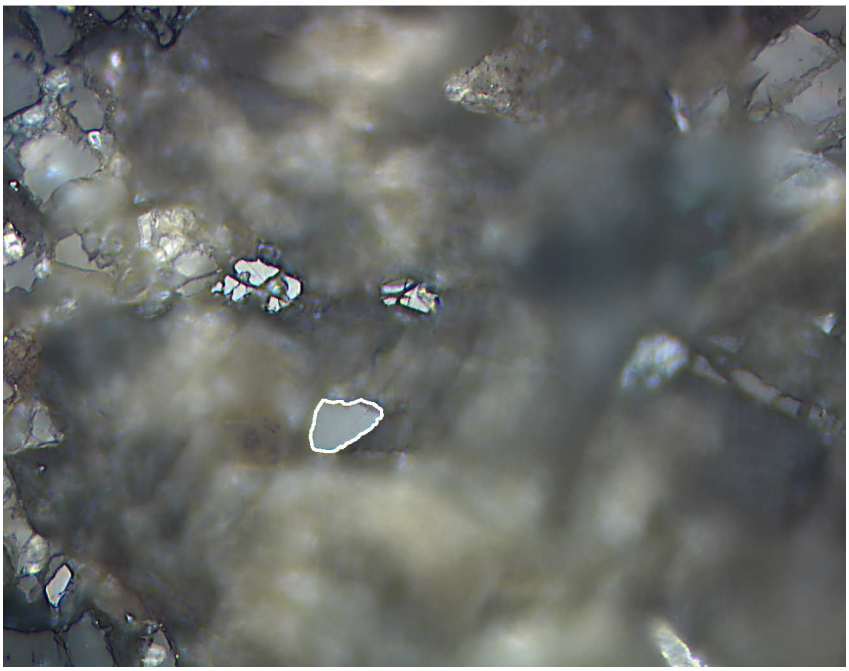

Figure F17 (continued). U, V. Cr spinel in tholeiitic basalt Subunit 19b with rims of titanomagnetite after reacting with the magma (Sample **197-1205A-35R-4 [Piece 1C, 77–79 cm]**) (reflected light; field of view = 0.25 mm): (U) photomicrograph 1205A-248; (V) photomicrograph 1205A-270.

U

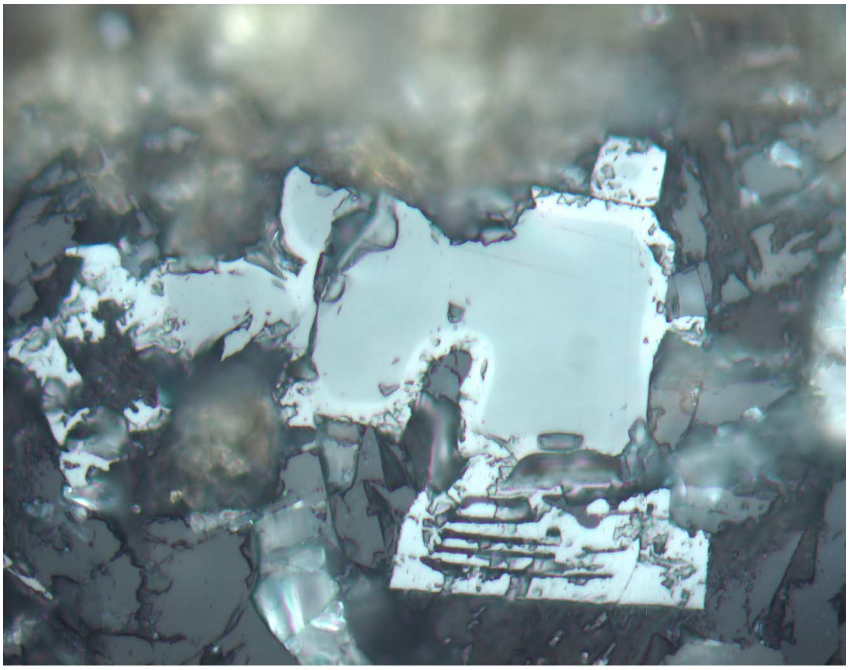

V

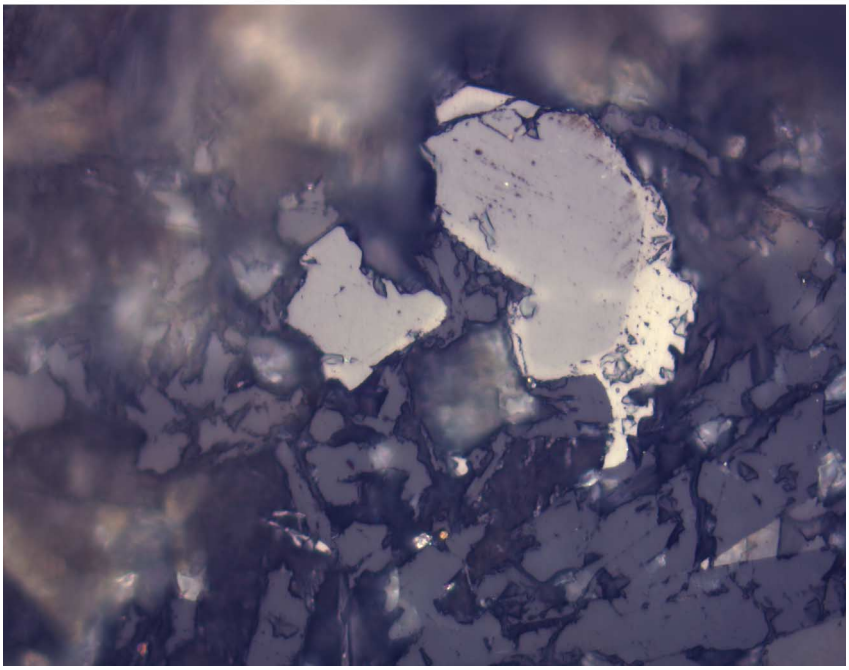

Figure F18. Total alkali content ($Na_2O + K_2O$) vs. SiO_2 classification plot for lava flows from Nintoku Seamount. The solid diagonal line is the alkalic-tholeiitic dividing line for Hawaiian basalt (Macdonald and Katsura, 1964). Only two lava units (Subunits 18b and 19b) at Site 1205 are composed of tholeiitic basalt. All other flow units at Site 1205 and nearby DSDP Site 432 (data from Kirkpatrick et al., 1980; M. Regelous et al., unpubl. data) are alkalic basalt. At both sites, conglomerates overlying igneous basement contain hawaiite clasts, which are distinguished by their high total alkali (>6 wt%) and relatively high SiO_2 content. Shown for comparison are data for Suiko Seamount (Site 433), which is dominantly tholeiitic basalt (Kirkpatrick et al., 1980; M. Regelous et al., unpubl. data).

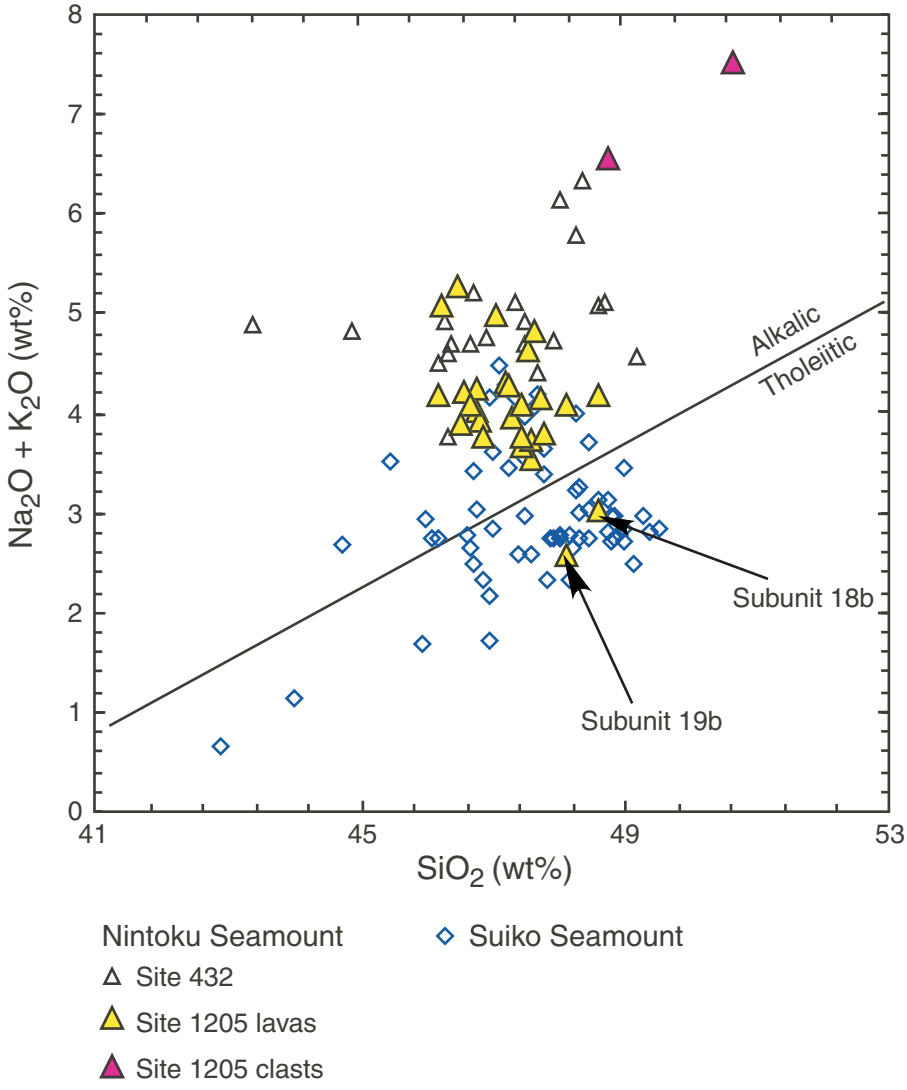

Figure F19. Abundances of Na_2O, K_2O, TiO_2, CaO, Al_2O_3, and Zr vs. MgO content for lavas from Sites 1205 and 432 at Nintoku Seamount. All trends show an inverse correlation except CaO at <5 wt% MgO. Shown for comparison are data for Suiko Seamount (Kirkpatrick et al., 1980; M. Regelous et al., unpubl. data).

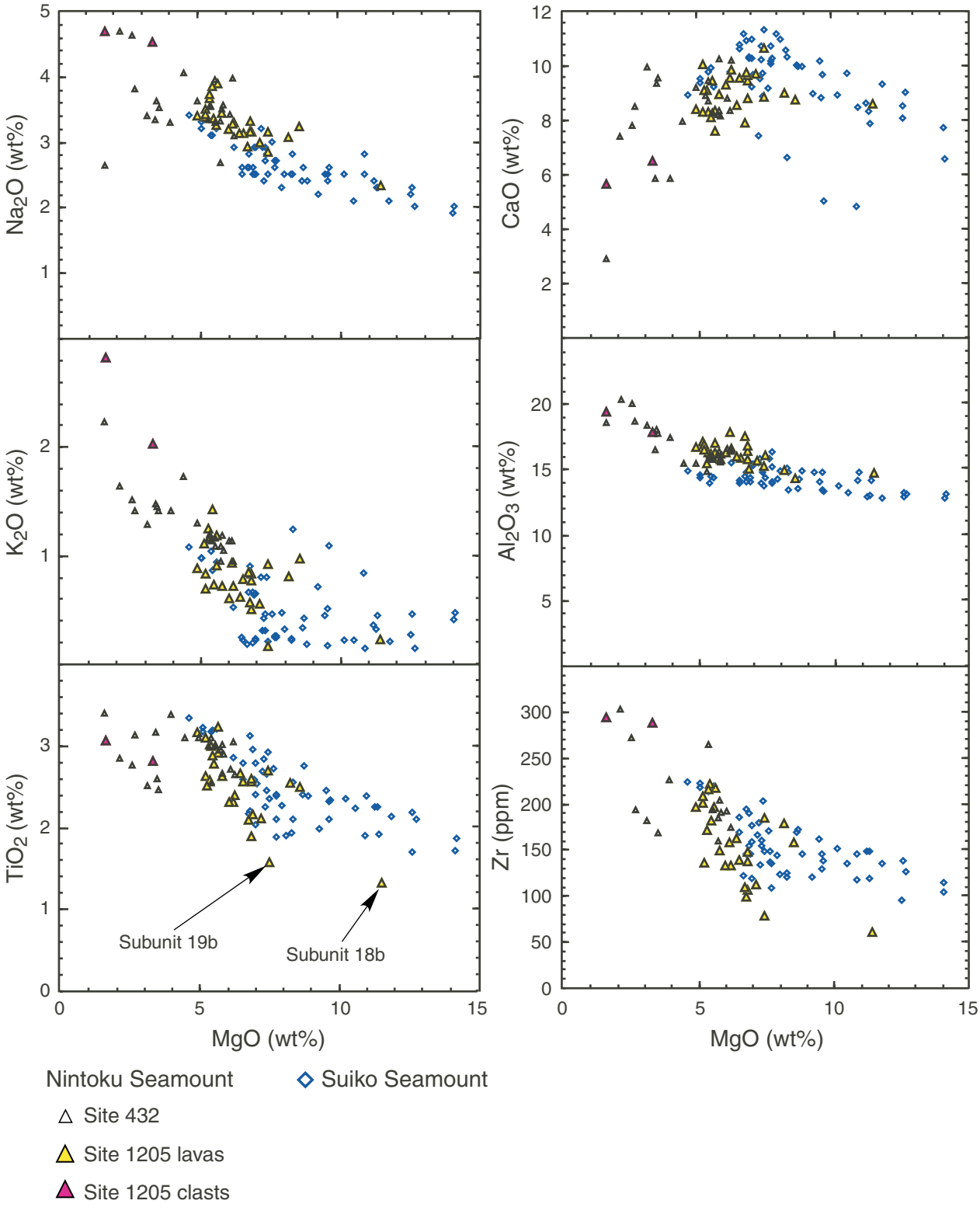

Figure F20. Alkalinity, Ti/Zr, Zr, and Ba abundance vs. depth. Alkalinity is a measure of the deviation of the sample from the alkalic-tholeiitic dividing line in Figure F18, p. 67; tholeiitic lavas have negative values. From ~40 to 250 mbsf, alkalinity decreases, the abundance of Zr and Ba decreases, and Ti/Zr increases, with the tholeiitic basalt in Subunits 18b and 19b defining the extreme values. Below Subunit 19b all flow units are composed of alkali basalt.

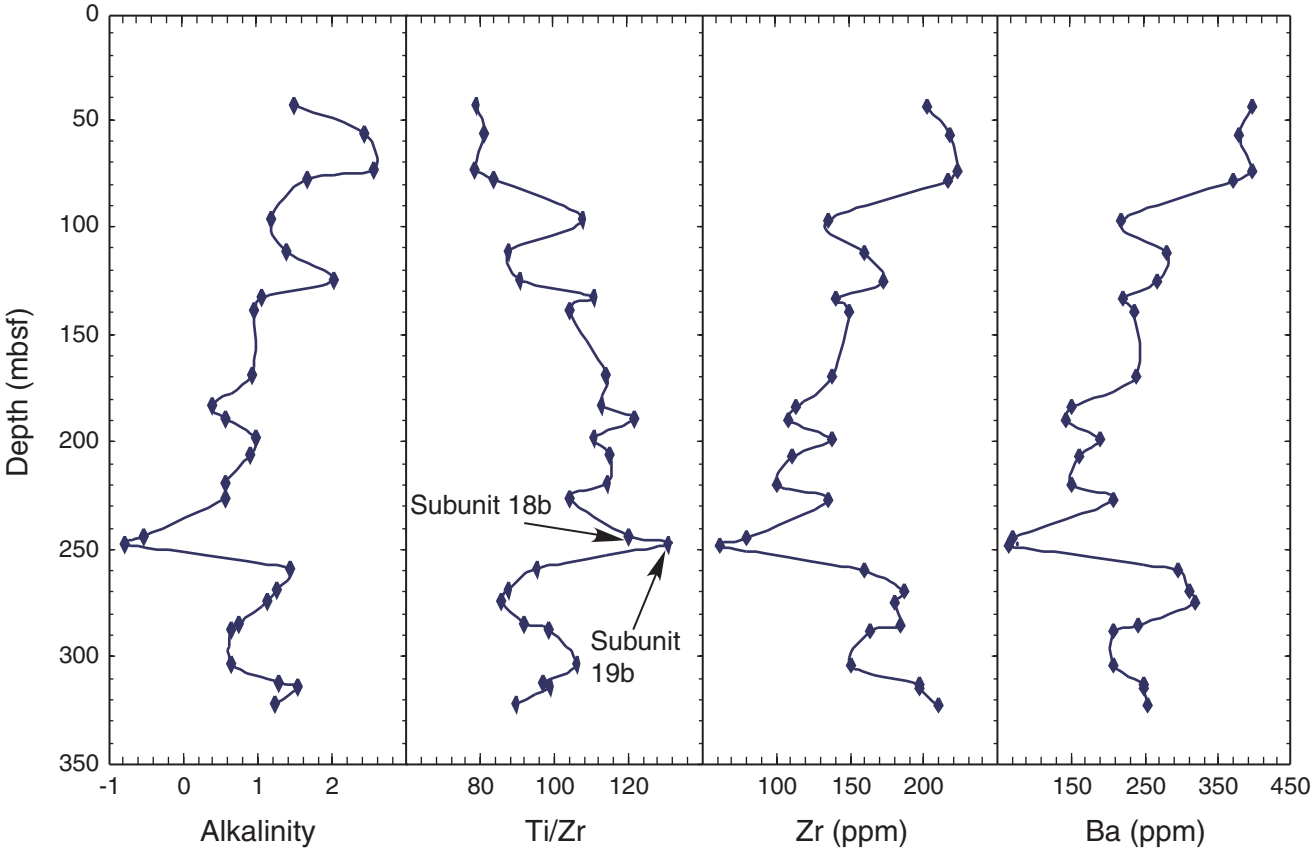

Figure F21. Abundance of Sc vs. MgO comparing data for Sites 1205 and 432 at Nintoku Seamount with data for Suiko Seamount (Kirkpatrick et al., 1980; M. Regelous et al., unpubl. data), Mauna Kea Volcano (Yang et al., 1996; S. Huang and F.A. Frey, unpubl. data), and mid-ocean-ridge basalt (MORB) from the East Pacific Rise (data from J.M. Sinton, pers. comm., 1998). Important observations are the lower Sc content of Hawaiian basalt relative to East Pacific Rise MORB and the decrease in Sc content with decreasing MgO at <5 wt% MgO for Nintoku lavas. Sc is a compatible element in garnet and clinopyroxene. Consequently, the difference in Sc content between Pacific MORB and Hawaiian basalt reflects the greater importance of residual garnet during the formation of Hawaiian lavas, and the decrease in Sc content at <5 wt% MgO in Nintoku lavas reflects clinopyroxene fractionation.

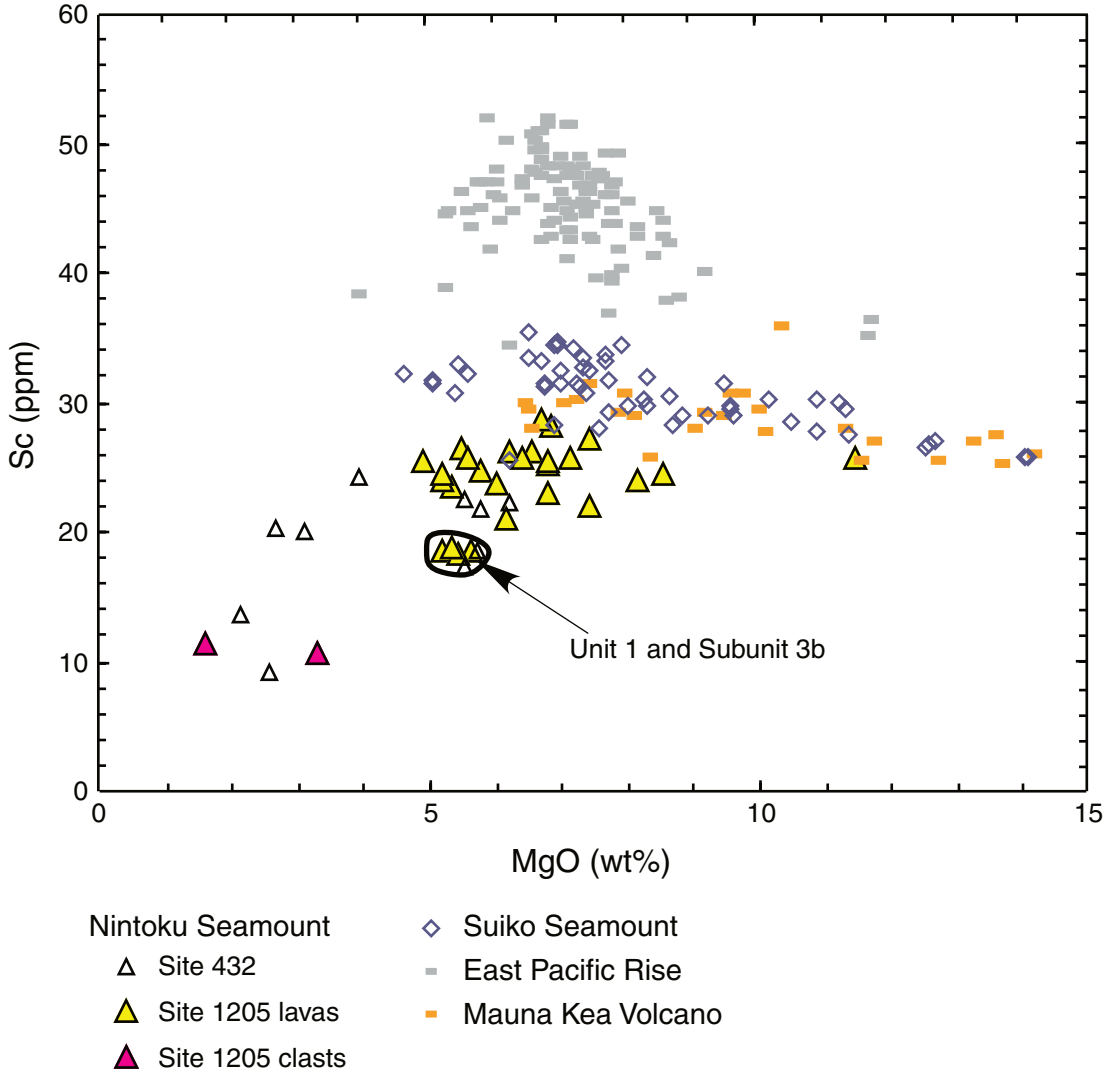

Figure F22. Ratios of Zr/Ba, Zr/Sr, Ti/Ba, and Ti/Sr vs. MgO content. At a given MgO content, these ratios increase in the order: Nintoku Seamount < Mauna Kea Volcano < Suiko Seamount (data from Kirkpatrick et al., 1980; Yang et al., 1996, S. Huang and F.A. Frey, unpubl. data; M. Regelous et al., unpubl. data).

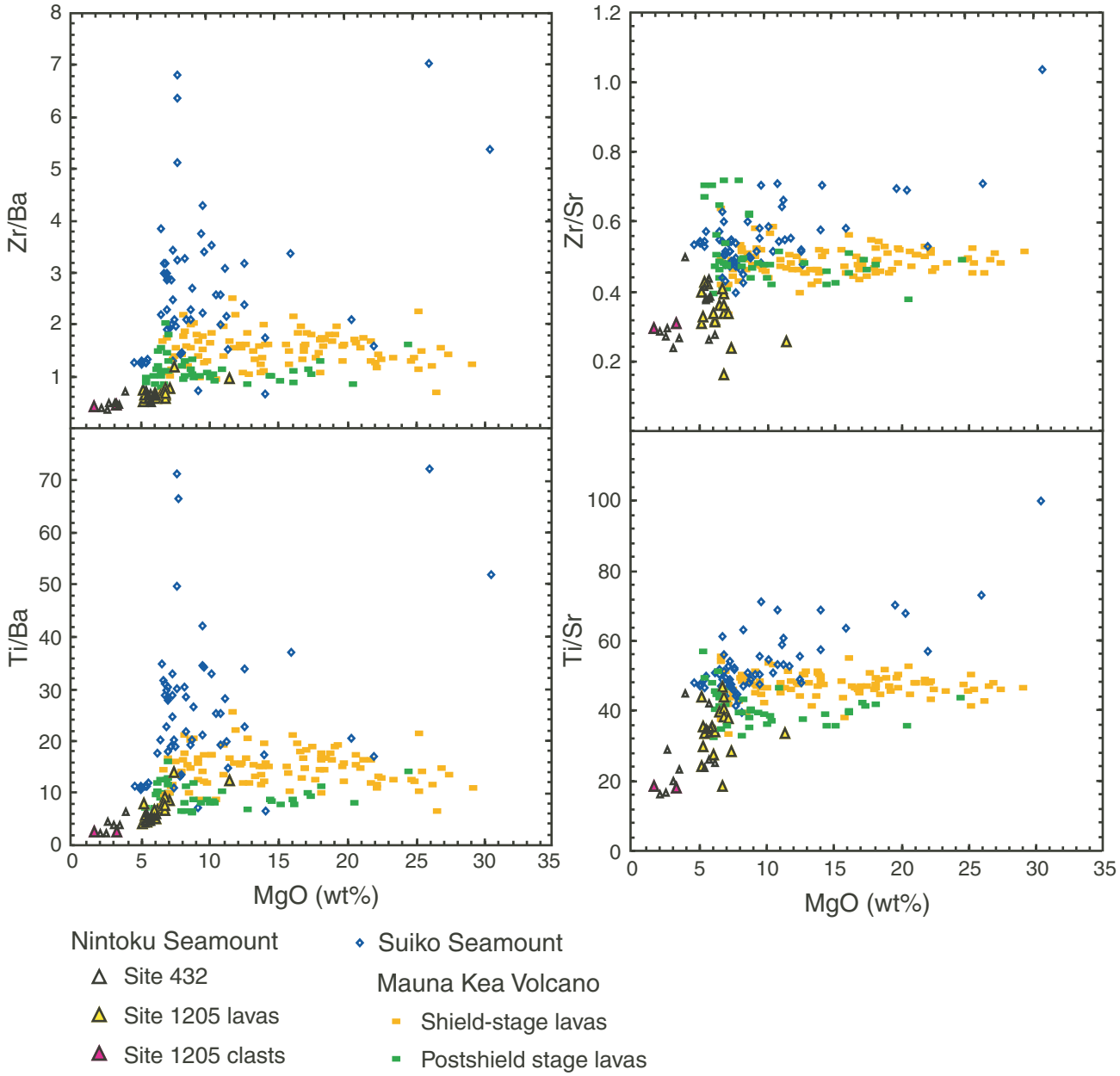

Figure F23. Abundance of Y and Zr/Y vs. Zr content. In the Zr–Y panel, the trends for East Pacific Rise (EPR) MORB (data from J.M. Sinton, pers. comm., 1998), three Hawaiian shields, and Suiko Seamount define a fan-shaped array of lines, but the trend for lavas from Nintoku Seamount crosscuts the trends for Suiko Seamount and the Hawaiian volcanoes (data from Kirkpatrick et al., 1980; Frey et al., 1994; Rhodes, 1996; Yang et al., 1996; S. Huang and F.A. Frey, unpubl. data; M. Regelous et al., unpubl. data). The Zr/Y–Zr panel shows that lavas from Nintoku Seamount display a wider range in Zr/Y than EPR MORB and Mauna Kea shield lavas. HSDP = Hawaiian Scientific Drilling Project.

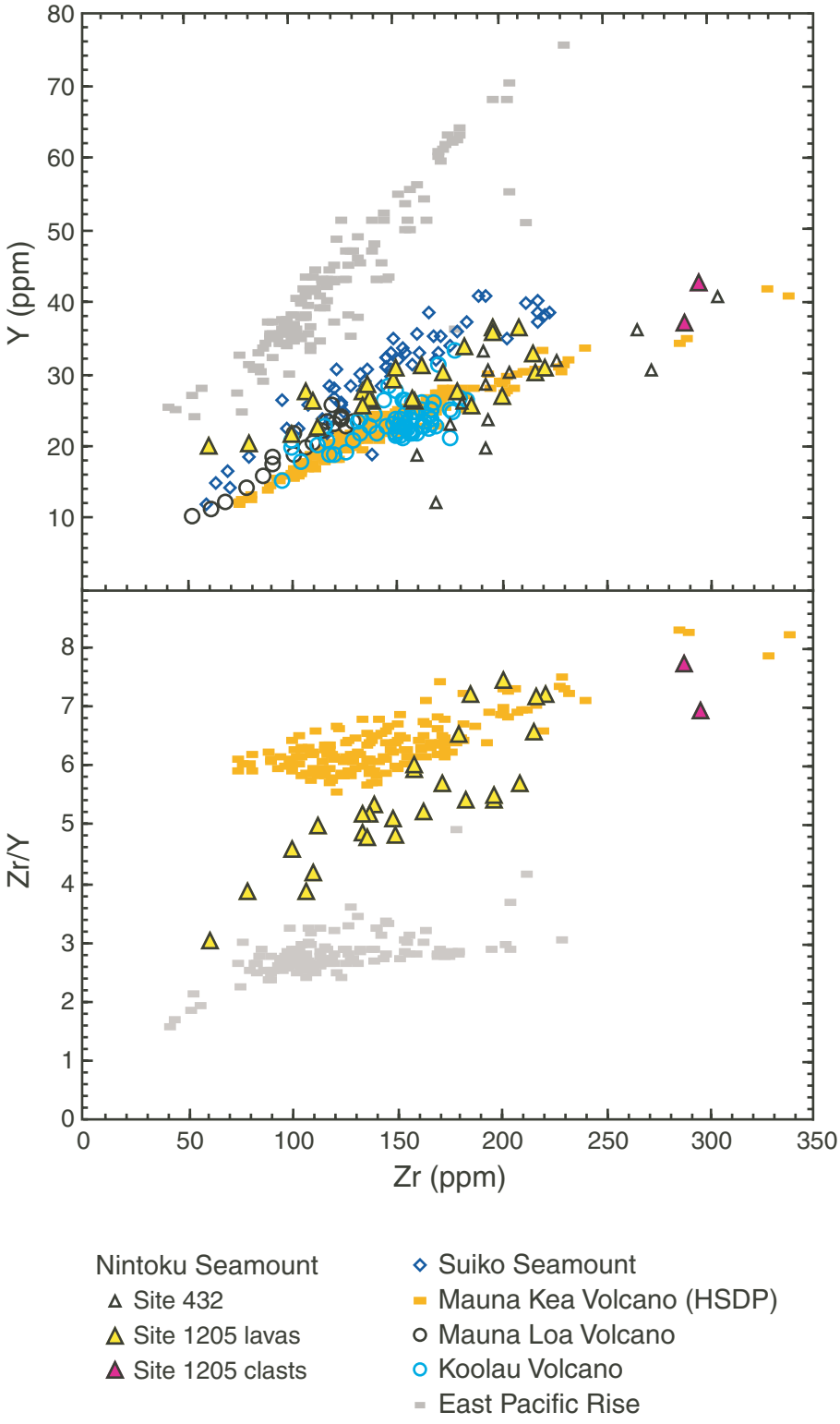

Figure F24. Composite figure showing the alteration degree, mineral assemblages, vesicle occurrence and vesicle and vein fillings for Hole 1205A. Also shown is the core recovery downhole. Green = sedimentary units, yellow = volcaniclastic units, red = soil horizons, blue = lava flow units. TD = total depth.

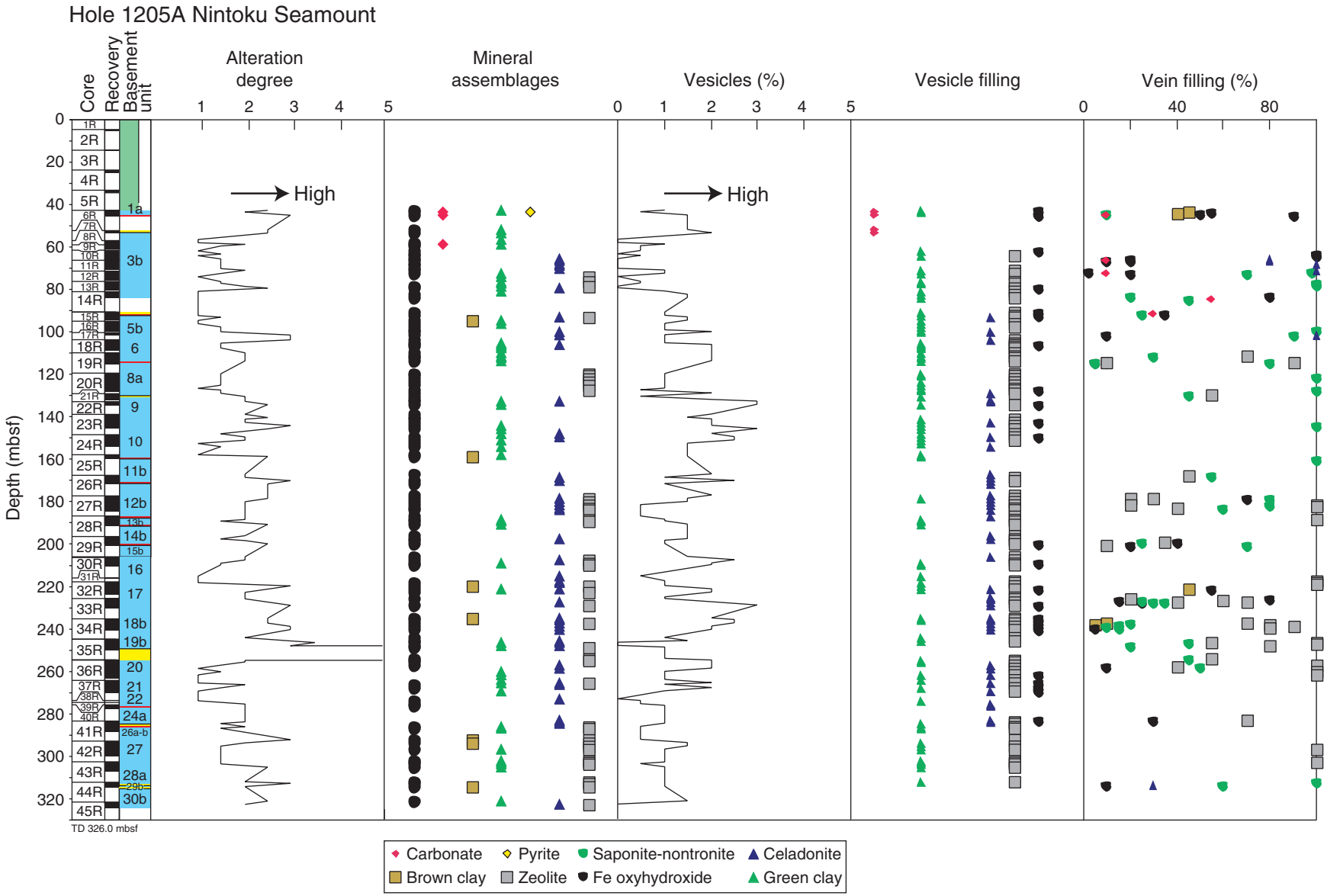

Figure F25. Photograph of a vesicle filled with celadonite and saponite (interval 197-1205A-21R-2, 94–113 cm).

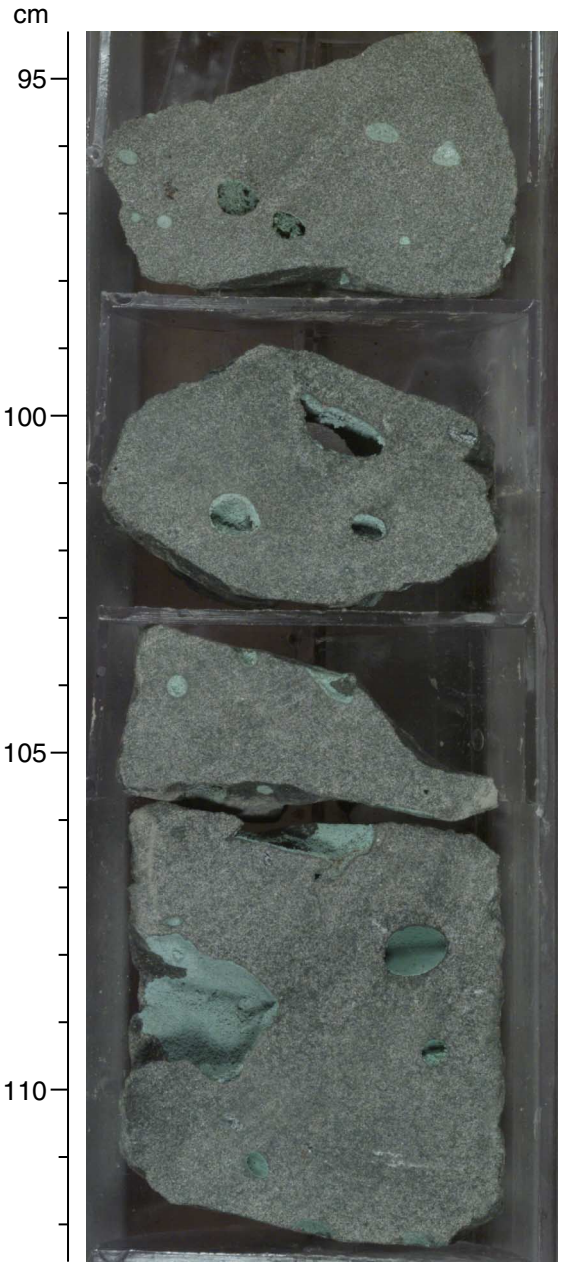

Figure F26. Variations of LOI (loss on ignition), K_2O abundances, Cu/Zr, Co/Zr, and Zn/Zr ratios with depth in the Hole 1205A sequence. Also shown is the core recovery downhole. Green = sedimentary units, yellow = volcaniclastic units, red = soil horizons, blue = lava flow units. TD = total depth.

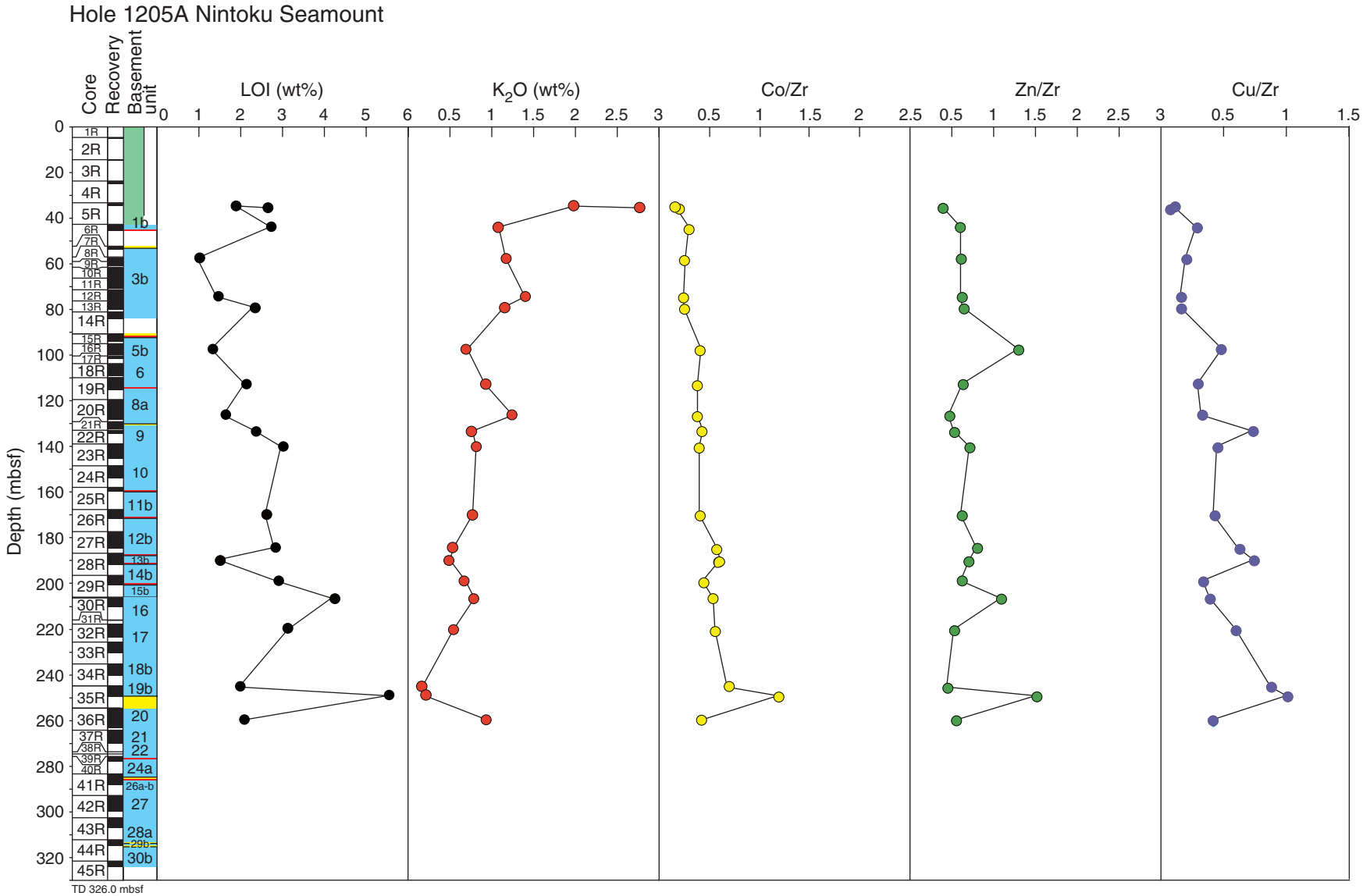

Figure F27. Low-field volume-normalized (bulk) magnetic susceptibility, Koenigsberger ratio, and median destructive field (MDF) vs. depth for Hole 1205a basalt samples. Open symbols = oriented samples. Closed symbols = unoriented pebbles given a laboratory orientation direction.

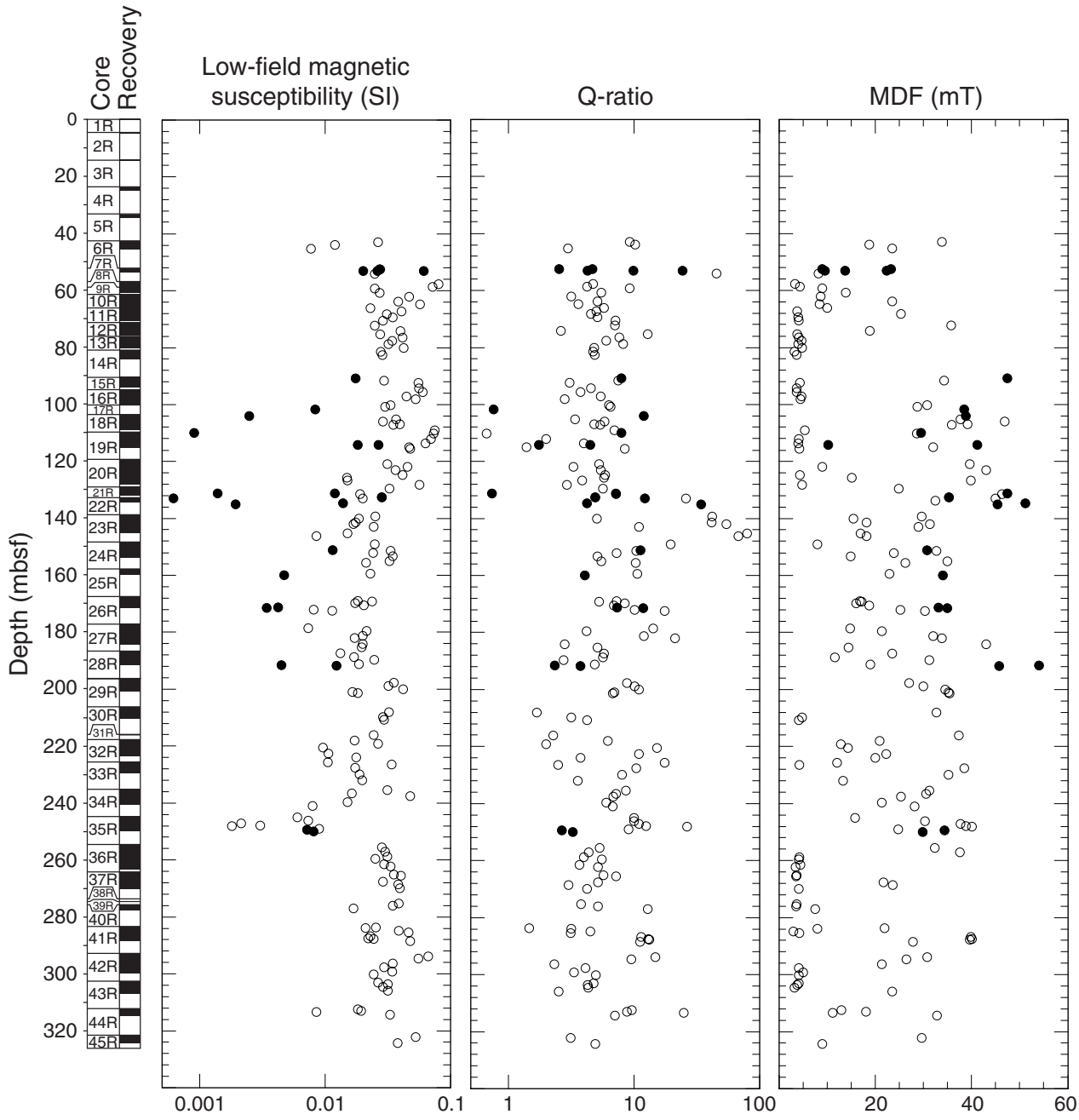

Figure F28. Examples of Lowrie-Fuller tests (Lowrie and Fuller, 1971) conducted on Site 1205 basalt: Samples (**A**) 197-1205A-14R-2, 16–18 cm, (**B**) 19R-4, 143–145 cm, (**C**) 24R-2, 141–143 cm, (**D**) 27R-4, 44–46 cm, (**E**) 29R-3, 114–116 cm, and (**F**) 35R-2, 36–38 cm. ARM = anhysteretic remanent magnetization, SIRM = saturation isothermal remanent magnetization, SD = single-domain, MD = multidomain, AF = alternating field.

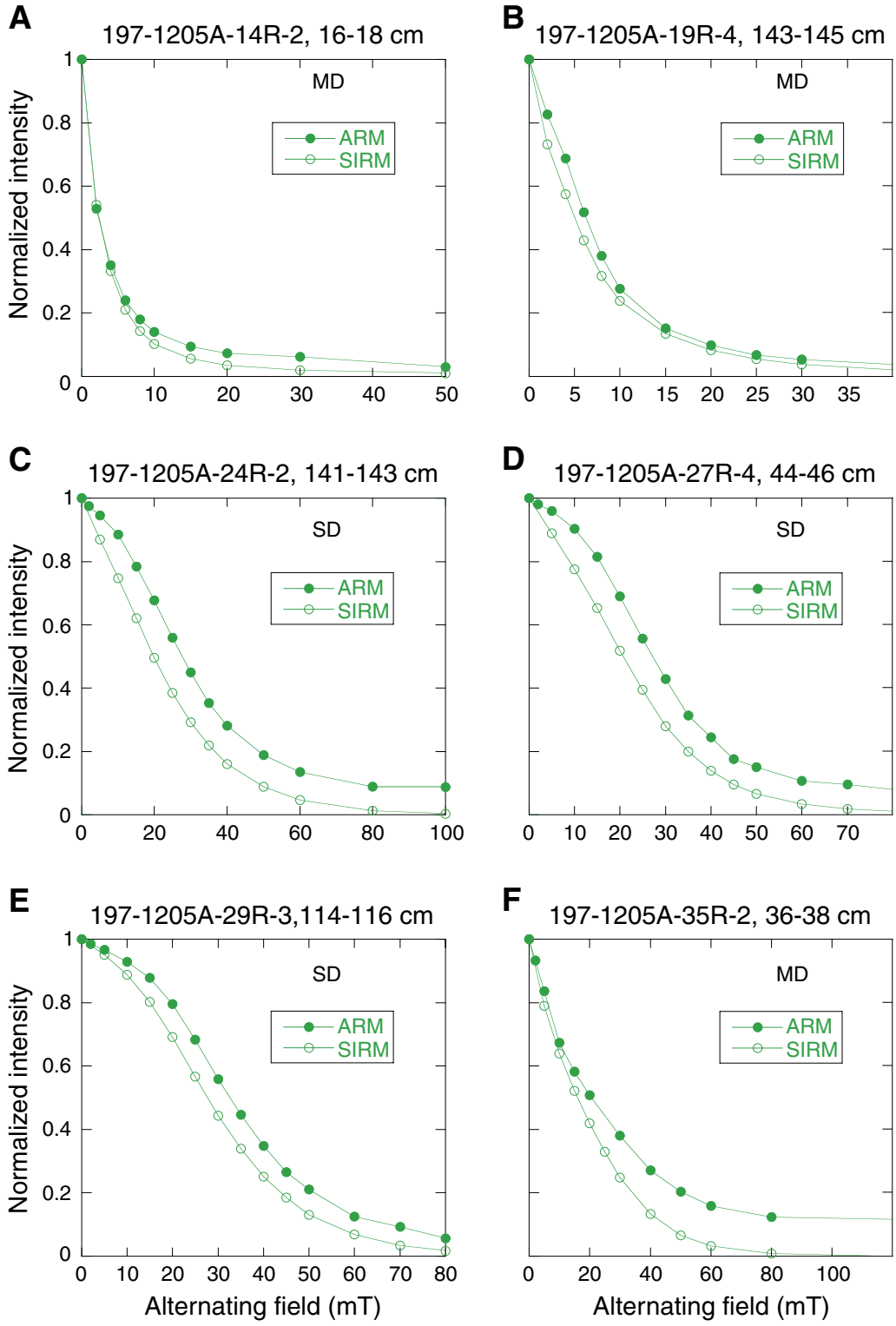

Figure F29. Examples of isothermal remanent magnetization (IRM) acquisition and demagnetization (backfield IRM) (see "Lowrie-Fuller Tests and Coercivity of Remanence Measurements," p. 21) used to calculate coercivity of remanence from Hole 1205A basalt: Samples (**A**) 197-1205A-4R-2, 16–18 cm, (**B**) 19R-4, 143–145 cm, (**C**) 24R-2, 141–143 cm, (**D**) 27R-4, 44–46 cm, (**E**) 29R-3, 114–116 cm, and (**F**) 35R-2, 36–38 cm. AF = alternating field, SD = single-domain, MD = multidomain.

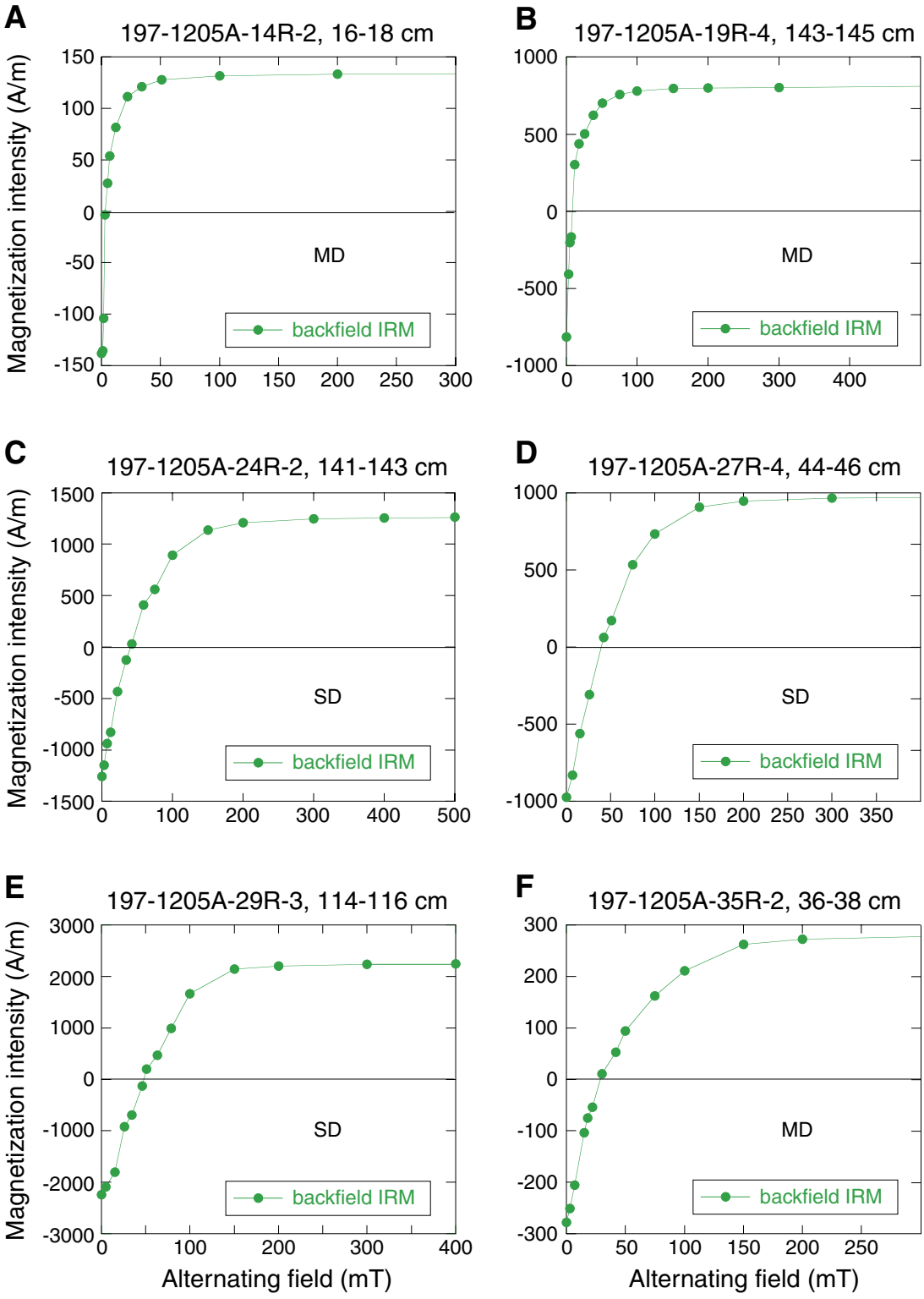

Figure F30. Examples of samples that may contain superparamagnetic grains. Normalized NRM decay spectra (A, C) suggest SD-like behavior, whereas Lowrie-Fuller tests (B, D) (Lowrie and Fuller, 1971) conducted on these samples suggest multidomain (MD) behavior. **A, B.** Sample 197-1205A-20R-6, 12–14 cm. **C, D.** Sample 197-1205A-35R-2, 36–38 cm. ARM = anhysteric remanent magnetization, SIRM = saturation remanent magnetization, AF = alternating field.

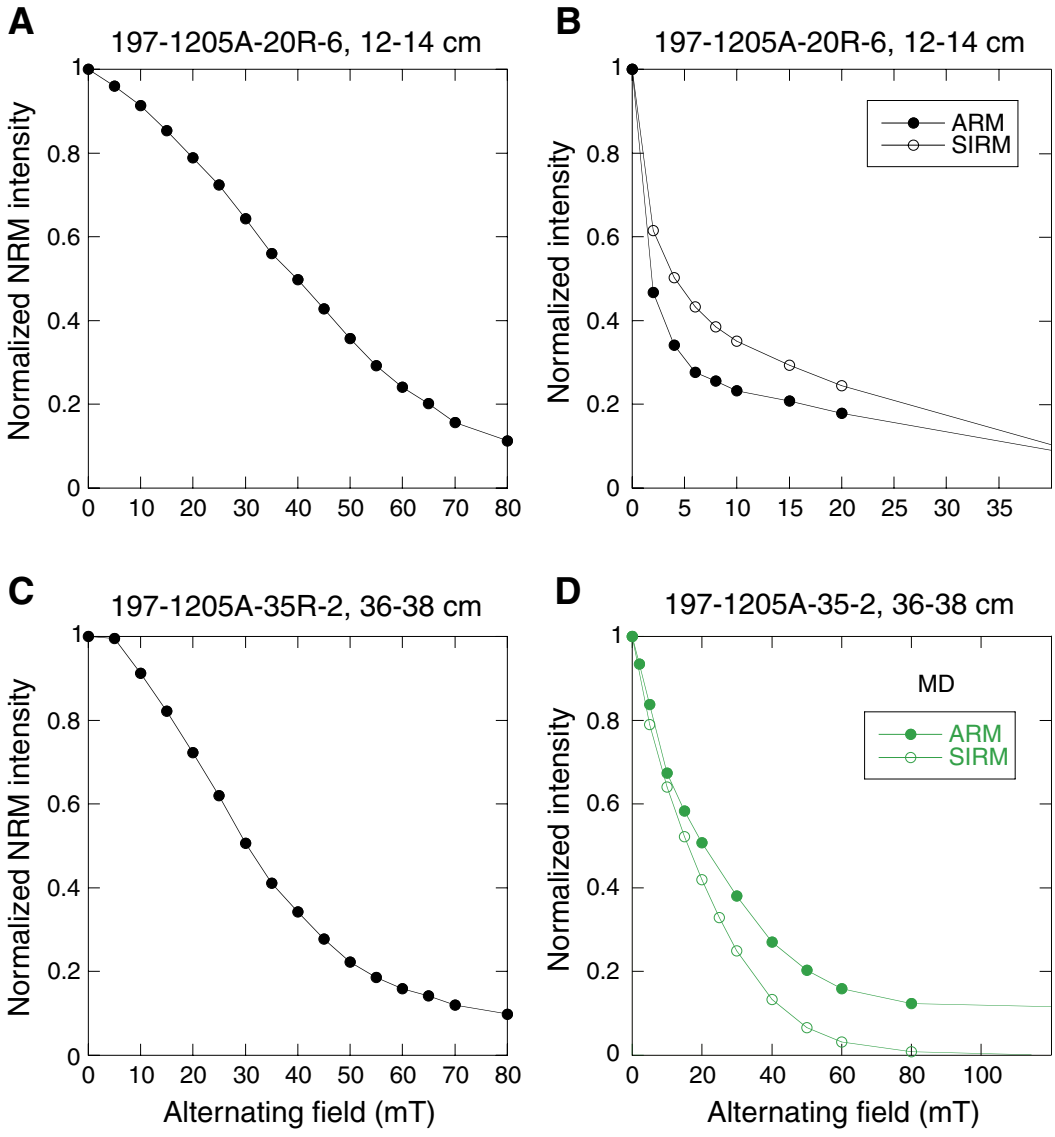

Figure F31. Example orthogonal vector plots showing well-defined, stable magnetic behavior recorded by Hole 1205A basalt: Samples (**A**) 197-1205A-13R-2, 39–41 cm, (**B**) 25R-2, 17–19 cm, (**C**) 26R-1, 117–119 cm, (**D**) 28R-3, 4–6 cm, (**E**) 29R-4, 126–128 cm, and (**F**) 44R-1, 68–70 cm. Numbers adjacent to the symbols signify alternating-field demagnetization level. Open symbols = inclination values, closed symbols = declination values.

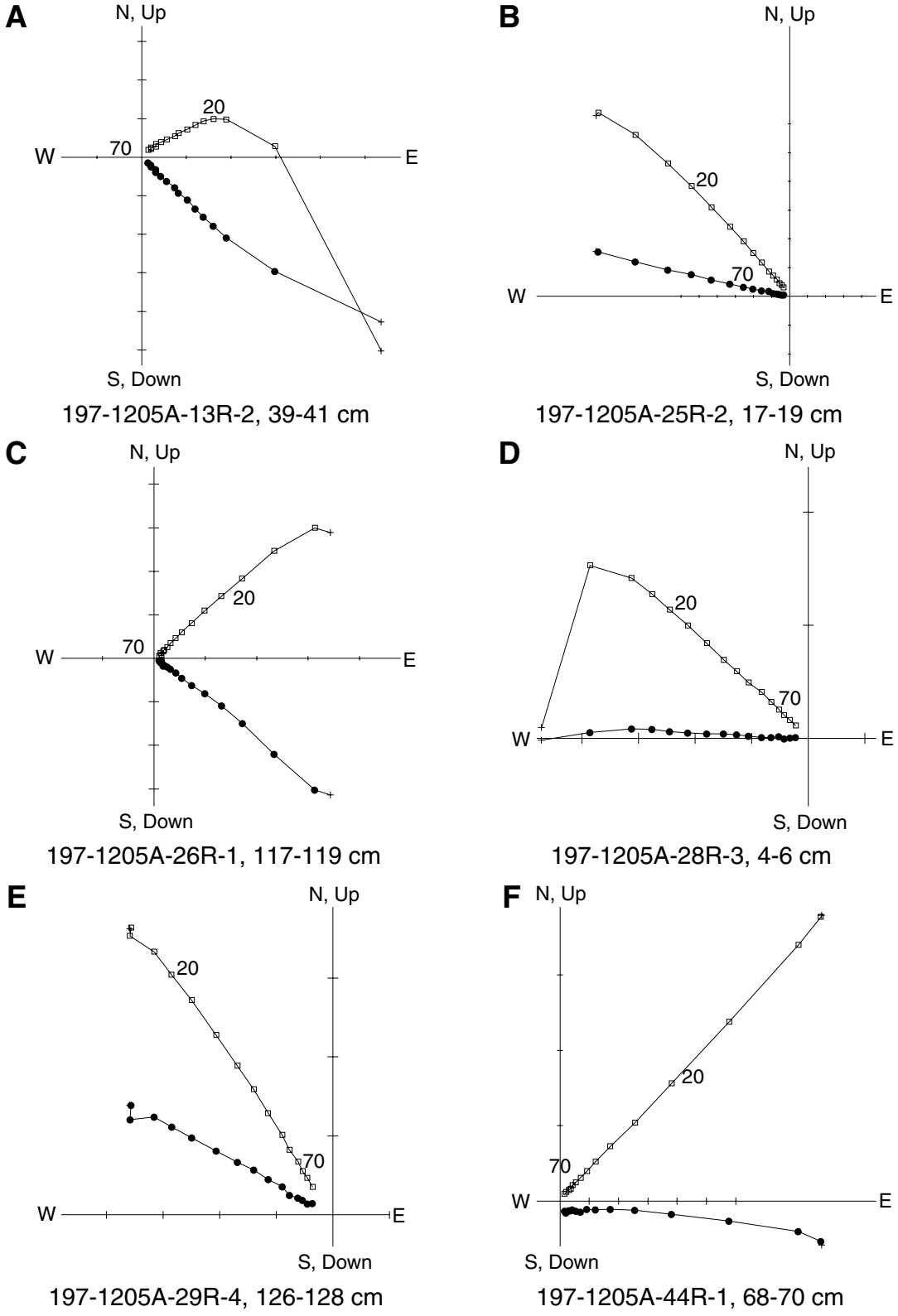

Figure F32. $\Delta RM = (RM_0 - RM_5)/(RM_{20}-RM_{50})$ (log scale) vs. compressional wave velocity. ΔRM is the vector difference between steps of progressive AF demagnetization (see **"Magnetically "Soft" Components and Rock Alteration,"** p. 22).

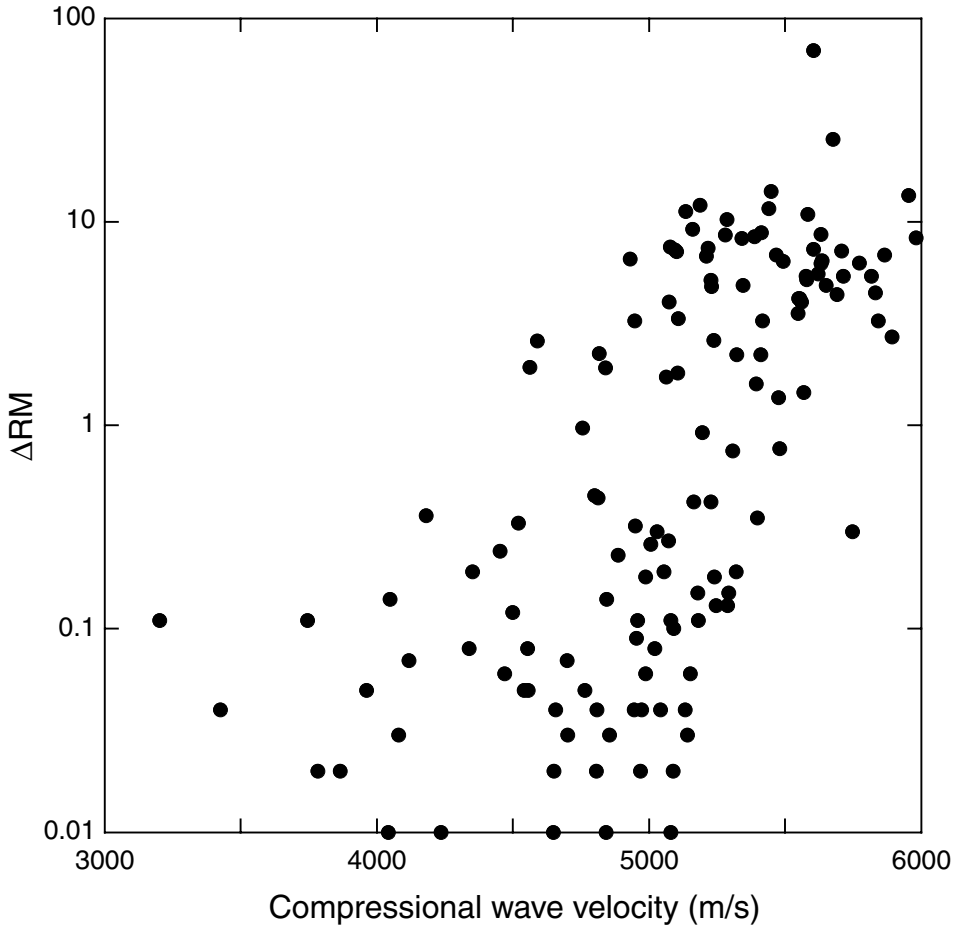

Figure F33. Example orthogonal vector plots showing nonideal behavior as recorded by Hole 1205A basalt: Samples (**A**) 197-1205A-14R-1, 55–57 cm, (**B**) 18R-1, 130–132 cm, (**C**) 33R-1, 36–38 cm, (**D**) 36R-5, 46–48 cm, (**E**) 41R-2, 96–98 cm, and (**F**) 42R-1, 113–115 cm. Open symbols = inclination values, closed symbols = declination values.

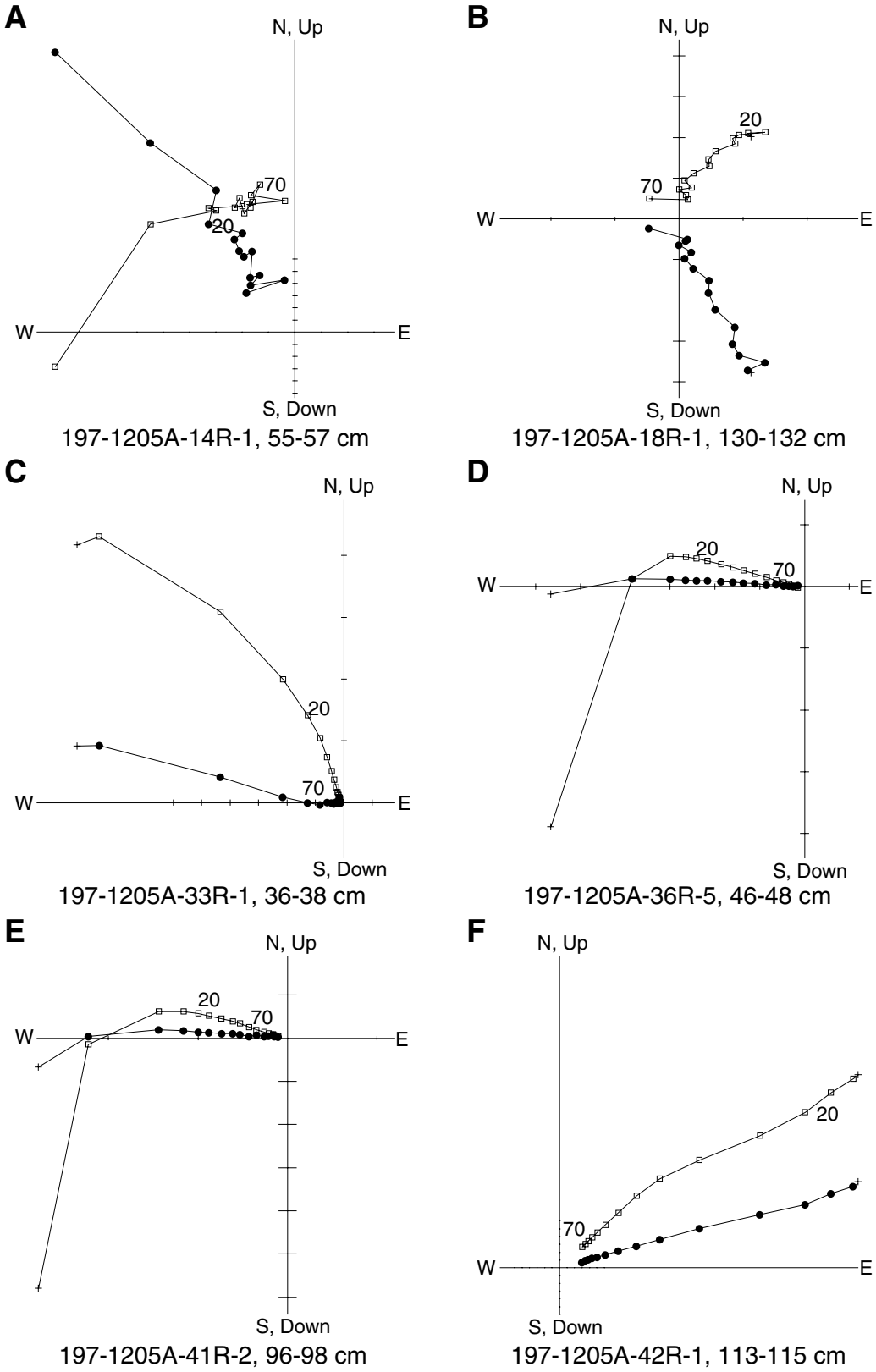

Figure F34. Example orthogonal vector plots showing well-defined magnetic components recorded by Hole 1204A basalt that are not completely demagnetized by the alternating field treatment applied: Samples (**A**) 197-1205A-12R-1, 93–95 cm, (**B**) 15R-1, 90–92 cm, (**C**) 17R-1, 58–60 cm, (**D**) 18R-3, 97–99 cm, (**E**) 29R-1, 116–118 cm, and (**F**) 35R-4, 115–117 cm. Open symbols = inclination values, closed symbols = declination values.

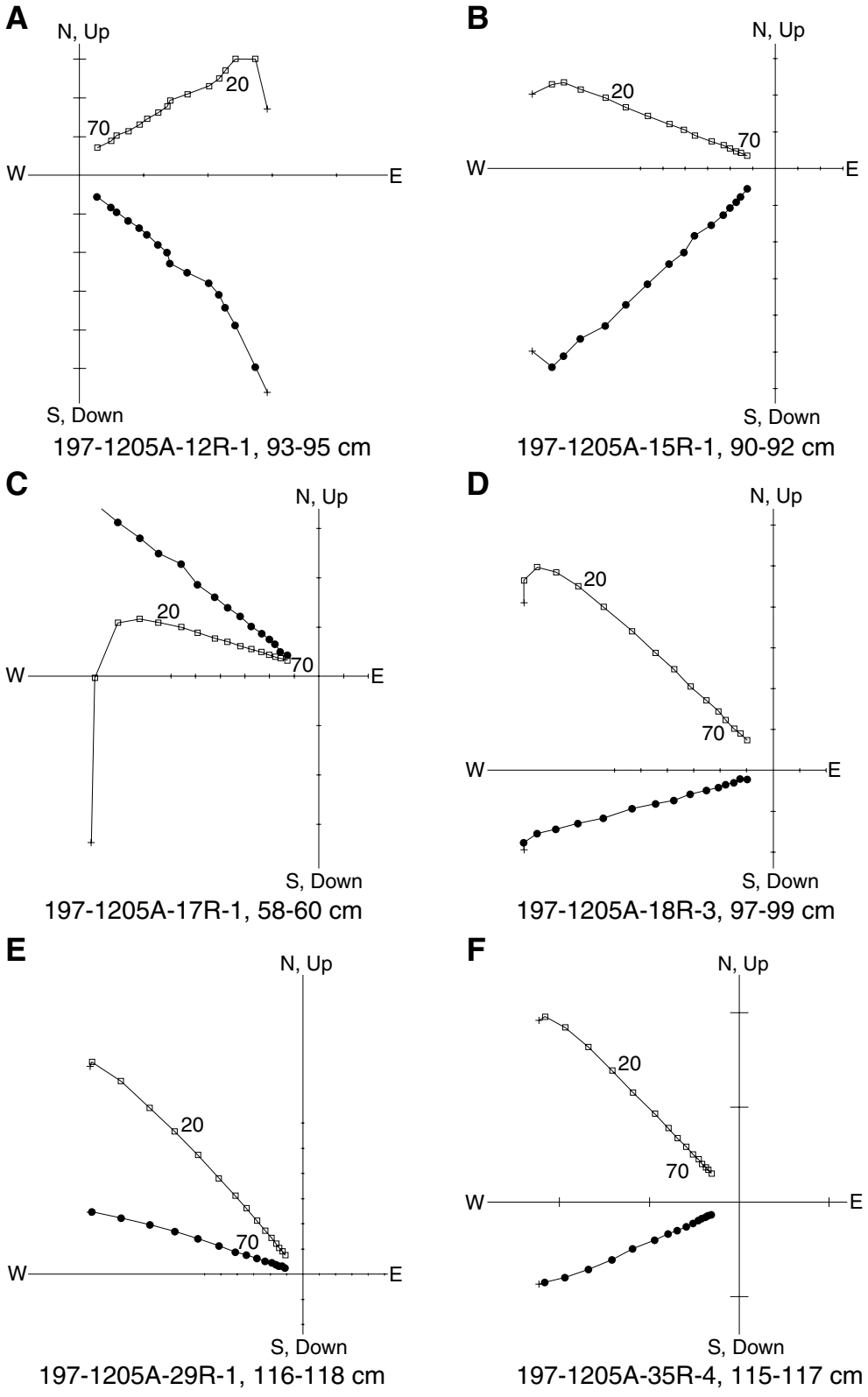

Figure F35. Histogram of inclination values derived from principal component analyses of lava flows recovered at Site 1205 compared to a synthetic Fisher distribution (Fisher, 1953) having the same precision parameter (*k*) as the experimental data.

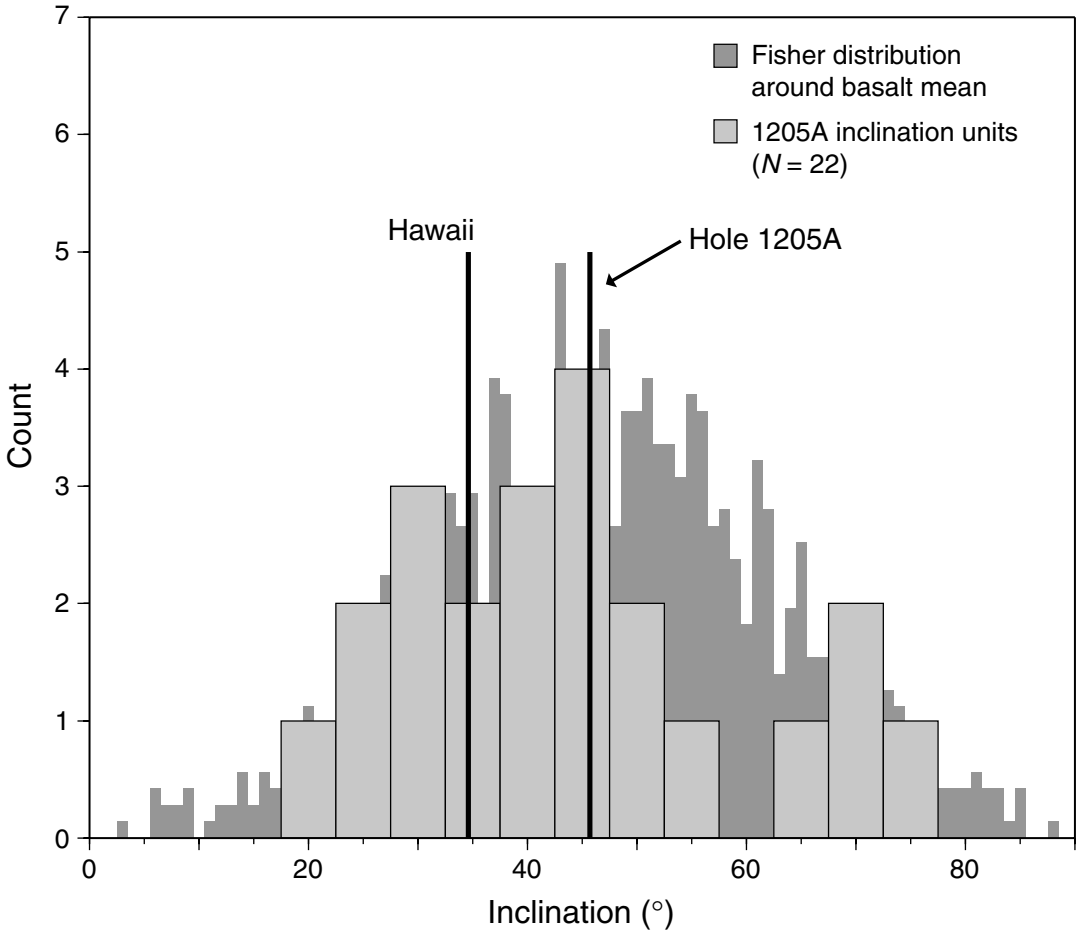

Figure F36. Summary of physical properties measurements. **A**. Natural gamma ray. **B**. Bulk density. **C**. Grain density. **D**. Porosity.

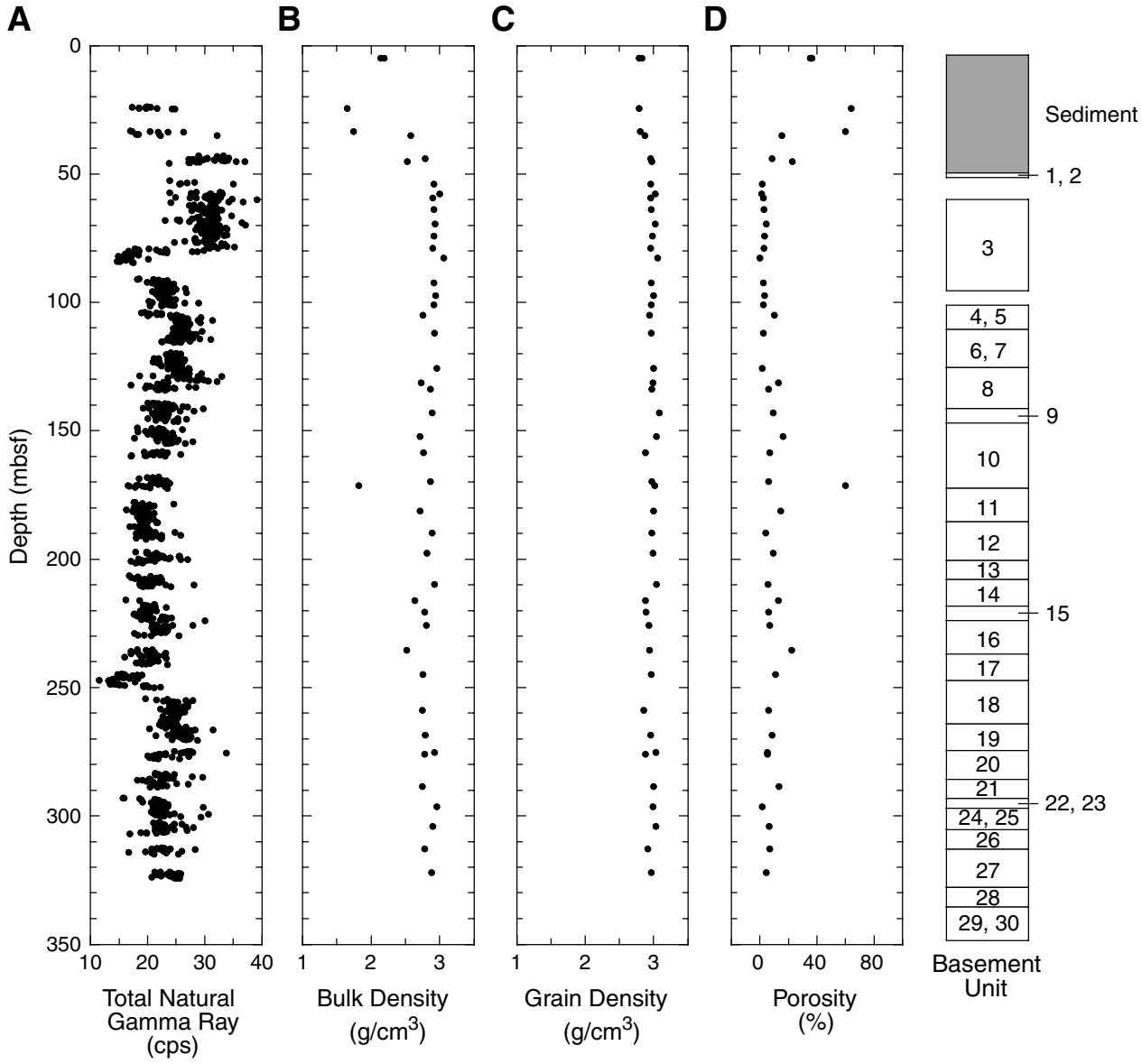

Figure F37. Thermal conductivity measurements vs. depth.

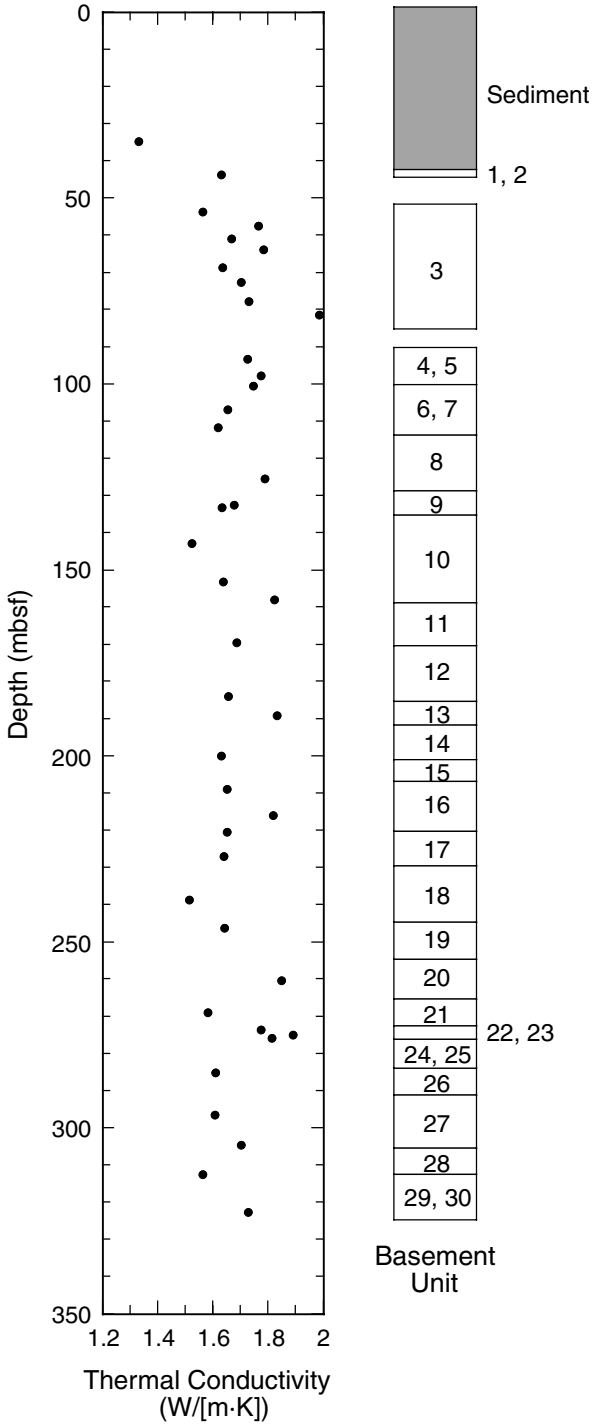

Figure F38. Compressional wave velocity.

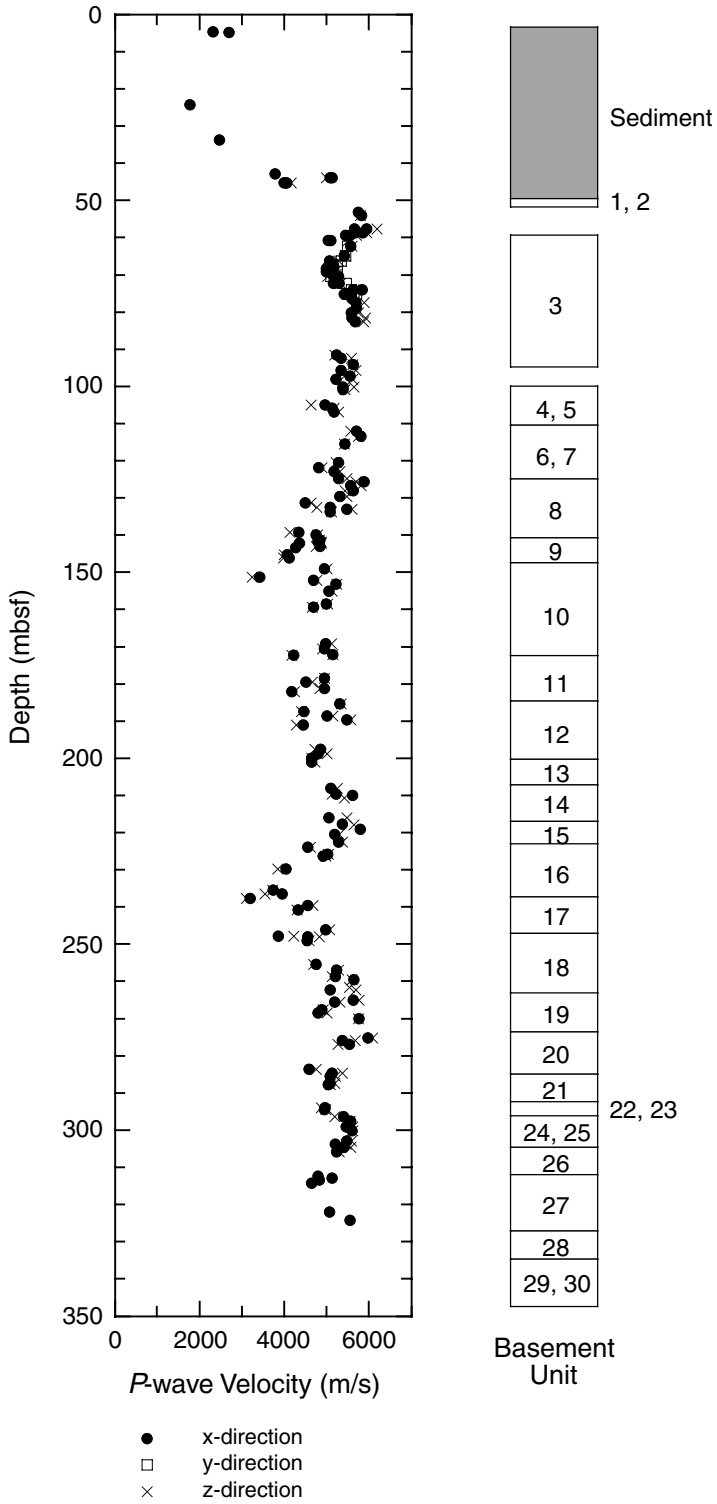

Figure F39. Compressional wave velocity plotted against bulk density at the same sampling depth.

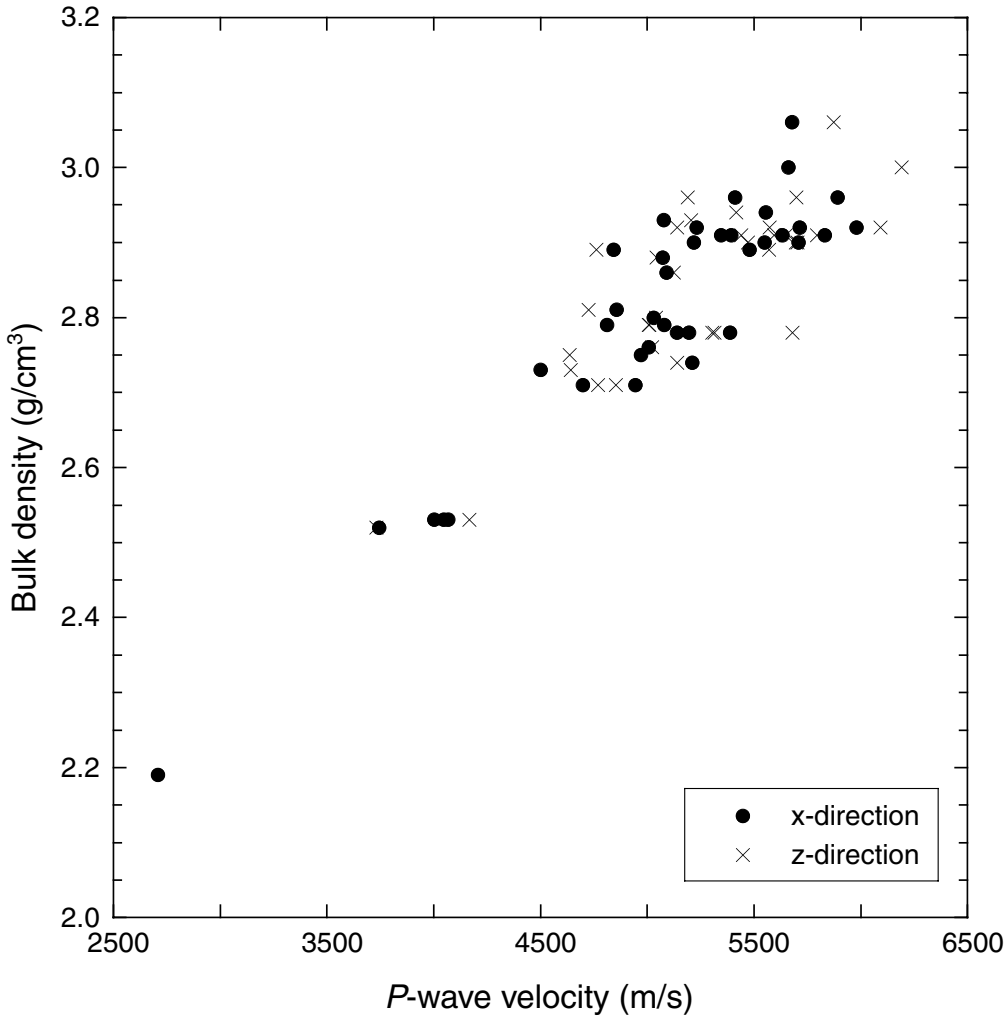

Figure F40. Ship track for Leg 197, Site 1205 seismic reflection survey. Tick marks show half-hour time intervals.

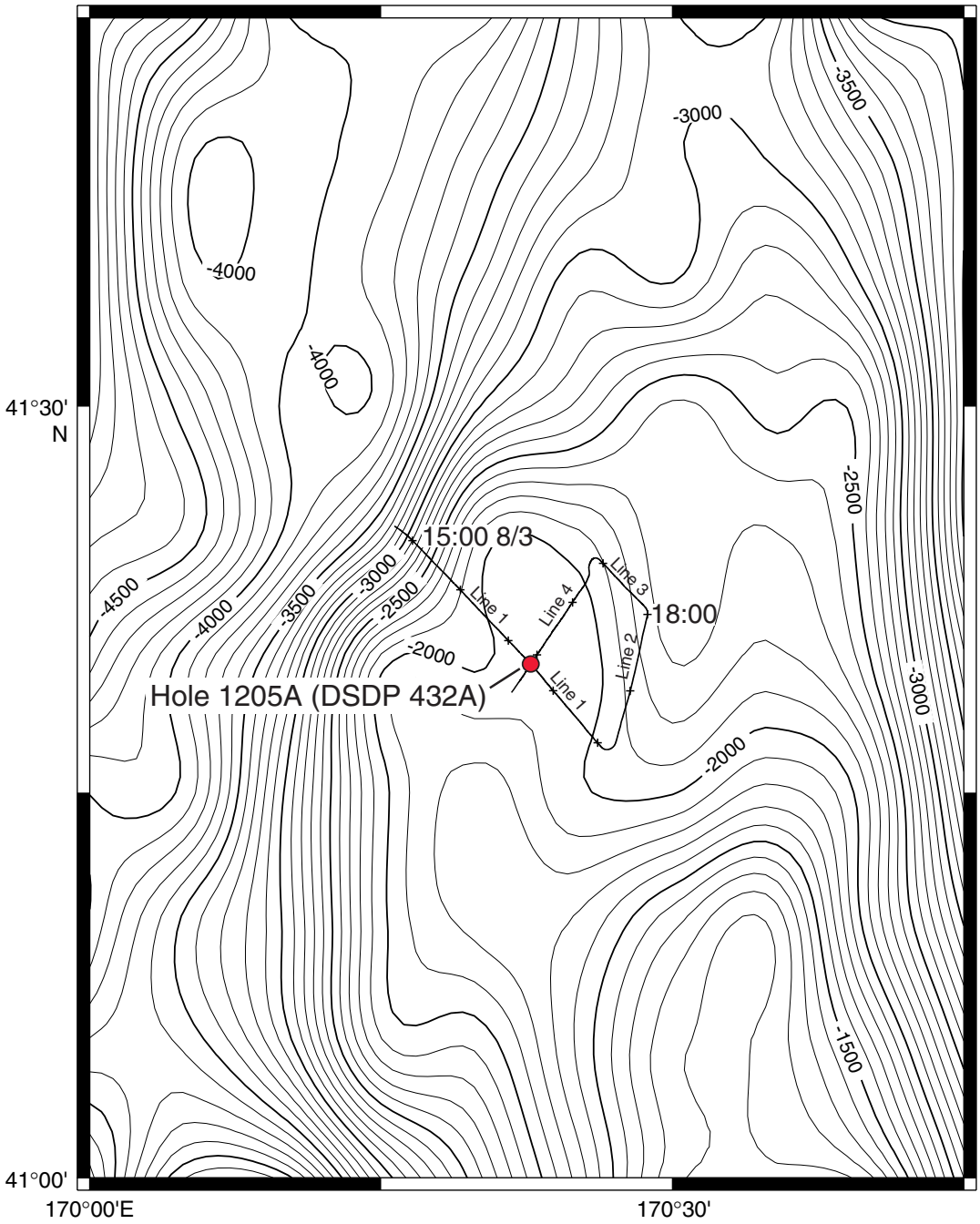

Figure F41. Three-km-long Fk-migrated time section of survey Line 1. Data are bandpass filtered between 60 and 150 Hz. Hole 1205A is at about shotpoint 1225. Trace-to-trace distance = ~11 m, vertical exaggeration at the seafloor = ~8:1, bottom of Hole 1205A = ~1.92 s two-way traveltime.

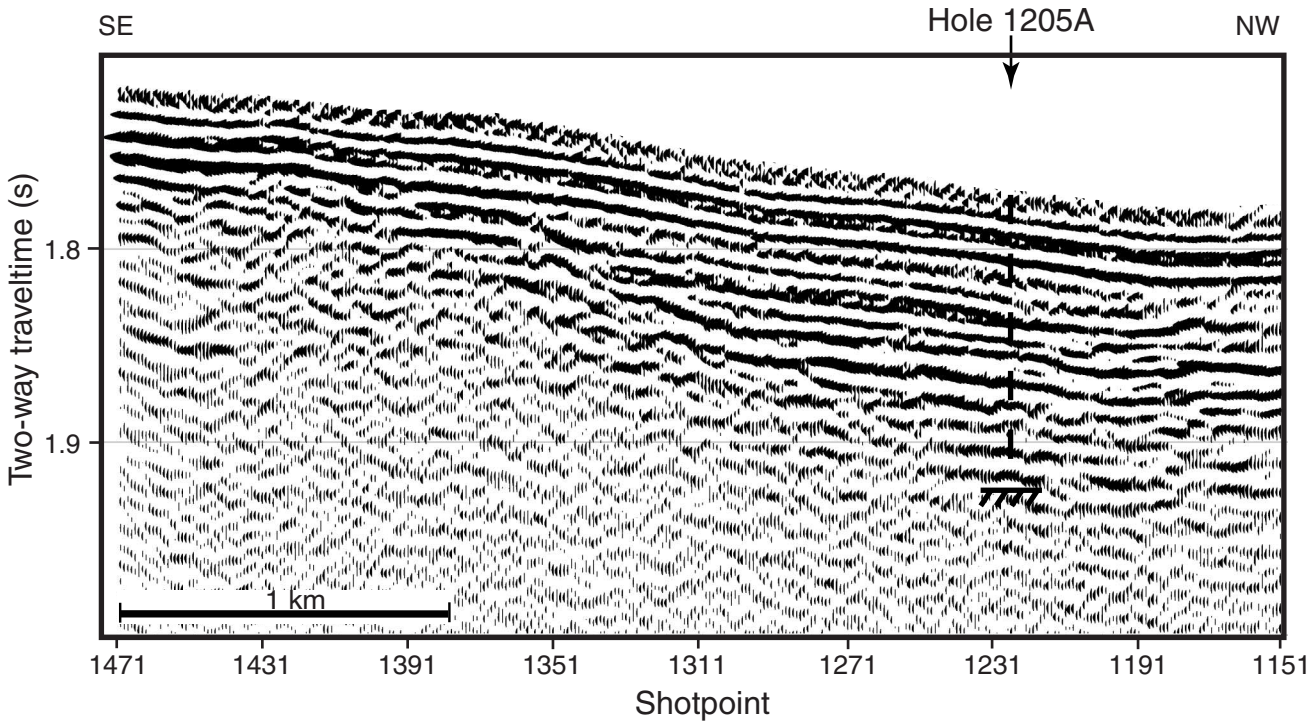

Figure F42. Three-km-long Fk-migrated time section of survey Line 4. Data are bandpass filtered between 60 and 150 Hz. Hole 1205A is approximately shotpoint 4216. Trace-to-trace distance = ~9.9 m, vertical exaggeration at the seafloor = ~7:1, bottom of Hole 1205A = ~1.92 s two-way traveltime.

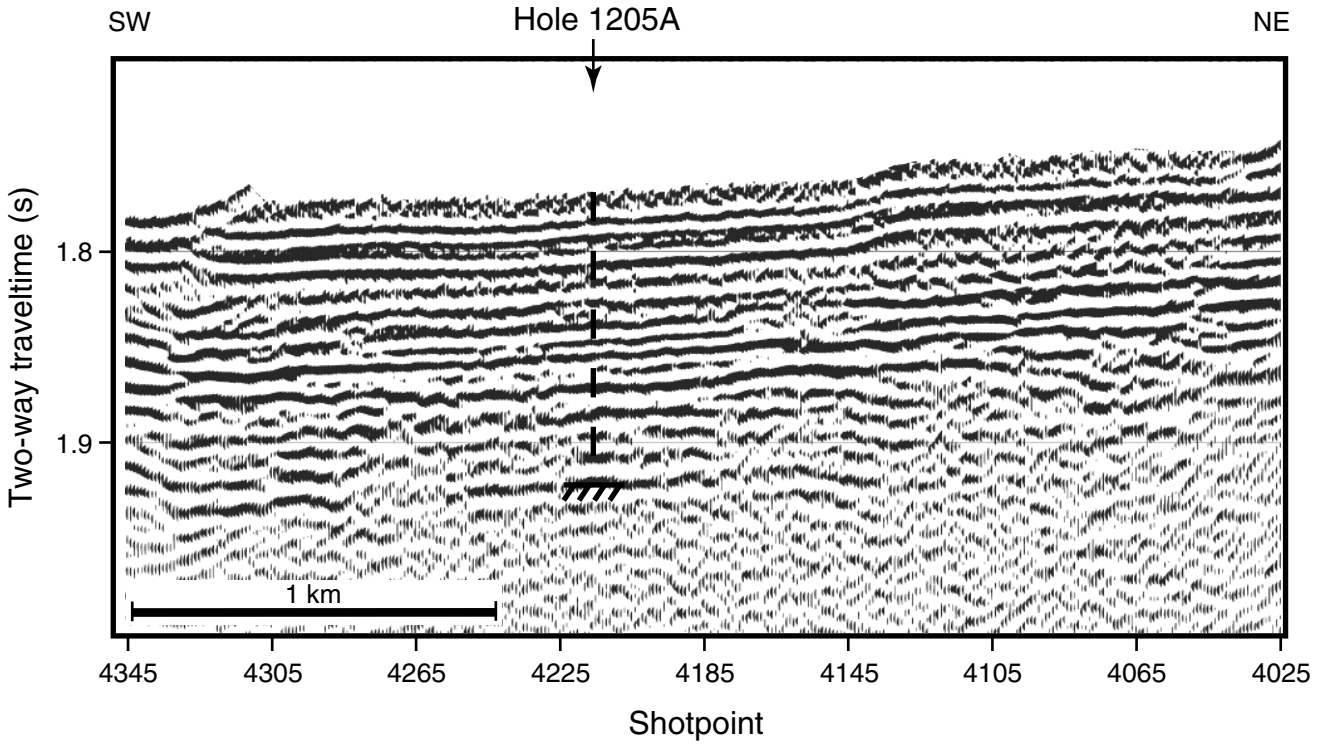

Table T1. Coring summary, Site 1205.

Latitude: 41°19.9986′N
Longitude:170°22.6992′E
Time on site (hr): 191.5 (0630 hr, 4 Aug–0600 hr, 12 Aug 2001)
Seafloor (drill pipe measurement from rig floor, mbrf): 1321
Distance between rig floor and sea level (m): 11.1
Water depth (drill pipe measurement from sea level, m): 1309.9
Total depth (drill pipe measurement from rig floor, mbrf): 1647.0
Total penetration (meters below seafloor, mbsf): 326.0
Total length of cored section (m): 326
Total length of drilled intervals (m): 0
Total core recovered (m): 165.62
Core recovery (%): 50.8
Total number of cores: 45

Core	Date (August 2001)	Ship time (local)	Depth (mbsf) Top	Depth (mbsf) Bottom	Length (m) Cored	Length (m) Recovered	Recovery (%)	Comments
197-1205A-								
1R	4	1325	0.0	4.6	4.6	0.09	2.0	AHC
2R	4	1545	4.6	14.2	9.6	0.59	6.2	AHC
3R	4	1655	14.2	23.7	9.5	0.40	4.2	AHC
4R	4	1755	23.7	33.2	9.5	1.24	13.1	AHC
5R	4	1945	33.2	42.7	9.5	1.55	16.3	AHC
6R	4	2230	42.7	52.2	9.5	2.74	28.8	AHC
7R	5	0155	52.2	56.9	4.7	1.30	27.7	AHC
8R	5	0650	56.9	58.9	2.0	1.98	99.0	AHC
9R	5	0925	58.9	61.7	2.8	2.01	71.8	AHC
10R	5	1325	61.7	66.2	4.5	4.29	95.3	AHC
11R	5	1750	66.2	71.3	5.1	4.60	90.2	AHC
12R	5	2310	71.3	76.1	4.8	4.49	93.5	AHC
13R	6	0345	76.1	81.0	4.9	4.13	84.3	AHC
14R	6	0840	81.0	90.7	9.7	3.10	32.0	AHC
15R	6	1205	90.7	95.0	4.3	3.68	85.6	AHC
16R	6	1540	95.0	100.3	5.3	5.06	95.5	AHC
17R	6	1745	100.3	103.8	3.5	1.43	40.9	AHC
18R	6	2115	103.8	109.9	6.1	5.11	83.8	AHC
19R	7	0220	109.9	119.6	9.7	5.41	55.8	AHC
20R	7	0810	119.6	129.2	9.6	8.69	90.5	AHC
21R	7	1030	129.2	132.9	3.7	3.24	87.6	AHC
22R	8	0200	132.9	138.9	6.0	1.84	30.7	AHC
23R	8	0500	138.9	148.5	9.6	6.56	68.3	AHC
24R	8	0845	148.5	158.0	9.5	5.35	56.3	AHC
25R	8	1120	158.0	167.7	9.7	1.76	18.1	AHC
26R	8	1420	167.7	177.3	9.6	3.93	40.9	AHC
27R	8	1825	177.3	186.9	9.6	7.29	75.9	AHC
28R	8	2230	186.9	196.5	9.6	4.84	50.4	AHC
29R	9	0150	196.5	206.1	9.6	4.25	44.3	AHC
30R	9	0555	206.1	215.8	9.7	4.03	41.6	AHC
31R	9	1230	215.8	217.5	1.7	0.29	17.1	AHC
32R	9	1640	217.5	225.4	7.9	5.92	74.9	AHC
35R	10	0335	244.6	254.3	9.7	5.07	52.3	AHC
36R	10	0815	254.3	264.0	9.7	8.86	91.3	AHC
37R	10	1205	264.0	273.6	9.6	6.02	62.7	AHC
38R	10	1345	273.6	274.6	1.0	0.09	9.0	AHC
39R	10	1640	274.6	275.6	1.0	0.94	94.0	AHC
40R	10	1925	275.6	283.2	7.6	2.11	27.8	AHC
41R	11	0005	283.2	292.8	9.6	5.22	54.4	AHC
42R	11	0420	292.8	302.5	9.7	7.07	72.9	AHC
43R	11	0720	302.5	312.2	9.7	4.41	45.5	AHC
44R	11	0950	312.2	321.5	9.3	2.40	25.8	AHC
45R	11	1240	321.5	326.0	4.5	2.75	61.1	AHC
				Cored totals:	326.0	165.62	50.8	

Note: AHC = active heave compensation.

Table T2. Carbonate data, Site 1205.

Core, section, interval (cm)	Depth (mbsf)	Inorganic C (wt%)	$CaCO_3$ (wt%)
197-1205A-			
2R-1, 12–13	4.72	7.3	60.4
3R-1, 24–25	14.44	5.4	44.6
4R-1, 2–3	23.72	3.2	26.9
4R-1, 106–107	24.76	3.7	31.0
5R-1, 29–30	33.49	3.4	28.1
6R-3, 70–71	45.78	0.0	0.1
6R-3, 79–80	45.87	0.0	0.1

Table T3. Summary of abundance and distribution of nannofossils, and biozonal assignments, Site 1205.

Core, section, interval (cm)	Depth (mbsf)	Sample code	Zone From	Age From	Preparation*	Preservation	Group abundance	Nannofossils: *Braarudosphaera bigelowii*	*Braarudosphaera discula*	*Campylosphaera dela*	*Chiasmolithus bidens*	*Clausicoccus fenestratus*	*Coccolithus pelagicus*	*Coronocyclus nitescens*	*Cruciplacolithus asymmetricus*	*Discoaster binodosus*	*Discoaster multiradiatus*	*Ellipsolithus macellus*	*Micrantholithus entaster*	*Neochiastozygus chiastus*	*Neococcolithes protenus*	*Rhabdosphaera pinguis*	*Toweius eminens*	*Toweius pertusus*	*Tribrachiatus contortus*	*Zygodiscus adamas*	*Zygrhablithus bijugatus*
197-1205A-																										
2R-1, 10–11	4.70	BIO	NP10	early Eocene	Smear slide	P	R			R			F						R			R	F		R		
3R-1, 35–40	14.55	PAL	NP10	early Eocene	Smear slide	P	R	R	R		R	R	R	R				R	R	R	R		F	R	R	R	R
4R-1, 98–99	24.68	BIO	NP10	early Eocene	Smear slide	M	R	R	R	R	R		R	R	R	R	R			R		R	F	F			R
4R-CC, 8–12	24.90	PAL	NP10	early Eocene	Smear slide	M	F	R	R	R			R				R		R		R	R	F	F	R	R	R
5R-1, 32–33	33.52	BIO	NP10	early Eocene	Smear slide	M	R	R	R				R	R	R						R		R	R	R		R
6R-3, 69–79	45.77	PAL			Smear slide																						

Notes: * = all smear slides were prepared at variable concentrations. Preservation: M = moderate, P = poor. Abundance: F = few, R = rare. PAL = paleontology. BIO = biostratigraphy.

Table T4. Distribution and lithology of basement units and subunits from Nintoku Seamount, Site 1205. (Continued on next page.)

Core, section	Unit/ Subunit	Unit name	Position of unit boundaries and comments
197-1205A-			
1R to 5R-1	SEI	Fossilferous sandstone	The base of sedimentary Unit I is inferred to be at Section 5R-1, 62 cm.
5R-2	SEII	Conglomerate	The base of sedimentary Unit II is inferred to be at the bottom of Section 5R-2.
6R-1 to 6R-2	1	Moderately to highly plagioclase-phyric basalt	The base of Unit 1 is at Section 6R-3, 74 cm.
6R-3	2	Red soil	About 7 cm of red-brown soil was recovered at the base of Section 6R-3. Large increases in the rate of penetration at this depth may indicate the presence of a soil horizon of substantial thickness. The base of Unit 2 is between Sections 6R-3 and 7R-1. Part of the soil and flow-top breccia were not recovered.
7R-1 to 7R-2	3a	Olivine-plagioclase-phyric basalt autoclastic breccia	Agglutinated autoclastic breccia from the lower part of the flow-top rubble.
7R-2 to 14R-3	3b	Sparsely to moderately olivine-plagioclase-phyric basalt	Glassy lobe margins and soil on the bottom piece of Section 14R-3 defines the base of Unit 2.
		No recovery	Part of the vitric sandstone and associated soils were not recovered.
15R-1	4	Reddish brown vitric sandstone	Laminated volcaniclastic sandstone. Unit 4 is a 0.25-m-thick interval at the top of Section 15R-1.
15R-1	5a	Red soil	Piece 3 contains ~8 cm of grayish red silty clay (soil) situated above the smooth glassy flow top of Unit 5b.
15R-1 to 17R-1	5b	Moderately plagioclase-olivine-phyric basalt	The base of Unit 5b is in Section 17R-1.
17R-1		Red soil	There is a fragment of oxidized silty clay adhering to coherent basalt in Piece 10.
17R-1 to 19R-4	6	Moderately plagioclase-olivine-phyric basalt	The upper boundary is a weathered flow top in Section 17R-1. The base of Unit 6 is at the top of Section 19R-4.
19R-4	7	Red-brown soil	Unconsolidated red-brown silty clay mixed with angular (broken by drilling) lava fragments. Large increases in the rate of penetration at this depth may indicate the presence of a soil horizon of substantial thickness. The base of Unit 7 is in Section 19R-4.
19R-4 to 21R-2	8a	Moderately plagioclase-olivine-phyric basalt	The base of Unit 8a is in Section 21R-2.
21R-2	8b	Plagioclase-olivine basalt autoclastic breccia	Basal flow rubble. The base of Unit 8b is in Section 21R-2.
22R-2		Break in lava accumulation (soil?)	The unit boundary is indicated by presence of flow-base breccia in Pieces 3–5 and traces of red oxidized clay soil in Piece 6, along with a significant change in lithology between Units 8 and 9.
21R-2 to 22R-2	9	Aphyric basalt	The base of Unit 9 is inferred to be at the top of Section 23R-2.
22R-2		Break in lava accumulation	There is a significant change in lithology between Cores 22R and 23R.
23R-1 to 25R-2	10	Sparsely plagioclase-olivine-phyric to aphyric basalt	The base of Unit 10 is at Section 25R-2, 71 cm.
25R-2	11a	Red-brown soil	Contact between Unit 11a and 11b is placed at the bottom of Section 25R-2 because the thin-bedded red-brown clay contains relict clasts that have groundmass texture similar to that of the underlying lava flow and are different from the unit above.
26R-1 to 26R-3	11b	Aphyric basalt	The base of Unit 11b is at Section 26R-3, 79 cm.
26R-3	12a	Red-brown soil	Red clay mixed with angular (broken by drilling) lava fragments represents soil produced by weathering of the underlying lava flow. The base is at Section 26R-3, 105 cm.
26R-3 to 28R-1	12b	Aphyric basalt	Highly weathered basalt is present in Piece 17. The base of Unit 12b is at Section 28R-1, 3 cm.
28R-1	13a	Red soil and weathered flow top	Piece 1B consists of dark reddish brown unconsolidated silty clay, and Piece 1C is glassy lava from the top of the underlying lava. The contact between Units 12a and 12b is placed at Section 28R-1, 10 cm.
28R-1 to 28R-4	13b	Aphyric basalt	Pieces 7–10 in Section 28R-4 consist of lapilli-size glassy and hypocrystalline scoriaceous lava clasts, which is the basal rubble to Unit 13b. The base of Unit 13b is at Section 28R-4, 85 cm.
28R-4	14a	Red soil and weathered flow top	This horizon contains soil formed by penetrative weathering of the top of the underlying lava flow. The base is at Section 28R-4, 135 cm.
28R-4 to 29R-3	14b	Sparsely to moderately plagioclase-olivine-phyric basalt	The base of Unit 14b is at Section 29R-3, 3 cm.
29R-4	15a	Red-brown soil	Piece 1 in Section 29R-4 consists of red-brown unconsolidated clay soil. The base is at Section 29R-4, 25 cm.
29R-3 to 30R-1	15b	Sparsely to moderately plagioclase-olivine-phyric basalt	Basal flow rubble is present in Piece 19. The base of Unit 15b is at Section 30R-1, 97 cm.
30R-1		Weathered flow top	Piece 20 in Section 30R-1 is a weathered pahoehoe flow top of Unit 16.
30R-1 to 32R-3	16	Sparsely to moderately plagioclase-olivine-phyric basalt	The upper boundary is a weathered flow top in Section 30R-1. Unit 16 has a smooth glassy pahoehoe base at Section 32R-3, 46 cm.
32R-3		Weathered flow top	Weathered flow top of Unit 17. Penetrative weathering of the flow top has formed a brown clay. Pieces of unaltered lava are present as 2- to 50-mm-sized fragments.
32R-3 to 33R-4	17	Sparsely to moderately plagioclase-olivine-phyric basalt	Unit 17 is a weathered flow top (Pieces 3–7). The top is at Section 32R-3, 46 cm, and the base at Section 33R-4, 25 cm.
33R-4	18a	Red soil and weathered flow top	Weathered flow top of Unit 18. Penetrative weathering of the flow top has formed a red-brown clay. Vesicular basalt lava at the top of Piece 7 in Section 33R-4 is similar to the basalt of Unit 17 and contains altered glassy lobe margins in contact with soil. 1- to 2-cm-sized fragments of highly altered aphanitic basalt (similar to those of Unit 18b) are present in the clay.
33R-4 to 35R-1	18b	Aphyric to moderately olivine-phyric basalt	The base of Unit 18b is at Section 35R-1, 55 cm.

Table T4 (continued).

Core, section	Unit/ Subunit	Unit name	Position of unit boundaries and comments
35R-1	19a	Weathered flow top	Weathered flow top of Unit 19. Penetrative weathering of the flow top has formed a brown clay. Subrounded to angular domains of olivine phyric basalt are present as 2- to 40-mm-sized fragments.
35R-1 to 35R-4	19b	Moderately to highly olivine-phyric basalt	The base of Unit 19b is at Section 35R-4, 131 cm.
35R-5 to 36R-1	19c	Olivine basalt breccia	The base of Unit 19c is at Section 36R-1, 20 cm.
36R-1		Weathered flow top	Weathered flow top of Unit 20. Penetrative weathering of the flow top is situated below the flow base rubble of Unit 19.
36R-1 to 37R-2	20	Sparsely to moderately olivine-phyric basalt	The base of Unit 20 is at Section 37R-2, 20 cm.
37R-2		Weathered flow top	Weathered flow top of Unit 20. Penetrative weathering of the flow top has formed a brown clay. Subrounded to angular centimeter-sized fragments of the underlying lava are present in the clay.
37R-2 to 38R-1	21	Moderately to highly plagioclase-olivine-phyric basalt	The base of Unit 21 is inferred to be at the top of Section 38R-1.
38R-1		Break in lava accumulation	There is a significant change in lithology between Cores 37R and 38R–40R.
38R-1 to 40R-2	22	Moderately olivine-plagioclase-phyric basalt	The base of Unit 22 is at Section 40R-2, 83 cm.
40R-2	23	Red-brown soil	This horizon is red-brown soil. The base is at Section 40R-2, 109 cm.
40R-2 to 41R-3	24a	Aphyric basalt	The base of Subunit 24a is at Section 41R-3, 73 cm.
41R-3	24b	Aphyric basalt breccia	The base of Subunit 24b is at Section 41R-3, 115 cm.
41R-3	25	Red brown soil	This horizon is a red-brown soil. The base is at Section 43R-3, 123 cm.
41R-3 to 41R-5	26a	Aphyric to sparsely plagioclase-phyric basalt	The base of Unit 26a is at Section 41R-5, 115 cm.
42R-1	26b	Aphyric basalt breccia	The base of Unit 26b is at Section 42R-1, 31 cm.
42R-2		Red soil and weathered flow top	There is 3–4 cm of red-brown soil on top of an eroded flow surface and deeply weathered flow top.
42R-1 to 43R-4	27	Aphyric to moderately plagioclase-phyric basalt	The top of Unit 27 is defined by a weathered flow top capped by 2–3 cm of soil. The base of Unit 27 is at Section 43R-4, 78 cm.
43R-4		Weathered flow top	Weathered flow top of Unit 28. Penetrative weathering of the flow top has formed a brown clay. 5- to 30-mm-sized fragments of less-altered olivine-phyric basalt are present.
43R-4 to 44R-2	28a	Moderately olivine-plagioclase-phyric basalt	The top of Unit 28 is defined by a deeply weathered flow top. The base of Unit 28 is at Section 44R-2, 66 cm.
44R-2	28b	Olivine-plagioclase basalt-breccia	Basal breccia to Unit 28a. There is 1 cm of soil attached to Piece 3. The base of Unit 28b is at Section 44R-2, 74 cm.
44R-2		Brown soil?	Soil is present on the edges of Pieces 2 and 3. Unit 28b breccia is cemented by zeolites, whereas interclast voids in Unit 29a breccia are partly filled by laminated detrital silt and clay.
44R-2	29a	Olivine basalt breccia	Flow-top breccia to Unit 29b. There is soil (2 cm) attached to top of Piece 4, and breccia is infiltrated by detrital silty clay. The base of Unit 29a is at Section 44R-2, 84 cm.
44R-2	29b	Moderately olivine-phyric basalt	The base of Unit 29b is at Section 44R-2, 134 cm.
44R-2	29c	Olivine basalt breccia	Basal breccia to Unit 29b. The base of Unit 29c is at Section 44R-2, 84 cm.
44R-2		Break in lava accumulation	Unit 29c breccia is cemented by zeolites, whereas the voids in the Unit 30a breccia are partly filled by laminated detrital silt and clay.
44R-2	30a	Olivine-plagioclase basalt breccia	Flow-top breccia to Unit 30b. The base of Unit 30a is taken to be at the top of Section 44R-3.
44R-2 to 45R2	30b	Aphyric to moderately olivine-plagioclase-phyric basalt	The base of Unit 30b is taken to be at the bottom of Section 45R-2.

Table T5. Carbon, nitrogen, and sulfur data, Site 1205A.

Core, section, interval (cm)	Depth (mbsf)	Depth in basement (m)	Basement unit/ subunit	Inorganic C (wt%)	$CaCO_3$ (wt%)	Total C (wt%)	TOC (wt%)	Nitrogen (wt%)	Sulfur (wt%)
197-1205A-									
6R-3, 70.0–71.0	45.78	3.08	2	0.01	0.12	ND	ND	ND	ND
6R-3, 72.0–73.0	45.80	3.10	2	0.01	0.10	0.05	0.04	0.003	0.000
6R-3, 75.0–76.0	45.83	3.13	2	0.00	0.04	0.04	0.03	0.002	0.000
6R-3, 79.0–80.0	45.87	3.17	2	0.01	0.07	ND	ND	ND	ND
15R-1, 19.5–20.0	90.89	48.19	5	0.01	0.07	0.04	0.03	0.002	0.000
15R-1, 21.0–21.5	90.91	48.21	5	0.01	0.09	0.02	0.01	0.002	0.000
19R-4, 19.0–20.0	114.24	71.54	7	0.01	0.05	0.03	0.02	0.002	0.000
19R-4, 23.0–24.0	114.28	71.58	7	0.01	0.07	0.02	0.02	0.001	0.000
23R-4, 83.0–84.0	143.76	101.06	10	0.01	0.07	0.06	0.05	0.001	0.000
23R-4, 88.0–89.0	143.81	101.11	10	0.01	0.05	0.08	0.08	0.006	0.000
23R-4, 95.0–96.0	143.88	101.18	10	0.01	0.05	0.13	0.12	0.001	0.000
25R-2, 60.0–61.0	159.84	117.14	11	0.01	0.05	0.06	0.05	0.001	0.000
25R-2, 65.0–66.0	159.89	117.19	11	0.00	0.03	0.05	0.05	0.001	0.000
25R-2, 70.0–71.0	159.94	117.24	11	0.00	0.03	0.06	0.05	0.002	0.000
25R-2, 72.0–73.0	159.96	117.26	11	0.00	0.03	0.07	0.06	0.000	0.000
25R-2, 75.0–76.0	159.99	117.29	11	0.01	0.06	0.05	0.04	0.000	0.000
26R-3, 72.0–72.5	171.39	128.69	12	0.01	0.06	0.06	0.06	0.004	0.000
26R-3, 72.5–73.0	171.39	128.69	12	0.01	0.06	0.04	0.03	0.002	0.000
26R-3, 79.0–79.5	171.46	128.76	12	0.01	0.05	0.05	0.04	0.003	0.000
26R-3, 86.0–86.5	171.53	128.83	12	0.01	0.07	0.06	0.05	0.005	0.000
28R-1, 9.0–9.3	186.99	144.29	13	0.01	0.06	0.04	0.04	0.003	0.000
28R-1, 9.5–9.9	186.99	144.29	13	0.01	0.06	0.03	0.02	0.003	0.000
28R-4, 77.0–77.5	191.57	148.87	14	0.01	0.06	0.02	0.01	0.002	0.000
28R-4, 91.0–91.4	191.71	149.01	14	0.01	0.05	0.02	0.02	0.004	0.000
28R-4, 123.0–123.5	192.03	149.33	14	0.01	0.07	0.03	0.02	0.004	0.000
29R-4, 6.0–6.5	200.19	157.49	15	0.01	0.08	0.02	0.01	0.002	0.000
29R-4, 9.5–9.7	200.23	157.53	15	0.01	0.04	0.02	0.01	0.001	0.000
29R-4, 11.0–11.5	200.24	157.54	15	0.01	0.05	0.03	0.03	0.002	0.000
33R-4, 37.0–38.0	229.28	186.58	18	0.01	0.09	0.09	0.08	0.004	0.000
36R-1, 10.0–11.0	254.40	211.70	20	0.00	0.03	0.10	0.10	0.002	0.654
36R-1, 12.0–13.0	254.42	211.72	20	0.00	0.04	0.08	0.08	0.003	0.303
40R-2, 89.0–90.0	277.69	234.99	23	0.01	0.06	0.11	0.11	0.006	0.000
40R-2, 108.0–109.0	277.88	235.18	23	0.01	0.06	0.09	0.08	0.006	0.000
41R-3, 118.0–119.0	286.02	243.32	25	0.01	0.08	0.06	0.05	0.002	0.000
42R-1, 2.0–3.0	292.82	250.12	26	0.00	0.04	0.06	0.06	0.000	0.000
42R-1, 12.0–13.0	292.92	250.22	26	0.01	0.10	0.04	0.03	0.001	0.000
43R-4, 148.0–149.0	307.11	264.41	28	0.01	0.06	0.05	0.05	0.001	0.000
43R-4, 149.0–150.0	307.12	264.42	28	0.01	0.05	0.06	0.05	0.002	0.000

Note: TOC = total organic carbon; ND = not detected. Organic carbon content was calculated as total carbon minus carbonate carbon by Coulometric analysis with respect to the depth of soils and baked breccia beds in Hole 1205A.

Table T6. Key structural and morphological features of the basement lava flow units, Site 1205.

Unit/ Subunit	Unit thickness (m)	Architecture	Pahoehoe		Lower vesicular crust		Lobe interior		Upper vesicular crust		Segregation structure	Breccia		Viscous flow fabric			Flow type
			Base	Top	Present	Vesicularity (modal%)	Type	Vesicularity (modal%)	Present	Vesicularity (modal%)		Top	Base	ff	pf	vf	
1	3.1	S	Y	—	Y	2–10	m	1–3	—	—	N	—	N	N	Y (ah, av, t)		Transitional
3a, b	32.9	S	Y		Y	15–20	m	1–2	N		y(sv)	Y	N	Y(ah)	—	y (ah, i)	Transitional
5b	10.8	S	—	Y	Y	5–10	v(ah, i)	1–5	N		N	N	—	Y(ah)	Y(ah)	Y(ah, i)	Transitional
6	12.4	S	—	—	y?	5	v(ah, av)	3–10	Y	3–10	y(mv, hvs)	—	—	N	Y(ah, r)	Y(ah, av, i)	Transitional
8a, b	17.1	S	N	N	N		m (ah, i)	<1–7	N		N	Y	Y	Y(ah)	Y(ah, r)	Y(ah, i)	A'a
9	3.7	L	—	—	Y	15–20	m/v(i)	3–5	Y	10–15	y(mv)	N	N	N	N		Compound pahoehoe (2 lobes)
10	24.9	L	—	Y	Y	10–25	m/v	0–15	Y	10–25	y(pv, sv, vc, mv)	N	N	N	N		Compound pahoehoe (10 lobes)
11b	11.4	S	N	N	Y	15–30	m	0–2	Y	0–15	y(vc, mv)	Y	Y	y(ah)	N		Transitional
12b	15.2	L	—	—	Y	5–15	m	<1–3	Y	10–20	y(sv, vc, mv)	N	N	N	N		Compound pahoehoe (3 lobes)
13b	4.4	S	Y	Y	Y	20–25	m	<2	Y	10–20	y(mv)	N	y	N	N		Simple pahoehoe
14b	8.1	S	—	—	Y	5	m/v	5–15	Y	10–15	N	—	—	Y(ah)	Y(ah)	y(ah, i)	Transitional
15b	6.7	L	—	—	Y	10–15	m	<1	Y	7–10	—	—	—	N	N		Compound pahoehoe (2 lobes)
16	13.7	S	Y	—	Y	10	m/v	0.5–5	Y	15–25	—	N	N	N	N		Simple pahoehoe
17	9.4	S	Y	—	Y	20–25	m	0–2	Y	10–20	y(mv, hvs)	N	N	N	N		Simple pahoehoe
18b	14.6	L	Y	Y	Y	10–25	m/v	0–10	Y	20–30	—	N	N	N	N		Compound pahoehoe (>5 lobes)
19b, c	9.0	S	N	—	N		m	0–5	N		N	—	Y	Y(ah)	N	Y(ah)	A'a
20	11.7	S	—	—	Y	5–15	m	<1–3	Y	15–40	y(mv, hvs)	—	—	N	N		Simple pahoehoe
21	7.4	S	—	—	—		m	2	Y	5–20	y(mv)	—	—	N	N		Simple pahoehoe
22	4.0	S	—	—	Y	3–5	m	<1	—	—	N	—	N	Y(ah)	N	N	Transitional
24a, b	8.1	S	N	—	N		m	1–2	N		N	—	Y	Y(ah)	N	Y(ah)	A'a
26a, b	6.6	S	N	—	Y	1–2	m	<1	N	5–15	N	—	Y	N	N	Y(ah, i)	Transitional
27	13.7	S	—	—	Y	3–5	m	<1	Y	3–15	y(mv)	—	N	Y(ah)	Y(ah)	Y(ah, i)	Transitional
28a, b	7.5	S	N	—	N	1	m	0–1	N	7–25	N	—	Y	y(ah)	—	Y(ah, i)	Transitional
29a, b, c	0.6	S	N	N	N		m/v	7	N		N	Y	Y	y(ah)	N	Y(ah)	A'a
30a, b	>9.7	S	—	N	—	—	m	0–3	N		N	Y	Not drilled	y(ah)	N	N	A'a?

Notes: S = simple flow consisting of a single lobe (flow unit), L = lobed consisting of multiple flow lobes. Y = present as a major component, — = cannot tell from the recovered core, N = not present, y = present as a minor component, m = massive (nonvesicular), v = vesicular, ah = subhorizontal, i = isotropic, av = subvertical (crystal or vesicle fabric), m/v = lava consisting of multiple lobes that have either massive or vesicular interiors. sv = segregation vesicles, mv = megavesicles, hvs = horizontal vesicle sheets (segregation veins), pv = pipe vesicles, vc = vesicle cylinders. ff = flow foliation, pf = crystal fabric (alignment of tabular and lath-shaped plagioclase phenocrysts and groundmass phases), vf = vesicle fabric: ah = aligned horizontal, r = random (isotropic), av = aligned vertical, t = trachytic texture.

Table T7. Summary of the opaque mineralogy of basement rocks, Site 1205. (See table note. Continued on next page.)

Basalt unit	Core, section, piece interval (cm)	Size (μm)	Titanomagnetite description	Estimated modal abundance (%)	Other opaque minerals	Photomicrograph
	197-1205A-					
Clast in basal conglomerate (Unit V)	5R-2 (Piece 7, 31–33)	≤100	Slight maghemite development in some crystals; most crystals are ≤50 μm	8–10	Trace of primary sulfide as minute bleb inclusions in primary minerals; secondary goethite is well developed; no sulfide	
Clast in basal conglomerate (Unit V)	5R-2 (Piece 21, 101–103)	≤100	Unaltered; most crystals are ≤10 μm	8–10	Goethite is well developed in patches; Fe oxyhydroxide is pervasive; no sulfide	1205A-182, 1205A-287
1	6R-2 (Piece 1A, 13–15)	≤100	Unaltered; rare maghemite is developed along cleavage planes and fractures; occasional ilmenite oxidation lamellae	6–8	No sulfide or Fe oxyhydroxide	
1	6R-2 (Piece 4, 55–57)	50–150	Unaltered; slight development of ilmenite oxidation lamellae; rare maghemite along cleavage planes and fractures	6–8	Goethite is well developed in patches; Fe oxyhydroxide is pervasive; no sulfide	
3b	7R-1 (Piece 17, 83–85)	≤30	Highly altered to maghemite with only a few relict cores in the larger crystals	8–10	Goethite is present; Fe oxyhydroxide is pervasive; no sulfide	
3b	8R-1 (Piece 4, 59–61)	≤80	Unaltered; most crystals are ≤10 μm; rare maghemite along cleavage planes and fractures; occasional ilmenite oxidation lamellae	10–12	Primary pentlandite as inclusions in primary minerals; trace of secondary pyrite; rare chromite(?) inclusions in olivine	1205A-192
3b	9R-2 (Piece 2A, 65–67)	≤200	Unaltered; most crystals are ≤40 μm; ilmenite oxidation lamellae are present in crystals adjacent to veins	4–6	Fe oxyhydroxide is present adjacent to veins; no sulfide	
3b	10R-2 (Piece 3E, 73–75)	≤80	Unaltered; no ilmenite oxidation lamellae or maghemite observed	12–15	No sulfide or Fe oxyhydroxide	
3b	11R-1 (Piece 2A, 73–75)	≤200	Unaltered; many crystals are ~50 μm; no ilmenite oxidation lamellae or maghemite observed	9–11	No sulfide or Fe oxyhydroxide	
3b	11R-4 (Piece 1A, 42–44)	≤150	Unaltered; rare maghemite along cleavage planes and fractures; occasional ilmenite oxidation lamellae	10–12	No sulfide or Fe oxyhydroxide	
3b	12R-2 (Piece 3A, 114–116)	~100	Unaltered; rare maghemite along cleavage planes and fractures; occasional ilmenite oxidation lamellae	10–12	No sulfide or Fe oxyhydroxide	
3b	13R-3 (Piece 1F, 27–29)	≤100	Unaltered; occasional development of ilmenite oxidation lamellae	10–12	No sulfide or Fe oxyhydroxide	1205A-226, 1205A-227
5b	15R-2 (Piece 10, 138–140)	≤150	Unaltered; occasional development of ilmenite oxidation lamellae	10–12	No sulfide or Fe oxyhydroxide	
5b	15R-3 (Piece 1B, 37–39)	≤80	Unaltered; occasional development of ilmenite oxidation lamellae	6–8	Rare pentlandite inclusions in primary minerals; secondary pyrite; no Fe oxyhydroxide	
5b	16R-2 (Piece 15, 84–86)	≤80	Unaltered; occasional development of ilmenite oxidation lamellae	8–10	No sulfide or Fe oxyhydroxide	
6	19R-2 (Piece 3, 104–106)	≤70	Unaltered; no ilmenite oxidation lamellae or maghemite observed	10–12	No sulfide or Fe oxyhydroxide	
8a	20R-5 (Piece 3, 67–68)	≤150	Unaltered; rare maghemite along cleavage planes and fractures; occasional ilmenite oxidation lamellae	10–12	Rare pentlandite inclusions in primary minerals; no Fe oxyhydroxide	
9	22R-1 (Piece 6A, 28–30)	≤200	Ilmenite oxidation lamellae are common; occasional development of maghemite along cleavage planes	9–11	No sulfide or Fe oxyhydroxide	
10	23R-1 (Piece 8, 77–78)	≤60	Unaltered; rare ilmenite oxidation lamellae, but lots of cracking along cleavage planes	2–4	No sulfide or Fe oxyhydroxide	
10	24R-2 (Piece 19, 124–130)	≤50	Extensive alteration to maghemite (~60%); relict titanomagnetite is present as lamellae parallel to cleavage planes; this is from a weathered flow top	4–6	Fe oxyhydroxide and goethite are pervasive; olivine is replaced by iddingsite or goethite; no sulfide	1205A-286
12b	27R-5 (Piece 5, 103–105)	≤150	Unaltered; occasional development of ilmenite oxidation lamellae	4–6	No sulfide or Fe oxyhydroxide	1205A-224
13b	28R-3 (Piece 1A, 4–6)	≤300	Development of ilmenite oxidation lamellae is extensive; rare maghemite along fractures and cleavage planes	4–6	Primary pentlandite as inclusions in primary minerals; trace of secondary pyrite; no Fe oxyhydroxide	

Table T7 (continued).

Basalt unit	Core, section, piece interval (cm)	Size (μm)	Titanomagnetite description	Estimated modal abundance (%)	Other opaque minerals	Photomicrograph
14b	29R-2 (Piece 7A, 55–58)	≤50	Ilmenite oxidation lamellae are common; maghemite is present along fractures and cleavage planes and as rims	9–11	No sulfide or Fe oxyhydroxide	1205A-273
15b	30R-1 (Piece 9, 42–44)	≤40	Maghemite development is extensive; relict Ti-Mag zone parallel to cleavage planes	3–5	Fe oxyhydroxide is present; no sulfide	1205A-272
16	32R-2 (Piece 2H, 114–116)	≤100	Ilmenite oxidation is extensive and not confined to lamellae; rare maghemite along fractures and cleavage planes	4–6	No sulfide or Fe oxyhydroxide	
17	33R-3 (Piece 1B, 11–13)	≤100	Development of ilmenite oxidation lamellae is extensive; maghemite along fractures and cleavage planes	5–7	No sulfide or Fe oxyhydroxide	
18b	35R-1 (Piece 1A, 32–34)	≤50	Unaltered; occasional ilmenite oxidation lamellae	2–4	Cr spinel as inclusions in olivine phenocrysts and with Ti-Mag rims; no sulfide or Fe oxyhydroxide	1205A-248, 1205A-270
19b	35R-4 (Piece 1C, 77–79)	≤100	Development of ilmenite oxidation lamellae is extensive; partially replaced by maghemite	2–4	Cr spinel as inclusions in olivine phenocrysts and with Ti-Mag rims; no sulfide or Fe oxyhydroxide	1205A-251, 1205A-268, 1205A-269, 1205A-280, 1205A-281, 1205A-282, 1205A-288
20	36R-5 (Piece 2D, 50–51)	≤80	Ilmenite oxidation is extensive and not confined to lamellae; occasional maghemite along fractures and cleavage planes	9–11	No sulfide or Fe oxyhydroxide	1205A-250, 1205A-283
21	37R-5 (Piece 2C, 28–29)	≤50	Development of ilmenite oxidation lamellae is extensive	3–5	No maghemite, sulfide, or Fe oxyhydroxide	
22	39R-1 (Piece 3F, 69–70)	≤100	Unaltered; rare maghemite along cleavage planes and fractures; occasional ilmenite oxidation lamellae	6–8	No sulfide or Fe oxyhydroxide	
24a	41R-3 (Piece 1B, 59–61)	≤70	Ilmenite oxidation is extensive and not confined to lamellae; maghemite along fractures and cleavage planes is common	4–6	No sulfide or Fe oxyhydroxide	
26a	41R-5 (Piece 1A, 24–26)	≤150	Development of ilmenite oxidation lamellae is extensive; partially replaced by maghemite along fractures, cleavage planes, and at rims	3–5	No sulfide or Fe oxyhydroxide	1205A-266, 1205A-267
27	43R-2 (Piece 2A, 58–60)	≤200	Ilmenite oxidation is extensive and not confined to lamellae; maghemite along fractures and cleavage planes is common	5–7	No sulfide or Fe oxyhydroxide	1205A-252, 1205A-253, 1205A-254
28a	44R-1 (Piece 5A, 87–88)	≤100	Most crystals ≤30 μm; development of ilmenite oxidation lamellae is extensive	12–15	No maghemite, sulfide, or Fe oxyhydroxide	1205A-284
29b	44R-2 (Piece 9, 110–112)	≤50	Ilmenite oxidation is extensive and not confined to lamellae; maghemite is present along fractures and cleavage planes	12–15	No sulfide or Fe oxyhydroxide	1205A-264, 1205A-285
30b	45R-1 (Piece 5I, 126–128)	≤100	Development of ilmenite oxidation lamellae is extensive; partially replaced by maghemite along fractures, cleavage planes, and at rims	10–12	No sulfide or Fe oxyhydroxide	1205A-265

Note: Ti-Mag = titanomagnetite.

Table T8. Major and trace element concentrations in lavas determined by ICP-AES, Hole 1205A. (Continued on next two pages.)

Core, section:	5R-2	5R-2	6R-2	8R-1	12R-2	13R-3	16R-2	19R-2	20R-5	22R-1
Interval (cm):	31–33	101–103	13–15	59–61	114–116	27–29	84–86	104–106	67–68	28–30
Piece:	7	21	1A	4	3A	2A	1J	3B	3	6A
Unit/Subunit:	Conglomerate	Conglomerate	1	3b	3b	3b	5b	6	8a	9
Rock type:	Basalt cobble boulder conglomerate	Basalt cobble boulder conglomerate	Moderately to highly plagioclase-phyric basalt	Sparsely to moderately olivine plagioclase-phyric basalt	Sparsely to moderately olivine-plagioclase-phyric basalt	Sparsely to moderately olivine-plagioclase-phyric basalt	Moderately plagioclase-olivine-phyric basalt	Moderately plagioclase-olivine-phyric basalt	Moderately plagioclase-olivine-phyric basalt	Aphyric basalt
Depth (mbsf):	34.19	34.89	43.93	57.49	73.88	78.79	97.08	112.34	125.8	133.18
Major element oxide (wt%):										
SiO_2	47.85	49.99	46.23	45.40	45.38	46.73	46.04	46.25	46.92	46.21
TiO_2	2.76	3.02	2.55	2.87	2.82	2.94	2.35	2.29	2.58	2.52
Al_2O_3	17.46	19.13	16.65	15.99	15.83	16.00	16.31	17.66	15.42	15.68
Fe_2O_3	13.22	10.90	11.64	14.47	14.48	13.68	13.59	12.52	14.88	14.13
MnO	0.15	0.10	0.15	0.20	0.20	0.18	0.18	0.16	0.20	0.17
MgO	3.24	1.59	5.03	5.52	5.33	5.26	6.10	6.08	5.30	6.45
CaO	6.36	5.57	9.78	8.20	7.89	8.15	9.71	9.42	9.09	9.41
Na_2O	4.45	4.63	3.42	3.83	3.77	3.59	3.24	3.25	3.72	3.09
K_2O	1.99	2.78	1.08	1.16	1.39	1.14	0.71	0.93	1.25	0.78
P_2O_5	0.68	0.97	0.69	0.60	0.60	0.45	0.25	0.32	0.33	0.27
Totals:	98.15	98.69	97.22	98.23	97.70	98.12	98.48	98.88	99.69	98.71
LOI	1.87	2.60	2.71	0.97	1.41	2.31	1.31	2.10	1.59	2.34
Mg#	0.35	0.24	0.49	0.46	0.45	0.46	0.50	0.52	0.44	0.50
Trace element (ppm):										
Sr	914	991	633	503	506	495	413	502	523	380
Ba	642	707	381	369	383	361	213	274	264	215
Sc	10.5	11.2	18.1	18.1	17.9	18.5	25.7	20.7	23.5	25.7
V	79.9	100	230	216	208	215	327	259	295	326
Cr	ND	ND	70.9	82.5	74.8	76.3	55.5	59.1	56.8	113
Co	45.8	58.6	58.6	54.4	52.5	50.1	54.6	60.7	66.4	59.6
Ni	4.8	5.4	65.5	42.4	36.9	41.0	46.8	44.4	26.6	52.4
Cu	26.0	17.1	55.7	41.0	33.0	32.9	63.2	46.4	53.7	99.7
Zn	107	108	119	127	130	134	169	98.5	78.7	72.1
Y	36.5	42.1	26.2	29.6	30.1	32.2	27.1	26.0	30.1	25.7
Zr	282	291	195	213	216	211	131	157	171	137

Notes: LOI = loss on ignition at 1025°C for 4 hr. Mg# = MgO/(MgO+FeO), in molar percent, with FeO calculated (as 90% of total Fe). In all figures all data are renormalized to 100% in order to correct for variable LOI. ND = not detected. This table is also available in **ASCII.**

Table T8 (continued).

Core, section:	23R-1	26R-2	27R-5	28R-3	29R-2	30R-1	32R-2	33R-3	35R-1	35R-4	36R-5
Interval (cm):	77–78	23–25	103–105	4–6	55–58	42–44	114–116	11–13	32–34	77–79	50–51
Piece:	8	1B	5	1A	7A	9	2H	1B	1A	1C	2D
Unit/Subunit:	10	11b	12b	13b	14b	15b	16	17	18b	19b	20
Rock type:	Sparsely plagioclase-olivine-phyric to aphyric basalt	Aphyric basalt	Aphyric basalt	Aphyric basalt	Sparsely to moderately plagioclase-olivine-phyric basalt	Sparsely to moderately plagioclase-olivine-phyric basalt	Sparsely to moderately plagioclase-olivine-phyric basalt	Sparsely to moderately plagioclase-olivine-phyric basalt	Aphyric to moderately olivine-phyric basalt	Moderately to highly olivine-phyric basalt	Sparsely to moderately olivine-phyric basalt
Depth (mbsf):	139.67	169.43	184.11	189.69	198.55	206.52	219.94	227.52	244.92	248.71	259.59
Major element oxide (wt%):											
SiO_2	46.45	46.85	46.53	46.60	46.36	44.69	46.70	47.44	48.67	46.31	45.91
TiO_2	2.50	2.59	2.07	2.12	2.45	2.00	1.86	2.30	1.58	1.26	2.46
Al_2O_3	15.94	15.67	15.30	14.80	16.49	16.75	16.51	16.13	16.08	14.16	14.10
Fe_2O_3	12.79	13.66	13.60	14.60	13.93	13.99	12.80	13.97	12.48	12.50	14.37
MnO	0.17	0.20	0.17	0.19	0.23	0.23	0.17	0.18	0.16	0.15	0.19
MgO	6.64	6.80	6.98	6.72	5.09	6.41	6.67	5.98	7.44	11.02	8.44
CaO	8.58	9.40	9.46	9.48	8.91	7.56	9.58	9.25	10.65	8.30	8.64
Na_2O	3.24	3.18	2.92	3.10	3.30	2.80	3.10	3.16	2.85	2.25	3.20
K_2O	0.80	0.76	0.54	0.49	0.68	0.80	0.55	0.60	0.16	0.21	0.95
P_2O_5	0.27	0.31	0.18	0.18	0.33	0.19	0.17	0.26	0.10	0.07	0.36
Totals:	97.38	99.70	97.75	98.29	97.76	95.42	98.11	99.26	100.17	96.25	98.60
LOI	2.96	2.60	2.80	1.44	2.85	4.18	3.13	2.02	2.02	5.52	2.04
Mg#	0.53	0.52	0.53	0.50	0.45	0.50	0.53	0.48	0.57	0.66	0.56
Trace element (ppm):											
Sr	368	405	329	290	335	256	606	391	332	227	555
Ba	226	235	145	138	182	151	145	202	068	061	289
Sc	24.6	25.4	25.0	27.6	23.4	27.3	22.4	23.6	27.3	24.6	24.1
V	319	350	315	349	325	279	277	328	265	232	277
Cr	73.6	138	184	65.3	68.0	176	163	123	291	627	253
Co	58.5	53.9	62.7	64.3	57.6	55.7	53.9	59.6	53.2	68.9	64.1
Ni	39.8	73.3	93.2	41.4	31.5	92.7	87.5	67.8	105.2	413.1	243.7
Cu	63.3	57.5	67.2	77.0	44.0	40.3	58.1	60.2	69.5	58.4	63.4
Zn	101	81.6	86.9	73.7	81.3	114	50.5	130	35.0	87.0	82.9
Y	28.3	26.4	22.1	27.0	27.9	25.0	21.4	25.5	20.5	19.2	26.3
Zr	144	136	110	105	133	105	97.6	132	78.9	58.1	156

Table T8 (continued).

Core, section:	37R-5	39R-1	41R-3	41R-5	43R-2	44R-1	44R-2	45R-1
Interval (cm):	28–29	69–70	59–61	24–26	58–60	87–88	110–112	126–128
Piece:	2C	3F	1B	1A	2A	5A	9	5I
Unit:	21	22	24a	26a	27	28a	29a	30b
Rock type:	Moderately to highly plagioclase-olivine-phyric basalt	Moderately olivine-plagioclase-phyric basalt	Aphyric basalt	Aphyric to sparsely plagioclase-phyric basalt	Aphyric to moderately plagioclase-phyric basalt	Moderately olivine-plagioclase-phyric basalt	Olivine basalt breccia	Aphyric to moderately olivine-plagioclase-phyric basalt
Depth (mbsf):	269.92	275.29	285.43	287.82	303.88	313.07	314.3	322.76
Major element oxide (wt%):								
SiO_2	46.16	46.53	47.35	46.58	48.77	46.54	44.82	46.37
TiO_2	2.66	2.55	2.74	2.61	2.64	3.12	3.13	3.05
Al_2O_3	15.04	14.97	15.77	15.68	15.84	16.43	16.47	16.18
Fe_2O_3	14.32	14.30	13.25	14.39	13.59	14.45	15.17	14.53
MnO	0.18	0.17	0.16	0.21	0.19	0.27	0.24	0.19
MgO	7.34	8.17	5.42	6.30	5.81	4.84	5.44	5.09
CaO	8.74	9.01	9.31	8.39	8.99	8.29	7.38	8.15
Na_2O	3.12	3.08	3.31	3.08	3.46	3.36	3.16	3.36
K_2O	0.90	0.81	0.72	0.61	0.73	0.87	0.88	0.82
P_2O_5	0.43	0.44	0.44	0.34	0.35	0.43	0.39	0.42
Totals:	98.89	100.03	98.46	98.18	100.38	98.60	97.08	98.15
LOI	1.38	0.46	3.23	2.89	1.81	2.51	4.06	2.53
Mg#	0.53	0.56	0.47	0.49	0.48	0.42	0.44	0.44
Trace element (ppm):								
Sr	578	788	366	334	358	375	344	390
Ba	304	316	235	200	207	243	239	246
Sc	21.6	23.8	26.1	25.2	24.8	25.0	24.8	24.0
V	288	290	330	322	322	324	332	315
Cr	226	221	98.0	75.3	81.2	66.5	72.6	66.5
Co	70.2	79.6	59.4	66.5	68.2	61.8	71.0	63.7
Ni	145.5	189.7	74.6	66.8	69.8	54.7	48.0	54.5
Cu	54.6	77.7	45.1	26.9	49.6	50.1	36.8	43.9
Zn	140	141	144	147	148	173	161	163
Y	25.4	27.4	33.1	30.5	31.0	35.8	34.6	35.8
Zr	183	179	180	159	150	193	190	204

Table T9. Summary of rock magnetic parameters for basalt samples, Site 1205.

Core, section, interval (cm)	H_{cr} (mT)	MDF_{ARM} (mT)	MDF_{SIRM} (mT)	MDF_{NRM} (mT)	Basement unit/subunit
197-1205A-					
6R-1, 21	31.2	22.6	16.2	33.9	1
41R-4, 27	7.1	7.4	5.7	18.8	1
40R-3, 32	20.5	11.2	15.8	23.5	1
7R-1, 100*	13.2	15.4	10.6	13.8	3a
18R-1, 12	3.8	2.3	3.5	4.3	3b
19R-9, 98	6.5	4.7	4.6	8.7	3b
12R-2, 135	4.5	1.8	3.3	18.9	3b
14R-2, 16	3.2	2.3	2.4	3.7	3b
15R-1, 90	39.0	20.8	18.1	34.3	5b
16R-3, 34	7.7	2.2	4.2	4.4	5b
17R-1, 56	29.5	9.3	14.6	28.7	5b
19R-4, 83	26.7	18.9	13.7	31.0	8a
19R-4, 143	8.8	4.3	5.0	4.2	8a
20R-6, 12	6.4	1.9	4.1	39.8	8a
21R-2, 67	62.3	40.4	25.4	46.4	9
23R-1, 35	36.0	25.4	17.6	29.6	10
24R-2, 141	40.4	27.8	19.9	32.7	10
26R-1, 143	9.9	7.6	6.2	18.4	11b
27R-4, 44	39.4	27.2	20.8	33.8	12b
29R-3, 114	48.0	32.6	27.7	34.6	14b
35R-2, 36	28.7	20.3	16.1	30.3	19b
41R-5, 91	33.6	27.1	16.4	27.8	26a
42R-1, 113	18.7	22.1	12.5	30.8	27

Notes: * = unoriented sample. H_{cr} = coercive field, MDF = median destructive field, ARM = anyhsteretic remanent magnetization, SIRM = saturation isothermal remanent magnetization, NRM = natural remanent magnetization.

Table T10. Shipboard characteristic remanent magnetization inclination averages and summary statistics based on principal component analyses of alternating-field demagnetization data, Site 1205.

Basalt unit/subunit	*N*	Point inc (°)	Inc_{95} (°)	*k*
1	3	–72.0	17.5	139
3	19	–29.5	2.3	191
5b	8	–18.1	2.8	414
6	8	–43.8	14.3	17
8	9	–35.1	3.3	258
9	4	–29.6	9.1	172
10	13	–42.4	6.3	42
11b	4	–47.5	2.5	2245
12b	7	–62.9	12.9	26
13b	4	–43.3	7.0	290
14b	3	–50.8	13.9	221
15b, 16, 17	14	–74.0	6.7	39
18b	7	–69.0	6.6	96
19b	5	–64.9	8.5	111
20	7	–27.0	5.3	149
21	3	–25.9	10.6	373
22	3	–29.1	12.9	255
24a	4	–46.0	8.6	193
26a	4	–45.3	7.6	251
27	10	–55.4	3.6	180
28a	3	–40.9	9.0	519
29b	1	–35.1	—	—
30b	1	–38.4	—	—
Average:	22	–45.7	8.4	14

Notes: Estimate of dispersion (*S*), based on the transformation of Cox (1970) = 20.4°. *N* = number of determinations within each unit. Point inc = estimation of the inclination mean based on the averaging method of McFadden and Reid (1982). Inc_{95} = estimation of 95% confidence interval of inclination. *k* = estimate of precision parameter. — = not applicable. *N* for "Average" values is the estimated number of independent time units (see text).

Table T11. Magnetic susceptibility measurements, Site 1205.

Core, section, interval (cm)	Depth (mbsf)	Magnetic susceptibility (10^{-6} SI)	Corrected susceptibility (10^{-6} SI)
197-1205A-			
4R-1, 5	23.75	708.0	708.02
4R-1, 10	23.80	603.4	603.44
4R-1, 15	23.85	877.8	877.86
4R-1, 20	23.90	930.8	930.88
4R-1, 25	23.95	760.6	760.69
4R-1, 30	24.00	663.6	663.71
4R-1, 35	24.05	691.4	691.53
4R-1, 40	24.10	651.2	651.35
4R-1, 45	24.15	593.8	593.96
4R-1, 50	24.20	473.6	473.78
4R-1, 55	24.25	978.6	978.80
4R-1, 60	24.30	1087.6	1087.83
4R-1, 65	24.35	938.0	938.26
4R-1, 70	24.40	800.6	800.89
4R-1, 75	24.45	1026.8	1027.12
4R-1, 80	24.50	1188.4	1188.76
4R-1, 85	24.55	1302.6	1302.99
4R-1, 90	24.60	1208.8	1209.22
4R-1, 95	24.65	1308.2	1308.65
4R-1, 100	24.70	1314.2	1314.68
4R-1, 105	24.75	1549.4	1549.92
5R-1, 5	33.25	462.8	462.82
5R-1, 10	33.30	462.6	462.63
5R-1, 15	33.35	786.8	786.84
5R-1, 20	33.40	1058.6	1058.66
5R-1, 25	33.45	945.0	945.07
5R-1, 30	33.50	767.0	767.08
5R-1, 35	33.55	723.6	723.70
5R-1, 40	33.60	846.2	846.31
5R-1, 45	33.65	1035.2	1035.32
5R-1, 50	33.70	1047.8	1047.94
5R-1, 55	33.75	1094.0	1094.15
5R-1, 60	33.80	796.8	796.98
5R-1, 65	33.85	328.6	328.80

Note: This table is also available in **ASCII.**

Table T12. GRA bulk density measurements, Site 1205.

Core, section, interval (cm)	Depth (mbsf)	Density (g/cm^3)
197-1205A-		
4R-1, 5	23.75	1.594
4R-1, 10	23.80	1.280
4R-1, 15	23.85	1.708
4R-1, 20	23.90	1.624
4R-1, 25	23.95	1.289
4R-1, 30	24.00	1.688
4R-1, 35	24.05	1.618
4R-1, 40	24.10	1.834
4R-1, 45	24.15	1.301
4R-1, 50	24.20	0.641
4R-1, 55	24.25	1.636
4R-1, 60	24.30	1.744
4R-1, 65	24.35	1.740
4R-1, 70	24.40	1.040
4R-1, 75	24.45	1.799
4R-1, 80	24.50	1.908
4R-1, 85	24.55	1.863
4R-1, 90	24.60	2.030
4R-1, 95	24.65	1.873
4R-1, 100	24.70	2.075
4R-1, 105	24.75	1.972
5R-1, 5	33.25	–0.386
5R-1, 10	33.30	2.295
5R-1, 15	33.35	1.787
5R-1, 20	33.40	2.035
5R-1, 25	33.45	1.273
5R-1, 30	33.50	0.497
5R-1, 35	33.55	1.407
5R-1, 40	33.60	1.890
5R-1, 45	33.65	2.065
5R-1, 50	33.70	1.808
5R-1, 55	33.75	2.019
5R-1, 60	33.80	0.749
5R-1, 65	33.85	–0.768

Note: This table is also available in **ASCII.**

Table T13. Natural gamma ray measurements, Site 1205.

Core, section, interval (cm)	Depth (mbsf)	Corrected counts (cps)	Total counts (cps)
197-1205A-			
4R-1, 10	23.80	4.03	19.90
4R-1, 20	23.90	4.68	20.55
4R-1, 30	24.00	3.88	19.75
4R-1, 40	24.10	1.38	17.25
4R-1, 50	24.20	2.63	18.50
4R-1, 60	24.30	3.88	19.75
4R-1, 70	24.40	2.63	18.50
4R-1, 80	24.50	5.78	21.65
4R-1, 90	24.60	8.38	24.25
4R-1, 100	24.70	8.93	24.80
5R-1, 10	33.30	1.08	16.95
5R-1, 20	33.40	4.53	20.40
5R-1, 30	33.50	1.38	17.25
5R-1, 40	33.60	5.98	21.85
5R-1, 50	33.70	7.68	23.55
5R-1, 60	33.80	10.38	26.25
5R-2, 60	34.48	2.16	18.03
5R-2, 70	34.58	2.58	18.45
5R-2, 80	34.68	6.13	22.00
5R-2, 100	34.88	16.28	32.15
5R-2, 120	35.08	6.35	22.22
6R-1, 10	42.80	13.06	28.93
6R-1, 20	42.90	17.41	33.28
6R-1, 30	43.00	17.43	33.30
6R-1, 50	43.20	16.31	32.18
6R-1, 100	43.70	18.35	34.22
6R-2, 10	43.90	14.53	30.40
6R-2, 20	44.00	14.56	30.43
6R-2, 30	44.10	13.00	28.87
6R-2, 40	44.20	11.31	27.18
6R-2, 50	44.30	12.00	27.87
6R-2, 60	44.40	13.83	29.70
6R-2, 70	44.50	15.83	31.70
6R-2, 80	44.60	18.15	34.02
6R-2, 90	44.70	15.86	31.73
6R-2, 100	44.80	17.05	32.92
6R-2, 110	44.90	17.65	33.52
6R-2, 120	45.00	21.16	37.03
6R-3, 10	45.18	19.60	35.47
6R-3, 30	45.38	13.15	29.02
6R-3, 40	45.48	12.66	28.53
6R-3, 50	45.58	11.53	27.40
6R-3, 60	45.68	11.28	27.15
6R-3, 80	45.88	7.91	23.78
7R-1, 40	52.60	7.95	23.82
7R-1, 90	53.10	12.38	28.25
7R-1, 130	53.50	11.01	26.88
7R-2, 10	53.72	9.95	25.82
7R-2, 20	53.82	9.65	25.52
7R-2, 40	54.02	19.10	34.97
8R-1, 10	57.00	12.70	28.57
8R-1, 20	57.10	16.81	32.68
8R-1, 30	57.20	17.10	32.97
8R-1, 40	57.30	7.98	23.85
8R-1, 50	57.40	11.70	27.57
8R-1, 70	57.60	15.16	31.03
8R-1, 80	57.70	17.20	33.07
8R-1, 90	57.80	15.05	30.92
8R-1, 100	57.90	16.70	32.57
8R-1, 110	58.00	15.28	31.15
8R-1, 120	58.10	16.75	32.62
8R-2, 10	58.34	14.71	30.58
8R-2, 30	58.54	14.26	30.13
8R-2, 40	58.64	16.13	32.00
8R-2, 50	58.74	15.10	30.97
8R-2, 60	58.84	16.41	32.28
8R-2, 70	58.94	15.25	31.12
8R-2, 80	59.04	14.13	30.00
9R-1, 10	59.00	9.03	24.90
9R-1, 20	59.10	16.90	32.77
9R-1, 30	59.20	12.68	28.55
9R-1, 40	59.30	11.53	27.40
9R-1, 50	59.40	15.63	31.50
9R-1, 60	59.50	14.68	30.55
9R-1, 70	59.60	14.88	30.75
9R-1, 80	59.70	16.43	32.30
9R-1, 90	59.80	18.91	34.78
9R-1, 100	59.90	23.30	39.17
9R-2, 10	60.06	16.13	32.00
9R-2, 20	60.16	16.46	32.33
9R-2, 30	60.26	15.28	31.15
9R-2, 40	60.36	16.26	32.13
9R-2, 50	60.46	16.08	31.95
9R-2, 80	60.76	15.30	31.17
9R-2, 90	60.86	18.36	34.23
9R-2, 100	60.96	20.80	36.67
9R-2, 110	61.06	8.20	24.07
10R-1, 20	61.90	12.21	28.08
10R-1, 30	62.00	15.96	31.83
10R-1, 40	62.10	13.46	29.33
10R-1, 50	62.20	15.83	31.70
10R-1, 60	62.30	11.46	27.33
10R-1, 70	62.40	13.65	29.52
10R-1, 80	62.50	15.06	30.93
10R-1, 90	62.60	15.76	31.63
10R-1, 110	62.80	15.20	31.07
10R-1, 120	62.90	14.93	30.80
10R-1, 130	63.00	13.76	29.63
10R-2, 10	63.22	15.16	31.03
10R-2, 20	63.32	13.10	28.97
10R-2, 30	63.42	14.73	30.60
10R-2, 40	63.52	12.83	28.70
10R-2, 50	63.62	15.06	30.93
10R-2, 60	63.72	14.70	30.57
10R-2, 70	63.82	16.55	32.42
10R-2, 80	63.92	17.05	32.92
10R-2, 90	64.02	15.05	30.92
10R-2, 110	64.22	11.80	27.67
10R-2, 120	64.32	13.50	29.37
10R-2, 130	64.42	16.25	32.12
10R-3, 10	64.60	15.45	31.32
10R-3, 30	64.80	14.88	30.75
10R-3, 40	64.90	15.90	31.77
10R-3, 50	65.00	14.21	30.08
10R-3, 60	65.10	15.86	31.73
10R-3, 70	65.20	14.03	29.90
10R-3, 80	65.30	16.18	32.05
10R-3, 90	65.40	15.96	31.83
10R-3, 100	65.50	14.66	30.53
10R-3, 110	65.60	15.51	31.38
10R-3, 130	65.80	15.00	30.87
10R-4, 10	66.10	14.80	30.67
10R-4, 20	66.20	15.36	31.23
10R-4, 30	66.30	18.78	34.65
11R-1, 10	66.30	14.93	30.80
11R-1, 20	66.40	16.30	32.17
11R-1, 30	66.50	14.98	30.85
11R-1, 40	66.60	15.66	31.53
11R-1, 50	66.70	15.85	31.72
11R-1, 60	66.80	13.21	29.08
11R-1, 70	66.90	12.78	28.65
11R-1, 80	67.00	15.13	31.00
11R-1, 90	67.10	15.66	31.53
11R-1, 100	67.20	15.86	31.73
11R-1, 110	67.30	11.91	27.78
11R-1, 120	67.40	15.63	31.50
11R-1, 130	67.50	16.55	32.42
11R-1, 140	67.60	13.28	29.15
11R-2, 10	67.75	9.73	25.60
11R-2, 20	67.85	9.25	25.12
11R-2, 40	68.05	7.21	23.08
11R-2, 50	68.15	15.38	31.25
11R-2, 60	68.25	14.16	30.03
11R-2, 70	68.35	9.73	25.60
11R-2, 80	68.45	14.93	30.80
11R-2, 90	68.55	11.43	27.30
11R-2, 100	68.65	15.95	31.82
11R-2, 110	68.75	16.10	31.97
11R-2, 120	68.85	20.66	36.53
11R-3, 10	69.03	13.26	29.13
11R-3, 20	69.13	15.51	31.38
11R-3, 30	69.23	15.05	30.92
11R-3, 40	69.33	15.23	31.10
11R-3, 50	69.43	14.41	30.28
11R-3, 60	69.53	14.53	30.40
11R-3, 70	69.63	15.08	30.95
11R-3, 80	69.73	14.88	30.75
11R-3, 90	69.83	13.85	29.72
11R-3, 100	69.93	21.21	37.08
11R-3, 110	70.03	16.63	32.50
11R-4, 10	70.15	14.76	30.63
11R-4, 20	70.25	15.03	30.90
11R-4, 30	70.35	15.10	30.97
11R-4, 40	70.45	12.88	28.75
11R-4, 50	70.55	14.76	30.63
11R-4, 60	70.65	13.81	29.68
11R-4, 70	70.75	16.75	32.62
11R-4, 80	70.85	14.50	30.37
11R-4, 90	70.95	14.61	30.48
11R-4, 100	71.05	17.83	33.70
11R-4, 110	71.15	15.73	31.60
11R-4, 120	71.25	17.01	32.88
11R-4, 130	71.35	18.03	33.90
12R-1, 10	71.40	12.98	28.85
12R-1, 20	71.50	16.31	32.18
12R-1, 30	71.60	12.53	28.40
12R-1, 40	71.70	15.95	31.82
12R-1, 50	71.80	16.05	31.92
12R-1, 60	71.90	15.78	31.65
12R-1, 70	72.00	15.13	31.00
12R-1, 80	72.10	16.71	32.58
12R-1, 100	72.30	13.85	29.72
12R-1, 110	72.40	15.55	31.42
12R-1, 120	72.50	14.85	30.72
12R-1, 130	72.60	16.78	32.65
12R-2, 10	72.84	14.16	30.03
12R-2, 20	72.94	15.51	31.38
12R-2, 30	73.04	15.85	31.72
12R-2, 40	73.14	13.55	29.42
12R-2, 50	73.24	14.88	30.75
12R-2, 60	73.34	16.15	32.02
12R-2, 70	73.44	15.75	31.62
12R-2, 80	73.54	14.05	29.92
12R-2, 90	73.64	17.83	33.70
12R-2, 100	73.74	18.00	33.87
12R-2, 110	73.84	17.51	33.38
12R-2, 120	73.94	16.00	31.87
12R-2, 130	74.04	14.35	30.22
12R-3, 10	74.34	16.25	32.12

Note: Only a portion of this table appears here. The complete table is available in **ASCII.**

Table T14. Thermal conductivity measurements, Site 1205.

Core, section, interval (cm)	Depth (mbsf)	Thermal conductivity (W/[m·K])
197-1205A-		
5R-2, 95–105	34.83	1.331
6R-2, 0–24	43.80	1.631
7R-2, 19–30	53.81	1.562
8R-1, 61–79	57.51	1.766
9R-2, 96–108	60.92	1.667
10R-2, 72–80	63.84	1.783
11R-2, 102–114	68.67	1.635
12R-2, 0–15	72.74	1.702
13R-2, 74–93	77.86	1.730
14R-1, 48–59	81.48	1.985
15R-2, 119–132	93.31	1.725
16R-3, 20–32	97.88	1.774
17R-1, 18–32	100.48	1.745
18R-3, 90–104	106.89	1.652
19R-2, 46–60	111.76	1.618
20R-5, 47–61	125.60	1.788
21R-3, 46–68	132.58	1.677
22R-1, 33–52	133.23	1.633
23R-4, 0–14	142.93	1.523
24R-4, 28–42	153.28	1.637
25R-1, 0–11	158.00	1.823
26R-2, 42–62	169.62	1.685
27R-5, 92–106	184.00	1.657
28R-2, 83–100	189.17	1.832
29R-3, 108–122	199.99	1.631
30R-3, 0–17	208.98	1.651
31R-1, 21–41	216.01	1.818
32R-3, 16–30	220.46	1.650
33R-2, 105–117	226.96	1.639
34R-3, 130–145	238.80	1.515
35R-2, 41–56	246.26	1.642
36R-5, 130–149	260.39	1.848
37R-4, 80–96	268.94	1.580
38R-1, 0–8	273.60	1.774
39R-1, 44–60	275.04	1.891
40R-1, 36–46	275.96	1.814
41R-3, 40–67	285.24	1.610
42R-3, 79–96	296.53	1.608
43R-3, 18–34	304.62	1.703
44R-1, 36–57	312.56	1.563
45R-1, 129–144	322.79	1.727

Note: This table is also available in **ASCII.**

Table T15. Index properties, Site 1205.

Core, section, interval (cm)	Depth (mbsf)	Water content (%)		Density (g/cm^3)			Porosity (%)	Void ratio
		Bulk	Dry	Bulk	Dry	Grain		
197-1205A-								
2R-1, 16–18	4.76	17.5	21.2	2.14	1.76	2.78	36.6	0.58
2R-1, 27–29	4.87	16.4	19.6	2.19	1.83	2.83	35.2	0.54
4R-1, 80–82	24.50	39.9	66.3	1.65	0.99	2.78	64.2	1.80
5R-1, 31–33	33.51	35.4	54.8	1.74	1.12	2.80	60.0	1.50
5R-2, 124–126	35.12	6.2	6.6	2.58	2.42	2.87	15.5	0.18
6R-2, 13–15	43.93	3.1	3.2	2.79	2.70	2.95	8.4	0.09
6R-3, 11–13	45.19	9.2	10.1	2.53	2.30	2.97	22.6	0.29
7R-2, 42–44	54.04	0.7	0.7	2.91	2.89	2.95	1.9	0.02
8R-1, 74–76	57.64	0.4	0.4	3.00	2.98	3.02	1.2	0.01
9R-1, 39–41	59.29	0.8	0.8	2.90	2.88	2.95	2.3	0.02
10R-2, 77–79	63.89	1.0	1.0	2.91	2.88	2.96	2.8	0.03
11R-3, 38–40	69.31	1.5	1.5	2.93	2.88	3.02	4.4	0.05
12R-2, 135–137	74.09	1.2	1.2	2.91	2.88	2.98	3.3	0.03
13R-3, 29–31	78.81	1.0	1.0	2.90	2.87	2.95	2.8	0.03
14R-2, 16–18	82.66	0.0	0.0	3.06	3.06	3.06	0.0	0.00
15R-2, 28–30	92.40	0.8	0.9	2.91	2.89	2.96	2.4	0.03
16R-2, 113–115	97.37	1.1	1.2	2.94	2.90	3.00	3.3	0.03
17R-1, 56–58	100.86	0.9	0.9	2.91	2.88	2.96	2.6	0.03
18R-1, 130–132	105.10	3.7	3.8	2.75	2.65	2.94	10.0	0.11
19R-2, 71–73	112.01	0.8	0.8	2.92	2.90	2.96	2.3	0.02
20R-5, 56–58	125.69	0.6	0.6	2.96	2.95	3.00	1.7	0.02
21R-2, 67–69	131.34	4.9	5.2	0.95	0.90	0.94	4.6	0.05
22R-1, 90–92	133.80	–2.1	2.2	2.86	2.80	2.97	–6.0	–0.06
23R-4, 11–13	143.04	3.3	3.4	2.89	2.80	3.08	9.2	0.10
24R-3, 68–70	152.18	6.1	6.5	2.71	2.55	3.04	16.2	0.19
25R-1, 55–57	158.55	2.5	2.6	2.76	2.68	2.88	6.8	0.07
26R-2, 47–49	169.67	2.2	2.2	2.86	2.79	2.97	6.1	0.06
26R-3, 64–74	171.31	33.9	51.2	1.82	1.20	3.01	60.0	1.50
27R-3, 121–123	181.29	5.5	5.8	2.71	2.57	3.00	14.5	0.17
28R-3, 5–7	189.70	1.5	1.5	2.89	2.84	2.97	4.2	0.04
29R-1, 116–118	197.66	3.3	3.5	2.81	2.71	2.99	9.2	0.10
30R-3, 71–73	209.69	2.0	2.1	2.92	2.86	3.04	5.8	0.06
31R-1, 14–21	215.94	5.0	5.2	2.64	2.51	2.88	12.8	0.15
32R-3, 25–27	220.55	2.3	2.3	2.78	2.71	2.89	6.2	0.07
33R-1, 36–38	225.76	2.5	2.6	2.80	2.72	2.93	6.9	0.08
34R-1, 43–45	235.43	9.0	9.9	2.52	2.29	2.94	22.1	0.28
35R-1, 33–35	244.93	4.1	4.3	2.75	2.63	2.96	11.1	0.12
36R-4, 122–124	258.81	2.2	2.3	2.74	2.68	2.85	6.0	0.06
37R-4, 40–42	268.54	3.1	3.2	2.79	2.70	2.95	8.5	0.09
39R-1, 70–72	275.30	1.9	1.9	2.92	2.86	3.03	5.4	0.06
40R-1, 43–45	276.03	1.9	1.9	2.78	2.73	2.88	5.1	0.05
41R-5, 91–93	288.49	5.0	5.3	2.74	2.60	3.00	13.4	0.15
42R-3, 70–72	296.44	0.6	0.7	2.96	2.94	2.99	1.9	0.02
43R-2, 62–64	303.92	2.3	2.3	2.90	2.83	3.03	6.4	0.07

Note: This table is also available in **ASCII.**

Table T16. Compressional wave velocity measurements, Site 1205.

Core, section interval (cm)	Depth (mbsf)	Direction	Velocity (m/s)
197-1205A-			
2R-1, 3.5	4.64	x	2328.4
2R-1, 30	4.90	x	2710.5
4R-1, 58	24.28	x	1774.3
5R-1, 49	33.69	x	2475.0
6R-1, 22	42.92	x	3784.4
6R-2, 14	43.94	x	5080.7
6R-2, 14	43.94	x	5141.1
6R-2, 14	43.94	z	5008.2
6R-3, 11	45.19	x	4048.9
6R-3, 11	45.19	x	4004.5
6R-3, 11	45.19	x	4068.8
6R-3, 11	45.19	z	4167.9
7R-1, 98.5	53.19	x	5746.7
7R-2, 44	54.06	x	5833.0
7R-2, 44	54.06	z	5795.4
8R-1, 76	57.66	x	5662.8
8R-1, 76	57.66	x	5953.6
8R-1, 76	57.66	z	6191.7
8R-2, 50	58.74	x	5683.0
8R-2, 50	58.74	x	5865.7
8R-2, 50	58.74	z	5943.2
9R-1, 40	59.30	x	5551.2
9R-1, 40	59.30	x	5452.4
9R-1, 40	59.30	z	5705.5
9R-2, 83	60.79	x	5041.6
9R-2, 83	60.79	x	5106.4
9R-2, 83	60.79	z	5521.5
10R-1, 55	62.25	x	5577.7
10R-1, 55	62.25	z	5601.4
10R-1, 55	62.25	y	5505.5
10R-3, 29	64.79	x	5418.8
10R-3, 29	64.79	z	5432.1
10R-3, 29	64.79	y	5445.2
10R-4, 25	66.25	x	5074.0
10R-4, 25	66.25	z	5280.2
10R-4, 25	66.25	y	5348.4
11R-1, 115	67.35	x	5160.5
11R-1, 115	67.35	z	5167.1
11R-1, 115	67.35	y	5256.6
11R-2, 65	68.30	x	5002.0
11R-2, 65	68.30	x	5164.6
11R-2, 65	68.30	z	5038.7
11R-3, 39	69.32	x	5078.9
11R-3, 39	69.32	x	4999.6
11R-3, 39	69.32	x	5044.3
11R-3, 39	69.32	z	5205.6
11R-3, 39	69.32	y	5252.8
11R-4, 45	70.50	x	5279.9
11R-4, 45	70.50	x	5168.8
11R-4, 45	70.50	z	5035.9
11R-4, 45	70.50	y	5106.4
12R-1, 94	72.24	x	5168.8
12R-1, 94	72.24	x	5308.3
12R-1, 94	72.24	z	5334.3
12R-1, 94	72.24	y	5465.0
12R-2, 136	74.10	x	5634.9
12R-2, 136	74.10	x	5843.1
12R-2, 136	74.10	z	5650.3
12R-2, 136	74.10	y	5594.1
12R-3, 99	75.23	x	5423.6
12R-3, 99	75.23	x	5449.9
12R-3, 99	75.23	z	5475.2
12R-3, 99	75.23	y	5710.4
13R-1, 37	76.47	x	5608.8
13R-1, 37	76.47	z	5716.0
13R-2, 40	77.52	x	5691.9
13R-2, 40	77.52	z	5893.3
13R-3, 30	78.82	x	5708.5
13R-3, 30	78.82	z	5696.8
13R-4, 37	80.22	x	5584.8
13R-4, 37	80.22	z	5751.1
14R-1, 56	81.56	x	5606.1
14R-1, 56	81.56	z	5925.9
14R-2, 17	82.67	x	5677.8
14R-2, 17	82.67	z	5874.7
15R-1, 91	91.61	x	5241.2
15R-1, 91	91.61	z	5191.8
15R-2, 29	92.41	x	5346.4
15R-2, 29	92.41	z	5595.6
15R-3, 64	94.19	x	5632.9
15R-3, 64	94.19	z	5621.1
16R-1, 74	95.74	x	5341.7
16R-1, 74	95.74	z	5694.7
16R-2, 104	97.28	x	5554.9
16R-2, 104	97.28	z	5418.8
16R-3, 35	98.03	x	5228.7
16R-3, 35	98.03	z	5613.8
16R-4, 107	100.25	x	5399.9
16R-4, 107	100.25	z	5653.6
17R-1, 57	100.87	x	5394.6
17R-1, 57	100.87	z	5442.1
18R-1, 130	105.10	x	4973.4
18R-1, 130	105.10	z	4637.9
18R-2, 62	105.92	x	5132.8
18R-2, 62	105.92	z	5181.3
18R-3, 97	106.96	x	5179.3
18R-3, 97	106.96	z	5293.3
19R-2, 71	112.01	x	5715.5
19R-2, 71	112.01	z	5576.0
19R-3, 99	113.54	x	5819.2
19R-3, 99	113.54	z	5759.5
19R-4, 144	115.49	x	5441.4
19R-4, 144	115.49	z	5424.5
20R-1, 97	120.57	x	5292.7
20R-1, 97	120.57	z	5225.3
20R-2, 78	121.88	x	4817.6
20R-2, 78	121.88	z	4884.1
20R-3, 61	122.95	x	5181.2
20R-3, 61	122.95	z	5314.6
20R-4, 99	124.79	x	5288.2
20R-4, 99	124.79	z	5480.3
20R-5, 56	125.69	x	5893.1
20R-5, 56	125.69	z	5700.3
20R-6, 12	126.69	x	5568.7
20R-6, 12	126.69	z	5821.9
20R-7, 31	128.14	x	5632.3
20R-7, 31	128.14	z	5441.1
21R-1, 39	129.59	x	5321.6
21R-1, 39	129.59	z	5493.3
21R-2, 67	131.34	x	4501.1
21R-2, 67	131.34	z	4641.9
21R-3, 43	132.55	x	5081.5
21R-3, 43	132.55	z	4774.6
22R-1, 15	133.05	x	5482.4
22R-1, 91	133.81	x	5091.2
22R-1, 15	133.05	z	5610.8
22R-1, 91	133.81	z	5124.8
23R-1, 36	139.26	x	4352.4
23R-1, 107	139.97	x	4756.0
23R-1, 36	139.26	z	4144.9
23R-1, 107	139.97	z	4784.2
23R-2, 104	141.44	x	4846.4
23R-2, 104	141.44	z	4836.6
23R-3, 39	141.89	x	4808.3
23R-3, 68	142.18	x	4367.6
23R-3, 39	141.89	z	4875.6
23R-3, 68	142.18	z	4881.0
23R-4, 11	143.04	x	4844.4
23R-4, 45	143.38	x	4276.1
23R-4, 11	143.04	z	4763.3
23R-5, 91	145.34	x	4082.0
23R-5, 91	145.34	z	3994.6
23R-6, 24	146.08	x	4119.3
23R-6, 24	146.08	z	3990.4
24R-1, 64	149.14	x	4947.7
24R-1, 64	149.14	z	5013.9
24R-2, 141	151.41	x	3424.6
24R-2, 141	151.41	z	3249.4
24R-3, 68	152.18	x	4699.4
24R-3, 68	152.18	z	4771.6
24R-4, 32	153.32	x	5228.4
24R-4, 32	153.32	z	5234.6
24R-5, 63	155.01	x	5056.8
24R-5, 63	155.01	z	5131.8
25R-1, 55	158.55	x	5008.1
25R-1, 55	158.55	z	5024.7
25R-2, 17	159.41	x	4700.6
25R-2, 17	159.41	z	4660.9
26R-1, 143	169.13	x	4988.7
26R-1, 143	169.13	z	5120.6
26R-2, 138	170.58	x	4959.0
26R-2, 138	170.58	z	4912.4
26R-3, 145	172.12	x	5152.9
26R-3, 145	172.12	z	5149.3
26R-4, 14	172.31	x	4236.0
26R-4, 14	172.31	z	4186.1
27R-1, 122	178.52	x	4949.8
27R-1, 122	178.52	z	4957.6
27R-2, 92	179.50	x	4520.6
27R-2, 92	179.50	z	4667.8
27R-3, 119	181.27	x	4947.0
27R-3, 119	181.27	z	4855.3
27R-4, 44	182.02	x	4181.0
27R-4, 44	182.02	z	4239.8
27R-6, 92	185.34	x	5324.1
27R-6, 92	185.34	z	5341.0
28R-1, 56	187.46	x	4471.9
28R-1, 56	187.46	z	4414.1
28R-2, 43	188.77	x	5023.2
28R-2, 43	188.77	z	5143.5
28R-3, 4	189.69	x	5478.8
28R-3, 4	189.69	z	5572.7
28R-4, 36	191.16	x	4452.8
28R-4, 36	191.16	z	4293.0
29R-1, 117	197.67	x	4856.4
29R-1, 117	197.67	z	4726.7
29R-2, 85	198.85	x	4810.6
29R-2, 85	198.85	z	5012.8
29R-3, 115	200.06	x	4649.1
29R-3, 115	200.06	z	4658.9
29R-4, 91	201.04	x	4652.4
29R-4, 91	201.04	z	4728.0
30R-2, 56	208.11	x	5108.3
30R-2, 56	208.11	z	5259.4
30R-3, 72	209.70	x	5231.4
30R-3, 72	209.70	z	5140.6
30R-4, 63	210.06	x	5621.2
30R-4, 63	210.69	z	5420.5
31R-1, 26	216.06	x	5063.0
31R-1, 26	216.06	z	5478.8
32R-1, 26	217.76	x	5368.8
32R-1, 41	217.91	z	5648.3

Note: Only a portion of this table appears here. The complete table is available in **ASCII.**

Table T17. SIOSEIS process parameters for predictive deconvolution, bandpass filtering, and fk-migration.

```
Line 1:
  decon
    fno 1151 lno 1151 sedts 1.72 2.48 fillen .008 pdist .002 prewhi 1 double yes end
    fno 1311 lno 1311 sedts 1.69 2.44 fillen .008 pdist .002 prewhi 1 double yes end
    fno 1471 lno 1471 sedts 1.67 2.42 fillen .008 pdist .002 prewhi 1 double yes end
    end
  filter
    fno 1151 lno 1471 pass 60 150 fillen 55 end
    end
  tx2fk
    nxpad 100 end
    end
  fkmigr
    vel 2000 deltax 11.06 deltat .001 end
    end
  fk2tx
    end
    end
Line 4:
  decon
    fno 4025 lno 4025 sedts 1.67 2.42 fillen .008 pdist .002 prewhi 1 double yes end
    fno 4100 lno 4135 sedts 1.68 2.43 fillen .008 pdist .002 prewhi 1 double yes end
    fno 4163 lno 4345 sedts 1.69 2.44 fillen .008 pdist .002 prewhi 1 double yes end
    end
  filter
    fno 4025 lno 4345 pass 60 150 fillen 55 end
    end
  tx2fk
    nxpad 100 end
    end
  fkmigr
    vel 2000 deltax 9.9 deltat .001 end
    end
  fk2tx
    end
    end
```

Note: Processing was performed in the order shown (see **http://sioseis.ucsd.edu**).